

Diss. ETH No. 15728

Laserbased Ultrasound for Characterization of Thin Films and Microstructures and Resulting Applications

A dissertation submitted to the
SWISS FEDERAL INSTITUTE OF TECHNOLOGY
for the degree of
Doctor of Technical Sciences

presented by

Dieter M. Profunser

Dipl. Masch.-Ing. ETH
born May 19, 1974
citizen of Austria

Accepted on the recommendation of
Prof. Dr. J. Dual, examiner
Prof. Dr. D. Poulidakos, coexaminer

Zürich, 2004

Acknowledgements

This work was carried out during my employment as a research assistant at the Institute of Mechanical Systems, ETH Zürich. I would like to thank everyone who contributed to my thesis, in particular:

Prof. J. Dual, my supervisor, for guiding my research and his many helpful contributions and suggestions. The friendly atmosphere in his group and the academic freedom to try challenging and unconventional ideas, provided excellent research conditions.

Prof. D. Poulidakos, my co-examiner, for agreeing to review my thesis without hesitation.

Prof. Dr. M.B. Sayir who created a stimulating work environment.

Dr. Jacqueline Vollmann for the fruitful collaboration, interesting discussions and for reviewing my work.

Traude Junker and Dr. Stephan Kaufmann for providing excellent administrative and computational services.

Jürg Bryner, Bernard Masserey, Kuno Meyer and Andreas Meier for writing their semester or diploma thesis with great enthusiasm within the scope of my research project. Ondrej Papes, Andreas Ehrsam and Christoph Gerber for their valuable contributions to this thesis working as Hilfsassistent.

My office companion Francesco Colombo and my colleagues István Veres, Udo Lang, Gerd Simons, Albrecht Haake and Frank May and all the other members of the Center of Mechanics for interesting discussions and generally for having a good time.

Tamara Scherer and Karl Vollmers for their kind help regarding the linguistics of this work.

Finally, I would like to thank Claudia Salamon and my family for their support and motivation throughout my thesis.

Dieter Profunser
Zürich, September 2004

Table of Contents

Abstract	v
Zusammenfassung	vii
List of symbols	ix
1 Introduction	1
1.1 Review of previous work	3
1.1.1 Experimental work.	3
1.1.2 Theoretical work	4
1.2 Motivation and goals	6
1.3 Contents of this thesis	7
2 Theoretical considerations and modelling of the experiment	11
2.1 Excitation and propagation of acoustic pulses produced by ultrashort laser pulses: analytical model	12
2.2 Numerical modelling	21
2.2.1 Numerical model of the one-dimensional linear elastic wave propagation	21
2.2.1.1 Implementation	21
2.2.1.2 Discussion	24
2.2.2 Numerical model for the ultrashort pulse laser heating	26
2.2.2.1 Theoretical considerations.	27
2.2.2.2 Implementation	27
2.2.2.3 Discussion	28
2.2.3 Non-equilibrium numerical modelling of the ultrashort laser pulse heating	30
2.2.3.1 Theoretical considerations.	31
2.2.3.2 Implementation	32
2.2.3.3 Results and Discussion	33

2.3	Further aspects of the propagation characteristics of the acoustic pulses	38
2.3.1	Surface roughness	38
2.3.2	Limits of continuum-mechanics	38
2.4	Detection of the acoustic pulses	40
2.4.1	Perturbations of the dielectric constants (or refractive index) ..	42
2.4.1.1	Perturbations of the dielectric constants by the mechanical strain	42
2.4.1.2	Perturbations of the reflectivity caused by the induced temperature	44
2.4.1.3	Complete simulation of the experiment on a single opaque thin film	45
2.4.2	Perturbations of the refractive index in transparent thin films and of the interface positions	46
3	Experimental setup	49
3.1	Setup	50
3.2	Most important components of the experimental setup	54
3.2.1	Ultrashort pulse laser	54
3.2.2	Electro-optical modulator	57
3.2.3	Mechanical modulator	59
3.2.4	Balanced photodetector	60
3.2.5	Lock-In amplifiers	60
3.2.6	Computer-based signal processing with LabView™	61
3.3	Signal processing	61
3.4	Discussion of quantitative aspects	63
3.5	Different measurement configurations	66
4	Results	69
4.1	Measurements on thin films	69
4.1.1	Aluminium thin films	70

4.1.1.1 Specimens	70
4.1.1.2 Measurements and Discussion	71
4.1.1.3 Influence of the measurement configuration and the boundary conditions	76
4.1.2 Platinum thin films.	79
4.1.3 Multilayers, stacks of thin films.	80
4.1.3.1 Aluminium - Gold.	80
4.1.3.2 Functionally graded materials (FGM), in-depth profiling and applications	82
4.1.3.3 Copper - tantalum - tantalum-nitride.	84
4.1.3.3.1 Barrier layers	84
4.1.3.3.2 Problem formulation and solution strategy	85
4.1.3.3.3 Detailed procedure for investigating diffusion barrier layers.	86
4.1.3.3.4 Extension of the simulations - considering heat flux in the lattice	90
4.1.3.3.5 Measurements and simulations with aluminium top layer for the determination of the bulk wave velocity of Ta, TaN and Cu	91
4.1.3.3.6 Simulations with copper top layer	99
4.1.3.3.7 Discussion.	106
4.2 Measurements on transparent materials.	106
4.2.1 Specimen	106
4.2.2 Measurements and Discussion.	107
4.3 Bulk wave propagation in membranes	109
4.3.1 Specimen	109
4.3.2 Measurements and Discussion.	111
4.3.2.1 Measurements on supported membranes coated with 10nm aluminium	111
4.3.2.2 Measurements on a free silicon-nitride membrane coated with 120nm aluminium	112

4.3.2.3	Comparison of measured and simulated results of a membrane coated with 40nm aluminium	114
4.3.2.4	Summary of the measured results	115
4.4	Measurements on cantilevers and AFM tips	116
4.4.1	Cantilevers	116
4.4.2	AFM tips	124
4.4.2.1	Motivation - focussing of acoustic pulses	124
4.4.2.2	Specimen preparation	126
4.4.2.3	Measurements on truncated AFM - tips	128
5	Conclusions and Outlook	131
5.1	Simulation and modelling of the experiment	131
5.2	Experimental setup	132
5.3	Experimental results	132
Appendix A: Material properties		135
Appendix B: Magic time step		137
Appendix C: Reflectivity change		140
Appendix D: Electro-optical modulator		141
Bibliography		145
Curriculum vitae		153

Abstract

The goal of most ultrasonic techniques is to obtain geometrical and/or mechanical information from structures in a non-destructive way. In order to achieve an acceptable resolution, the wavelength of the acoustic pulses propagating through the media has to be short compared to the geometrical dimensions of the specimen. When characterizing microstructures and thin films having sub-micron dimensions, this condition becomes very challenging. For the inspection of machine parts and airplane structures wavelengths in the millimeter range are sufficient, whereas wavelengths for analyzing microstructures and thin films need to be in the order of tens of nanometers. Since classical devices, such as piezoelectrical transducers or layers, are usually cumbersome on the specimens, the excitation and detection of ultrasound with such small wavelengths is realized using an optical so-called pump-probe technique, which has been successfully adapted.

The pump and probe laser pulses are synchronously emitted by an ultrashort pulse laser unit. Thermoelastically induced acoustic pulses are produced, through the absorption of a pump laser pulse. The acoustic pulses propagate perpendicular to the surface into the microstructure. At any discontinuity of the acoustic impedance the acoustic pulses are partly reflected or transmitted. With the second laser pulse, the probe pulse, the reflectivity at the surface of the specimen is measured. The induced temperature, as well as the propagating acoustic pulse, slightly changes the reflectivity at the surface. These changes are measured versus time. The temporal resolution of the pump-probe technique is only limited by the laser pulse duration, which is in the order of 100 femtoseconds. Therefore, phenomena, such as high frequency acoustic pulses, occurring on time scales shorter than the rise time of currently available photo-detectors become accessible.

Accurate models form the basis for the inverse problem: the determination of geometrical or mechanical properties of the specimen by fitting the simulated results and measured wave propagation phenomena. Apart from an analytical thermomechanical model, numerical models using finite differences (FTDT) for describing the fast transient heating after absorption of the pump laser pulse, the heat transport and the subsequent thermomechanical generation and propagation of bulk acoustic waves, are developed. Enhanced heat transport occurs on the very short time scale of the absorption of the laser pulses in metallic thin films, which is considered using the so-called two temperature model. The reflectivity change is determined with the calculated temperature and strain distribution. In the first place, these models were developed for metallic thin films but can also be used in some cases with semiconducting or transparent films, for instance.

These techniques are successfully applied for characterizing aluminium and platinum thin films, as well as multilayers, e.g. an aluminium-gold structure on a silicon substrate. With the measured bulk wave velocity the thickness or the Young's modulus of the layers is determined.

Using thermally induced intermetallic diffusion layers between an aluminium and a gold thin film are realized. Measurements with laserbased ultrasound show that these intermetallic layers can be used for acoustic signal filtering.

Copper layers are of growing importance for chip manufacturers. To prevent copper diffusing into the silicon semiconductor it is necessary to deposit thin diffusion barrier layers (tantalum, tantalum-nitride) in between. With a series of measurements and simulations the determination of material properties and thickness of these underlying diffusion barriers is discussed.

Measurements on aluminium coated silicon nitride membranes with a total thickness of several hundred nanometers and on silicon cantilevers showed that these techniques can also be used for determining material properties of freestanding micro- and nanostructures. This is important, since their material properties vary strongly with fabrication technology. In general, the experiments showed that this measurement technique, which works in a non-contact and non-destructive way, is a valid approach for deriving mechanical properties of thin and brittle MEMS-structures.

If mechanical pulses are excited in a structure which is tapered to a point, such as an AFM tip, these acoustic pulses can be focused depending on the frequency spectrum of the acoustic pulse and the geometry of the structure. Measurements in truncated AFM tips which focusses acoustic pulses, were performed, for developing new metrology techniques, such as local probe methods with high time resolution.

Zusammenfassung

Das Ziel vieler Anwendungen von mechanischem Ultraschall ist, neben der Lokalisierung von Fehlstellen und Rissen, die zerstörungsfreie Bestimmung von mechanischen Materialkonstanten oder auch von geometrischen Abmessungen. Um eine hohe Messgenauigkeit zu erreichen, ist es notwendig, dass die mechanische Wellenlänge im Vergleich zu den Abmessungen der Struktur klein ist. Bei der Charakterisierung von Mikrostrukturen oder Dünnschichten ist diese Voraussetzung schwieriger zu erfüllen als bei grossen Strukturen. Beim Testen von Flugzeug- oder Maschinenteilen liegt die mechanische Wellenlänge beispielsweise in der Grössenordnung von Millimetern, bei Mikrostrukturen oder Dünnschichten muss jedoch eine Wellenlänge von einigen Nanometern verwendet werden. Da piezoelektrische Transducer auf den Proben üblicherweise extra aufgebracht werden müssen und ausserdem störend sein können, wurde die Anregung und Messung der hochfrequenten mechanischen Wellen mit der sogenannten optischen Pump-Probe-Technik realisiert.

Die Pump- und Probe-Laserpulse werden synchron von einem Ultrakurzpulslaser emittiert. Durch die Absorption der Pump-Laserpulse werden thermomechanisch akustische Pulse erzeugt, die normal zur Oberfläche in die Mikrostruktur laufen. An jeder Unstetigkeit der akustischen Impedanz wird ein Teil der Welle reflektiert, der Rest transmittiert. Mit dem zweiten Laserpuls, dem Probe-Laserpuls, wird die Reflektivität an der Oberfläche gemessen, die durch die induzierte Temperatur und die reflektierten akustischen Pulse beeinflusst wird. Diese Technik erlaubt, aufgrund der repetitiven Experimente, Phänomene aufzulösen, deren Frequenzinhalt weit über der Bandbreite und den Anstiegszeiten von gegenwärtigen Photodetektoren und Messinstrumenten liegen.

Genaue Modelle und Simulationen sind die Basis für die Lösung des inversen Problems: der Bestimmung von Abmessungen oder Materialparameter durch Fitten von simulierten Resultaten und der gemessenen Wellenausbreitungsphänomene. Neben analytischen Modellen wurden auch numerische Modelle mittels finiten Differenzen (FDTD) zur Beschreibung der transienten Erwärmung nach Absorption des Laserstrahls und der darauffolgenden Ausbreitung der akustischen Pulse entwickelt. Überproportionaler Wärmetransport ist während der Absorption des Pump-Laserpulses in metallischen Schichten zu beobachten und wurde in den Modellen mit dem sogenannten Zwei-Temperaturmodell berücksichtigt. Mit der berechneten Temperatur und Dehnung im Material kann die entsprechende optische Reflexionsänderung berechnet werden. Zuerst wurden diese Modelle für metallische Schichten entwickelt, da sie den Hauptanwendungsfall darstellen. Die Modelle können aber auch in einigen

Fällen für halbleitende und transparente Filme angewendet werden.

Die entwickelten Techniken wurden erfolgreich für die Charakterisierung von Aluminium- und Platinfilmen sowie von Mehrschichten aus Aluminium und Gold verwendet. Mit der gemessenen Wellenausbreitungsgeschwindigkeit können die Dicke der Schicht oder deren mechanische Parameter (Elastizitätsmodul) bestimmt werden.

Bei höheren Temperaturen entsteht zwischen Gold und Aluminium durch Materialdiffusion eine intermetallische Zwischenschicht. Mittels Laserultraschall konnte gezeigt werden, dass diese Schichten für akustische Filterung verwendet werden können.

In der Halbleiterindustrie sind Kupferschichten von steigender Bedeutung, diese haben jedoch den Nachteil, dass Diffusionssperren aus dünnen Tantal- oder Tantalnitridschichten notwendig sind, um die Diffusion von Kupfer in den Halbleiter zu unterbinden. Im Rahmen dieser Arbeit wurde auch die Charakterisierung dieser Diffusionssperrenschichten unter dem Kupferfilm diskutiert. Bei Messungen an dünnen Siliziumbalken und an aluminiumbeschichteten ultra-dünnen Membranen mit einer Gesamtdicke von einigen hundert Nanometern, stellte sich heraus, dass diese Technologie auch zur Charakterisierung von freistehenden Mikrostrukturen verwendet werden kann. Die Messungen zeigten, dass diese zerstörungsfreie und berührungslose Technologie einen der besten Wege zur Charakterisierung von dünnen MEMS-Strukturen darstellt.

Wenn mechanische Pulse in einer Struktur angeregt werden, die spitz zu einem Punkt zusammenläuft, wie beispielsweise eine Spitze für die Rasterkraftmikroskopie, fokussieren sich die akustischen Wellen abhängig vom Frequenzgehalt und der exakten Geometrie der Struktur. Versuche an modifizierten Siliziumspitzen, wie sie auch für Rasterkraftmikroskope verwendet werden, wurden durchgeführt, mit dem Ziel neue Messtechnologien zu entwickeln, wie beispielsweise Rastermikroskopieverfahren mit hoher zeitlicher Auflösung.

List of symbols

ξ	absorption length
Z_1, Z_2	acoustic impedance
r	acoustic reflection coefficient, optical reflection
C	capacity
a	constant
b	constant
N_1	defined constant
N_2	defined constant
N_3	defined constant
n_e	defined constant
k_e	defined constant
q	defined constant
ρ	density
ϵ	dielectric constant
$\Delta\epsilon, \Delta\epsilon_x, \Delta\epsilon_y$	dielectric constant change
D	diffusivity
$u_z, u_i, u_{i+1}, u_{i-1}, u_3$	displacement
a	distance
A_{ijkl}	elastic compliance tensor
C_{ijkl}, C_{11}, \dots	elastic stiffness tensor (components of -)
G	electron-phonon coupling constant
γ	electronic specific heat constant
E	energy
$f, \omega, f_{max}, f_{-3dB}, f_{res}$	frequency (maximum -, cut off-, resonance-)
f	function, sensitivity function
C, C_e, C_b	heat capacity (electron-, lattice-), spring constant
Q	heat source term

H	Heavyside function
$\kappa, \kappa_{Si}, \kappa_f$	imaginary part of the refractive index
L	inductance
I_z, I_s	intensity
A, A_s	irradiated area of the spot size
λ, λ_n	Lame constants, optical wavelength
μ, μ_n	Lame constants
t_p	laser pulse duration
J	laser pulse energy
α, α_{kl}	linear expansion coefficient
τ	lockin time constant
c_l	longitudinal wave velocity
m, M	mass
P_{out}	measured power
ΔP_{out}	measured power change
U_{out}	measured voltage
ΔU_{out}	measured voltage change
m	numerator
n	numerator, real part of the refractive index
λ	optical wavelength, Lame constant
r, r_p, r_o	optical reflection
Δr	optical reflection change
R	optical reflectivity
$\Delta R, \Delta R_u$	optical reflectivity change
t_{vf}, t_{fv}	optical transmission coefficient
ϑ	parameter of crank-nicholson
P_{ij}, P_{11}, \dots	photoelastic constants
n, n_{Si}, n_f	real part of the refractive index, numerator
Δn^*	refractive index change
f	sensitivity function, function
c	specific heat capacity
z, z_i, z'	spatial coordinate
Δz	spatial step size
C	spring constant
Δs_{min}	step size of translation table
$\epsilon_z, \epsilon_{ij}, \eta_z$	strain
$\sigma_z, \sigma_{z, mech}, \sigma_{z, temp}, \sigma_{kl}$	stress
T, T_e, T_l	temperature (electron-, lattice-)
ΔT	temperature increase
$I(t)$	temporal profile

Δt_{min}	temporal resolution
$\Delta t, \Delta t_{magic}$	temporal step size (magic time step)
d	thickness
K, K_e, K_l	thermal conductivity (electron- , lattice-)
t, t_n	time coordinate
v_z	velocity
k, k_v, k_f	wave vector

Chapter 1

Introduction

Thin films and microstructures are widely used in the semiconductor industry, automotive industry, in visual display technologies, biotechnology and numerous other fields such as electrical signal filtering. With the growing importance of thin films and electromechanical microstructures a great demand arises for rapid characterization during and after fabrication. Many different methods such as the well-known scanning probe techniques provide data of roughness and surface quality and of electrical and optical properties. But for the mechanical characterization mostly destructive techniques such as nanoindentation are used.

However, the mechanical quantities are usually key parameters for the correct operation of the microdevices and performance of thin films and coatings. Since manufacturing processes and conditions and the film thickness significantly influence the resulting mechanical properties non-destructive measurement techniques are necessary, which can provide mechanical properties of coatings or microstructures after fabrication.

In similar problems of bulk testing, common ultrasonic techniques are used to obtain geometrical and/or mechanical information from structures in a non-destructive way, by measuring wave propagation phenomena. With the measured time of flight of the acoustic pulses or the measured wave velocity, geometrical dimensions or mechanical properties are determined. In order to achieve an acceptable resolution the wavelength of the acoustic pulses propagating through the structure have to be short compared to the geometrical dimensions of the specimen. This condition becomes especially challenging when inspecting microstructures and coatings with sub-micron dimensions. While the wavelength used for the ultrasonic inspection of machine parts, air-

plane and other bulk structures is in the millimeter range, the wavelength excited to analyze microstructures and thin films needs to be in the nanometer range. New experimental techniques are necessary because the efficiency of piezoelectric devices is typically too small for the excitation and detection of ultrasound with frequencies of several hundred GHz that correspond to these tiny acoustic wavelengths.

The research group of H.J. Maris was first to observe the generation of very high frequency acoustic pulses in metallic thin films with short laser pulses. The excited acoustic pulses have a wavelength in the order of several tens of nanometers and are small enough for the application in ultrasonic measurements of thin films. Until that time no one had surmised that sound pulses with such high frequency content could be created (Maris H.J. [37]). By sending a second laser pulse which is measuring the reflectivity the detection of the excited longitudinal acoustic pulses is realized. These experiments have been the basis for a new and special field of scientific research in mechanics.

<i>Picosecond ultrasound</i>		<i>"Classical" ultrasound</i>
10-20nm	acoustic wavelength	0.5-2mm
100-600GHz	frequencies	5-10MHz
thermoelastic by ultra-short laser pulses	sound excitation	piezoelectrical
reflectivity scan, interferometrical, ...	sound detection	piezoelectrical, interferometrical, ...

Table 1.1 Comparison of picosecond and "classical" ultrasound in typical configurations

Two more approaches of photoacoustic evaluation of thin films are well-known, both of which are working with surface acoustic waves instead of bulk acoustic waves. In one method laser pulses are focussed towards the surface and excite surface acoustic waves by line or point excitation. The detection can be realized by a second laser pulse measuring the reflectivity or by other methods like piezoelectrical or interferometrical detection because the excited frequencies of the surface acoustic waves are lower. Thickness and/or mechanical properties are determined with the surface acoustic wave velocity. In the other technique two or more laser pulses interfere on the surface of the specimen and excite narrow band surface acoustic waves. In contrast to the first technique the frequency content is even lower. The reason is that the overlapping laser pulses form an interference pattern - called transient grating

(Rogers J.A. [65]) - which is absorbed and excites surface acoustic waves with a unique wave vector corresponding to the spacing of the grating. The detection is performed by diffraction of an incident continuous wave laser beam.

1.1 Review of previous work

1.1.1 Experimental work

Laser techniques have been well established as alternatives to piezoelectrical and electromagnetic excitation of ultrasound. Advantages such as the non-contact measurement leads to an extension towards various applications. Therefore, work has been published concerning the excitation of sound waves, the interactions of the optical and ultrasound field and the detection. The used laser pulses are usually in the order of nanoseconds and the excited waves have frequencies in the MHz region.

Since the early 1980s lasers could produce light pulses in the order of 10^{-14} s (Maris H.J. [37]). But only as a result of the unexpected possibility to excite acoustic pulses with frequencies far beyond 100GHz has been the ultrasound technique extended into a new frequency region. This is reported in a paper about the generation and detection of phonons in a-As₂Te₃ and cis-polyacetylene (CH)_x by picosecond light pulses published by the group of Maris H.J. [80]. Measurements in different thin films and multilayers (As₂Te₃, metallic thin films) and a theory of generation and detection of acoustic pulses by picosecond laser pulses followed (Thomsen C. et. al. [81]). They also investigated the detection of ultra-thin interfacial layers (Tas G. et. al. [77]), vibrational modes of gold nanostructures (Lin H.-N. et. al. [35]), and the acoustic reflection from solid-liquid interfaces (Tas G. et. al. [78]). Also, a time-resolved pump-probe experiment with sub-wavelength lateral resolution by means of a reflection near-field scanning microscope (SNOM) was reported by Vertikov A. et. al. [84]. Together with a supplier of the semiconductor industry - this technique has been commercialized for measuring the thickness of thin films and film stacks, which places great demand on further research.

Wright O.B. published several papers (e.g. [89]) about measuring transparent thin films. In transparent and semi-transparent films the interpretation of measured signals is much more challenging as with opaque thin films. A theory considering all contributions to the reflectivity change was developed by Wright O.B. [89]. In 1992 the detection of ultrafast surface vibrations by an angular deflection of the reflected probe laser beam was presented by Wright O.B. et. al. [92]. Recently an improvement of the ultrafast detection by a modified Sagnac interferometer was reported (Hurley D.H. et. al. [25]) which was used for the novel detection of ultra high frequency transverse sound pulses

(Hurley D.H. et. al. [26]). At present the group of Wright O.B. is working also in the field of high frequency surface acoustic waves and on a detailed theory describing the detection in various measurement configurations.

Perrin B. and coworkers showed the application of picosecond ultrasound for the study of elastic and thermal properties of materials (Bonello B. et. al. [2]). They also published work on photoacoustics in colloids (Devos A. et. al. [14]) and their interferometrical detection (Perrin B. et. al. [51]). Recently they published time-resolved acoustic measurements with a lateral resolution in the order of 100nm (Siry P. et. al. [71]). For such high resolution it was necessary to work with a tapered fiber in the optical near field. The configuration is different to that used by the group of Maris H.J. [84] because for the incident and reflected probe light the same fiber was used.

The application of a Michelson interferometer for detection is reported by Richardson C.J.K. et.al. [63]. Richardson C.J.K. and Spicer J.B. [41] showed the excitation of narrow band longitudinal waves by a train of four laser pulses. Working with longitudinal acoustic waves with a narrow frequency content allows signal filtering with high frequency band pass filters.

Similar experiments are used for investigating time resolved thermal transport phenomena in thin films and multilayer stacks. For this thesis these experiments are interesting in connection with the modelling of the excitation of the sound waves by means of ultra-short laser pulses.

Reviewing the published work of the mentioned groups gives a detailed and almost complete overview of the research work done in the field of picosecond ultrasound. In addition it is emphasized that nearly no work has been done for microstructures except by Matsuda O. et.al. [39] who recently published one paper on the subject.

1.1.2 Theoretical work

Picosecond ultrasonics is a multidisciplinary subject with a main emphasis on optics, thermodynamics and thermomechanics as well as elastic wave propagation. In this thesis the modelling and theoretical work focuses on the thermomechanical laserbased excitation and the propagation of acoustic pulses.

Thermodynamics and thermomechanics

In the paper of Thomsen C. et. al. [81] a theory of the excitation and detection of acoustic pulses with short laser pulses is presented and it is sufficient as long as the temperature diffusion plays a minor role or the laser pulses are not too short. A similar theory was used to describe the excitation of sound waves with laser pulses of nanosecond duration (Scruby C.B. et. al. [69]). Working

with ultra-short laser pulses and the very short time scale forces one to look at the thermodynamics and thermomechanics from a microscopic point of view. This has the consequence of a different modelling for metals, semiconductors and insulating materials. Since the setup is optimized for aluminium thin films, and metallic thin films are the most popular application, the modelling is developed for conductive materials. In the 1970s Anisimov S.I., et. al. [1] presented the two-temperature model which describes from a microscopic point of view the ultrafast and non-equilibrium heating process in metallic materials. The model was based on work of Kaganov M.I., et.al. [28]. Further development in this field was done by Tien C.L. and coworkers. They developed the hyperbolic two-step-model which describes in a similar but more general way the mechanism of energy transport during ultra-short pulse laser heating [59]. Experiments for validating the models and the basics of the numerical solution of the fast transient heating are also presented in papers of Tien C.L. et. al. [61][62]. The book of Tzou D.Y. [82] gives a very good introduction to the microscale heat transfer with a detailed discussion about the two-temperature model.

In the paper of Tas G. et.al. [79] the two-temperature model was combined with the solution of the elastic wave equation. Since analytical solutions are very difficult and usually only possible for special cases the obvious thing would be to solve the system of several differential equations in a numerical way. Recently, during the development of this thesis Chen J.K. et.al. published several papers about the numerical study of ultrashort laser pulse interactions with metal films in a 1-D formulation [7]. A quasi-3D axisymmetric study by Chen J.K. et.al. [6] followed.

The excitation of acoustic pulses in semiconductors is also discussed by Thomsen C. et. al. [81] and also elaborated in other publications. A good overview of excitation in different materials such as semiconductors and piezoelectrical materials in various configurations plus the discussion of nonlinear effects are given in the book of Gusev V.E. and Karabutov A.A. [19].

With an ultra-short pulse laser system it is easy to exceed the damage threshold of nearly any material and excite acoustic pulses with very high amplitudes (shockwaves) through ablation. Excitation of surface shockwaves is not taken into account in this review because the non-destructive manner is a key feature of picosecond ultrasound.

Optical detection

A theory for the reflectivity change caused by an acoustic pulse in an opaque film is proposed by Thomsen C. et. al. [81]. A modulation of the dielectric constants due to the strain distribution results in a change of the surface reflec-

tivity. This reflectivity change is measured in different configurations which are mentioned in Chapter 1.1.1. A theory covering the reflectivity change caused by acoustic pulses in transparent thin films is given in the published papers of Wright O.B. (see in Wright O.B. [89]). In several recently published papers Wright O.B. and Matsuda O. [40] developed a general closed theory for the reflectivity change caused by a strain distribution.

Miklos A. and Lörincz A. [42] showed a detailed calculation of the reflectivity change based on the solution of the maxwell equations. In their calculations the reflectivity is being modulated by the transient temperature.

A complete simulation of the experiment consisting of the thermoelastic excitation and the propagation of the acoustic pulse as well as a model for the detection can be realized by combining the theoretical background of each part with the appropriate numerical method. Such general numerical models especially with a calculation of the wave propagation in 1-, 2- or 3D-configurations has not been realized yet.

1.2 Motivation and goals

The Center of Mechanics has expertise and the appropriate experimental equipment for measuring wave propagation phenomena with frequency content up to several MHz. This range is extended into a new frequency region with the new ultrashort pulsed laser acoustic setup, which was developed together with Vollmann J.

With the new experimental setup it is possible to measure bulk wave propagation with sub-picosecond temporal resolution and with a spatial resolution of several microns. Also a complete numerical simulation covering the excitation, propagation and detection of the acoustic pulses is developed. With these accurate measurements and appropriate simulations the following new fields are examined in this thesis:

- Limits for the determination of material properties or thickness of thin diffusion barrier layers below a copper film are systematically investigated
- Intermetallic diffusion layers and their use for acoustic signal filtering are investigated using laserbased ultrasound
- Characterization of microstructures, such as ultra-thin membranes and cantilevers using measurements of the bulk wave propagation
- Measurements of the bulk wave propagation in modified silicon tips, which are usually used in atomic force microscopes.
- Moreover the excitation, propagation and detection of acoustic pulses in several different measurement configurations is discussed.

1.3 Contents of this thesis

The content of this thesis is divided into two main parts. The first part focuses on the development of the modelling and simulation as well as the experimental setup. Following this the results of measurements on thin films and microstructures are presented in the second part.

Modelling and simulation

The development of an accurate numerical model for the excitation and propagation of acoustic pulses is presented in the first part (Profunser D.M. et. al. [54]). An accurate model forms the basis for the inverse problem: the determination of geometrical or mechanical properties of the specimen by fitting the simulated and measured results. At the beginning a simple thermomechanical model (Thomsen C. et. al. [81]) is discussed which neglects that the incident laser pulse is of very short duration. Nevertheless this model is sufficient for many cases and has even the advantage of its simplicity. Furthermore improvements are made in describing the absorption of the laser pulse and considering the heat transport. The influence of heat transport on the acoustic pulse depends mainly on optical and thermal properties of the top layer material. To avoid complex analytical solutions the time dependent absorption of the laser pulse, the heat transfer and the elastic wave equation are solved in a numerical way to provide ease of calculation of the results for different geometries and materials. Enhanced heat transportation caused by the shortness of the laser pulses occurs in metallic thin films. It is considered in the so-called two temperature model which is implemented in the modelling. All models are discussed based on examples of aluminium and copper thin films and partly also platinum and gold coatings. The numerical models can also be applied to the two or three-dimensional cases, which is necessary if the spot size of the laser pulse becomes very small compared to the film thickness or if the acoustic pulse interacts with the lateral boundary or lateral structure of the specimen. The simulation of the experiment is split up as follows:

- Simulation of the absorption of the ultrashort laser pulses and calculation of the induced temperature rise
- Calculation of the induced strain and the propagation of the acoustic pulses
- Modelling of the detection based on the optical reflectivity changes caused by the propagating acoustic pulses

The models were developed for metallic thin films but can also be used in some cases with semiconducting or transparent films.

Experimental setup

The so-called optical pump-probe technique was successfully adapted to carry out picosecond ultrasound measurements on sub-micron scales (Vollmann J. et. al. [85]) based on work previously published by the groups of Maris H. J. [81] and Wright O.B. [92].

Thermoelastically induced acoustic pulses are produced by the absorption of a femtosecond laser pump pulse. The acoustic pulse propagates perpendicular to the surface of a microstructure or thin film until it encounters a discontinuity in acoustic impedance causing the pulse to be partly reflected and partly transmitted. The reflected and/or transmitted acoustic pulse cause a slight change of the optical reflectivity at the surface of the specimen, which is detected optically with the probe pulse. In this technique two optical paths of variable length are used to precisely control the time shift between two synchronously emitted ultrashort laser pulses. Thus phenomena occurring on time scales shorter than the rise time of currently available photodetectors can be observed. Therefore, the time of flight of an acoustic pulse and its pulse shape can be measured. The research involves the development of a novel dual frequency modulation technique to improve the signal-to-noise ratio of this measurement.

Results - Characterization of thin films

Experiments were successfully performed in different configurations on aluminium and platinum thin films and in different multilayers. For example in an aluminium-gold structure on a silicon substrate. In some materials such as copper and gold the heat diffusion during the absorption of the ultrashort laser pulse affects the shape and the acoustic frequency spectrum of the propagating acoustic pulses. In these materials the acoustic wavelength is usually much longer (the frequency content much lower) than in aluminium, for instance. Since copper is of growing importance for chip manufacturers, we discussed the detectability of very thin diffusion barrier layers below a copper top layer. We showed that it is very difficult to quantitatively determine the mechanical properties of these underlying layers even with a very accurate model. Also the influence on the wave propagation of atomic diffusion between the aluminium and gold layers was discussed by Vollmann J. et. al. [87] using experiments and accurate models.

Results - Measurements on microstructures

The investigations of thin films showed that it is also possible to use this experimental technique for the determination of geometrical properties like film thickness based on the known bulk acoustic wave velocity and the mea-

sured time of flight of the acoustic pulse. Alternatively, the mechanical properties (Young's modulus) instead of the thickness can be estimated from the data. Measurements were performed on aluminium coated silicon nitride membranes with a total thickness of several hundred nanometers. Since the Young's modulus of silicon nitride strongly depends on the deposition technique and the deposition conditions, experimental data were used to estimate the Young's modulus of the silicon nitride membrane deposited by LPCVD (low pressure chemical vapor deposition). In addition, the bulk wave propagation in a aluminium coated silicon cantilever was measured. These experiments show that this measurement technique, which works in a non-contact and non-destructive way, is a valid approach for deriving mechanical properties of thin and brittle MEMS-structures such as membranes and cantilevers (Profunser D.M. et. al. [55]).

Results - Applications

If mechanical pulses are excited in a structure which is tapered to a point these acoustic pulses can be focused to an extent that depends on the frequency spectrum of the acoustic pulse and the geometry of the structure. Experiments are carried out measuring the bulk wave propagation in modified silicon tips. Such tips are usually used in atomic force microscopes. The application of this new technique as a transducer or in a new scanning probe method has been proposed by Profunser D.M. et. al. [53].

The acoustic wave propagation in functionally graded materials like a diffusion layer between an aluminium and a gold thin film can be used in signal filtering devices. Experiments and simulations with different acoustic frequency spectra were successfully performed in this connection (Vollmann J. et. al. [86]).

Chapter 2

Theoretical considerations and modelling of the experiment

Acoustic pulses with a wavelength below of tens of nanometers are required for the non-destructive determination of mechanical properties or geometrical dimensions of sub-micron films and microstructures by ultrasound. This small wavelength corresponds to acoustic pulses having frequency content beyond 100GHz. To generate (and measure) acoustic pulses with such high frequencies ultrashort laser pulses are an excellent way - basically - the only one.

An accurate model of the light matter interaction as well as the elastodynamic wave propagation is the basis for solving the inverse problem: the determination of geometrical or mechanical properties of the specimen by fitting simulated and measured results. Moreover, properties such as thermal conductivity and photoacoustic properties can be determined. If the solution of the equations which describes the laser pulse absorption, heat transfer and acoustic wave propagation is done in a numerical way, it is easy to calculate the results for different specimen and measurement configurations. An extension of the models to the two or three-dimensional case is also straight forward. Simulations in two- or three dimensions are necessary if the spot size of the laser pulses becomes very small compared with the film thickness or if the acoustic pulse interacts with the boundary or structure of the specimen.

In general this section has the following two main parts:

- 1) excitation and propagation of the acoustic pulses
- 2) detection of the acoustic pulses

In the first subsection the basics of the excitation and propagation of acoustic pulses produced by ultra-short laser pulses are discussed using an analytical model. Some parts of this derivation are based on the work of Thomsen C. et. al. [81] and Bryner J. [5]. Using finite difference methods for the numerical simulation of the absorption of the laser pulses, the heat conduction and the acoustic wave propagation more accurate models are introduced in the subsections that followed. Then some further aspects such as the surface roughness which affects the propagation of the acoustic pulses are discussed. The detection principles and the corresponding theory is presented in the last subsection. Combining the simulation of the excitation and propagation with the theory of the detection leads to a complete and accurate model of the experiment. Such a complete numerical simulation of the overall experiment, which can be easily applied in different measurement configurations and on various specimens (single thin films, multilayer stacks, transparent substrates and transparent thin films) has not been presented. Results are shown in Chapter 2.4.1.3, Chapter 4.1.1.3 and Chapter 4.1.3.3.

2.1 Excitation and propagation of acoustic pulses produced by ultra-short laser pulses: analytical model

The modelling of the absorption of the laser pulse and the subsequent transient heating is only discussed for metal thin films and is different in semiconducting and isolating materials. The derived equations are applied to four metal thin films (aluminium, platinum, gold and copper) to illustrate, on the one hand, the physical meaning and on the other hand, the variations caused by the different physical properties of each metal film.

The surface of an absorbing metal thin film or metallic coated microstructure is irradiated with ultra-short laser pulses having durations of less than 100fs. In the top layer the laser pulses are absorbed within a characteristic, material dependent distance, the absorption length ξ . The absorption length ξ or penetration (skin) depth (derived from Thomsen C. et. al. [81])

$$\xi = \frac{\lambda}{4\pi\kappa} \quad (2.1)$$

is calculated with the wavelength of the laser λ and the imaginary part of the refraction index κ of the top layer material. The time varying intensity in the in-depth direction z in the thin film is

$$I_z(z, t) = (1 - R) I_s(t) e^{\left(\frac{-z}{\xi}\right)} \quad (2.2)$$

in which R denotes the optical reflectivity of the thin film, $I_s(t)$ the intensity of

the incident laser beam and ξ the penetration depth according to Equation (2.1).

The absorbed pump laser pulse deposits the following energy $dE(z)$ in an infinitesimal region at a distance z with width dz and uniformly irradiated area A_s of the thin film

$$dE(z) = \int \left(-\frac{d}{dz} I_z(z, t) A_s dz \right) dt = (1 - R) \frac{I}{\xi} e^{\left(-\frac{z}{\xi}\right)} A_s dz \cdot \int I_s(t) dt \quad (2.3)$$

with the assumption of a constant intensity $I_s(t)$ during the pulse duration t_p Equation (2.3) reduces to

$$dE(z) = (1 - R) \frac{I}{\xi} e^{\left(-\frac{z}{\xi}\right)} A_s I_s t_p dz \quad (2.4)$$

The area A_s of the specimen irradiated by the laser pulse is large compared to the film thickness d and the absorption length ξ . Therefore the excitation of the acoustic waves is considered in the z direction only. Metallic thin films have absorption-lengths (penetration depth) ξ in the order of 10 to 20 nm which is three orders of magnitude smaller than the experimentally achievable spot size A_s ($\sim 5\text{-}50 \mu\text{m}$ in diameter).

<i>Material</i>	<i>n</i>	<i>κ</i>	<i>R</i>	<i>Penetration (skin) depth ξ [nm]</i>
Aluminium	2.80	8.45	0.87	7.54
Platinum	2.84	4.95	0.71	12.86
Gold	0.18	5.12	0.97	12.45
Copper	0.25	5.03	0.96	12.65

Table 2.1 Optical refractive indices n , κ (source Palik E.D. [49]) and the calculated reflectivity R and penetration (skin) depth ξ of metallic thin films (Al, Pt, Au and Cu) at an optical wavelength λ of 800nm

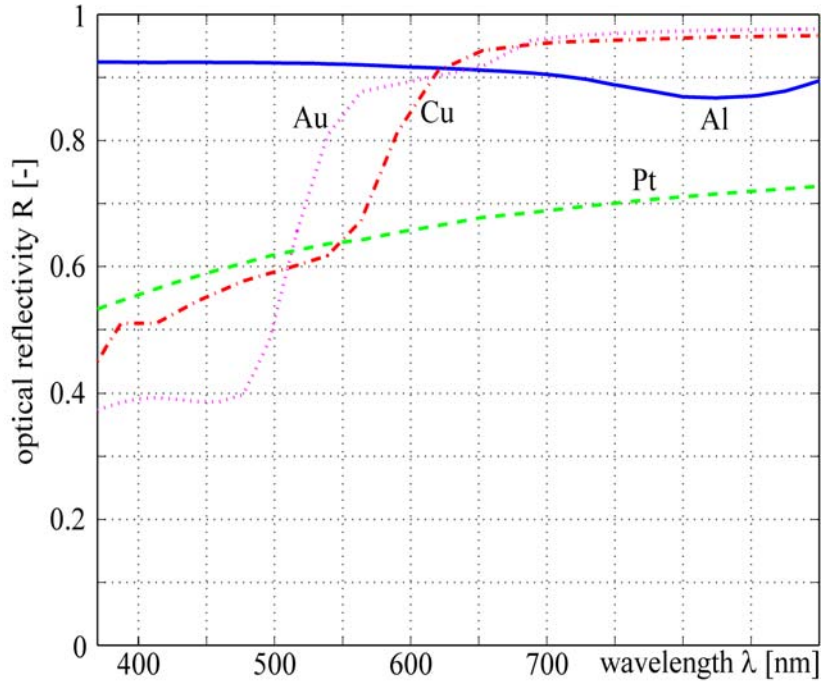


Figure 2.1 Calculated optical reflectivity R with respect to the laser wavelength λ of an Al (solid line), Pt (dashed), Cu (dash-dotted) and Au (dotted) thin film, source of the used refractive indices n and κ is Palik E.D. [49]

In general, the temperature increase ΔT in a solid is calculated with the induced energy E , the mass m and the specific heat capacity c as

$$\Delta T = \frac{E}{cm} \quad (2.5)$$

With the mass $dm = \rho A_s dz$ of the infinitesimal region, where the laser pulse is absorbed, and the absorbed energy of this region $dE(z)$ (2.4) the temperature increase $\Delta T(z)$ yields

$$\Delta T(z) = \frac{(1-R) I_s t_p}{\xi c \rho} e^{\left(-\frac{z}{\xi}\right)} \quad (2.6)$$

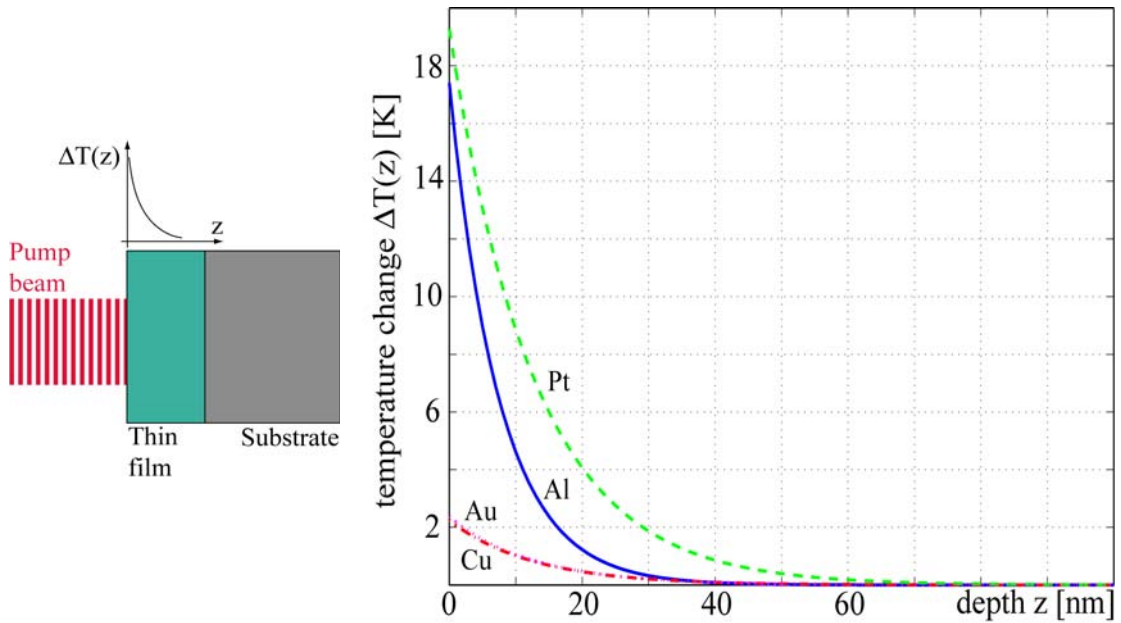


Figure 2.2 Left: illustration of the induced temperature increase $\Delta T(z)$ in thin film; right: induced temperature in an Al (solid line), Pt (dashed), Cu (dash-dotted) and Au (dotted) thin film calculated with Equation (2.6) (right)

The temperature is assumed to be homogeneously distributed in the plane and is exponentially decaying in the thickness direction z with $e^{(-z/\xi)}$ as determined in Equation (2.6) and illustrated in Figure 2.2 (left and right). For the calculation of the induced temperature in Figure 2.2 (right) a laser pulse with 100fs duration (full width at half maximum, FWHM) and a fluence of 2.45J/m^2 which corresponds to a laser pulse energy of 4.8nJ ($\sim 400\text{mW}$ average power in our laser system, repetition rate of 81MHz) and an irradiated spot size of $50\mu\text{m}$ in diameter. At a distance z equal to the absorption length ξ the induced temperature drops to 36.8% of the temperature increase at the surface. The temperature increase at a distance of three times the absorption length 3ξ amounts to only 5%. In other words, the temperature is affected only within a region of three times the absorption length 3ξ by the incident pump pulse. Figure 2.2 (right) shows that the induced temperature change in platinum and aluminium is similar but the temperature increase in copper and gold is very small compared to the changes in aluminium and platinum. It is mainly caused by the higher optical reflectivity of copper and gold (Table 2.1, Figure 2.1). The calculations in Figure 2.2 (right) are done with Equation (2.6) and the values in Table 2.1. In addition, the following literature values for density ρ and heat capacity c are being used

<i>Material</i>	<i>heat capacity c [J/(kg K)]</i>	<i>density ρ [kg/m³]</i>
Aluminium	897	2700
Platinum	133	21500
Gold	129	19300
Copper	385	8960

Table 2.2 Heat capacity and density of Al, Pt, Au and Cu (heat capacity c out of CRC Handbook [11], and density ρ out of CRC Handbook [12])

Further effects such as heat diffusion and the so called hot electron diffusion are not taken into account in this simple model. As one of the following chapters shows, these effects lead to reduction of the peak temperatures and spatial temperature gradients because the heat is strongly spread over the thin film. The stress-strain-temperature relations which correspond to a generalization of the Hooke-Duhamel law is

$$\varepsilon_{ij} = A_{ijkl} \sigma_{kl} + \alpha_{ij} \Delta T \quad (2.7)$$

in which ε_{ij} are the components of the strain tensor, σ_{kl} the components of the stress tensor, A_{ijkl} the elastic compliance tensor, ΔT the temperature increase and α_{ij} the coefficients of linear thermal expansion, which constitute a diagonal-symmetric tensor. Solving Equation (2.7) with respect to σ_{ij} leads to

$$\sigma_{ij} = C_{ijkl} \varepsilon_{kl} - C_{ijkl} \alpha_{kl} \Delta T \quad (2.8)$$

with C_{ijkl} denoting the stiffness tensor and $C_{ijkl} = A_{ijkl}^{-1}$. Assuming isotropic linear elastic material behavior the stiffness tensor C_{ijkl} reduces to

$$C_{ijkl} = \begin{bmatrix} \lambda + 2\mu & \lambda & \lambda & 0 & 0 & 0 \\ \lambda & \lambda + 2\mu & \lambda & 0 & 0 & 0 \\ \lambda & \lambda & \lambda + 2\mu & 0 & 0 & 0 \\ 0 & 0 & 0 & \mu & 0 & 0 \\ 0 & 0 & 0 & 0 & \mu & 0 \\ 0 & 0 & 0 & 0 & 0 & \mu \end{bmatrix} \quad (2.9)$$

with λ and μ as Lamé constants. Since the spot size is very large compared with the absorption length ξ , and film thickness d , the only nonzero component of the strain tensor is ε_z and therefore, Equation (2.8) can be reduced to

$$\sigma_z = (\lambda + 2\mu)\varepsilon_z - (3\lambda + 2\mu)\alpha\Delta T(z) \quad (2.10)$$

So, the stress σ_z in the thin film consists of a mechanical part $\sigma_{z, mech}$ and a thermal part $\sigma_{z, therm}$.

$$\sigma_z = \sigma_{z, mech} + \sigma_{z, therm} \quad (2.11)$$

The thermal stress $\sigma_{z, therm}$ is caused by the instantaneous temperature rise $\Delta T(z, t)$, which is according to Equation (2.10)

$$\sigma_{z, therm} = -(3\lambda + 2\mu)\alpha\Delta T(z, t) \quad (2.12)$$

λ and μ are Lamé constants and α is the linear expansion coefficient. With the equation of motion of the only nonzero component z , the kinematic relation

$$\rho \frac{\partial^2}{\partial t^2}(u_z) = \frac{\partial \sigma_z}{\partial z}; \quad \varepsilon_z = \frac{\partial u_z}{\partial z} \quad (2.13)$$

and Equation (2.10) the strain component caused by the propagating acoustic pulse and the time independent strain component caused by the thermal expansion can be calculated according to Thomsen C. et. al. [81] and Bryner J. [5].

$$\varepsilon_z(z, t) = \frac{(1-R) I_s t_p \alpha}{\xi c \rho} \frac{3\lambda + 2\mu}{\lambda + 2\mu} \cdot \left[e^{\frac{-z}{\xi}} \left(1 - \frac{1}{2} e^{\frac{-c_I t}{\xi}} \right) - \text{sgn}(z - c_I t) \frac{1}{2} e^{\frac{-|z - c_I t|}{\xi}} \right] \quad (2.14)$$

Equation (2.14) is calculated with a stress free boundary condition at the surface of the thin film

$$\sigma_z(z = 0) = 0 \quad (2.15)$$

In case of other configurations, for instance an excitation through a transparent layer, the boundary conditions must be adapted. The effect of the boundary condition on the pulse shape of the acoustic pulse is discussed in Chapter 4.1.1.3 and by Wright O.B. et. al. [88].

The strain pulse is propagating in the thickness direction of the thin film (z direction, Figure 2.3) with the longitudinal wave velocity c_I , which is determined by the Lamé constants and the density of the film.

$$c_I = \sqrt{\frac{\lambda + 2\mu}{\rho}} \quad (2.16)$$

The longitudinal wave velocities c_I of the Al, Pt, Au and Cu thin films are given in the following Table 2.3

<i>Material</i>	<i>calculated bulk wave speed c_1 [m/s]</i>	<i>acoustic reflection coefficient r (stress) on sapphire substrate [-]</i>
Aluminium	6362	0.4080
Platinum	3971	-0.3527
Gold	3212	-0.2055
Copper	4694	-0.014

Table 2.3 Calculated bulk wave speed c_1 in Al, Pt, Au and Cu thin film and acoustic reflection coefficient r of these thin films on a sapphire substrate (source of the used mechanical properties see Appendix A, definition of the acoustic reflection coefficient see Equation (2.17))

The acoustic reflection coefficients listed in Table 2.3 are defined as

$$r = \frac{Z_2 - Z_1}{Z_2 + Z_1} \quad (2.17)$$

where Z_1 and Z_2 are the acoustic impedances of the thin film and the substrate, respectively, and are determined by the wave speed c_1 and the density ρ of the material. If the acoustic impedance of the thin film (Z_1) is higher than the impedance of the substrate (Z_2) a sign change of the acoustic stress pulse occurs. For the calculation of the acoustic reflection coefficient r the density ρ of sapphire was 3990 kg/m^3 , the Young's modulus E is 345 GPa and the Poisson ratio ν was 0.24 (source Appendix A).

Usually the grains of the polycrystalline metallic thin films have arbitrary orientation. The diameter of the irradiated spot size on the surface of the thin film is 2 or 3 orders of magnitude larger than the grain size which is usually in the order of the film thickness. Hence, the measurements are averaged over a large number of grains with various orientations. So for the calculation of the bulk wave velocity c_1 isotropic material behavior is assumed. A fact which is well confirmed by experimental results.

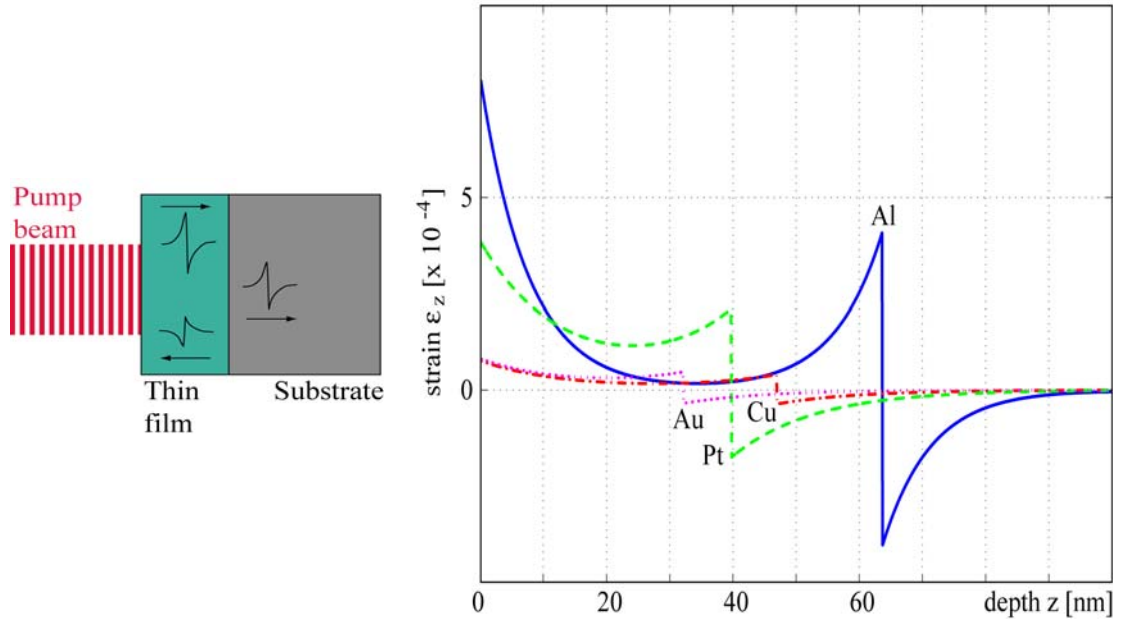


Figure 2.3 Left: illustration of the propagation of the acoustic pulse in thin film; right: strain pulse in an Al (solid line), Pt (dashed), Cu (dash-dotted) and Au (dotted) thin film 10ps after excitation

The quantitative results in Figure 2.3 (right) are based on the induced temperature change presented in Figure 2.2 and the corresponding laser parameters, as well as the mechanical properties of Appendix A. According to Figure 2.3 (left and right) and Figure 2.4 the strain distribution in the thin coating can be divided into two parts: a static part due to the thermal expansion near the free surface and a propagating part with a high frequency content up to several GHz. The propagating strain pulse again consists of two equal components with opposite signs: During the absorption of the laser pulse one part is propagating directly in the positive thickness direction z (part with negative strain) during the absorption of the laser pulse and one originally propagating in the negative direction ($-z$). The second one is instantaneously reflected at the stress free boundary, therefore its strain is positive. The acoustic wavelength and spectrum of the pulse travelling from the boundary into the bulk of the absorbing medium is mainly determined by the optical absorption length (skin depth).

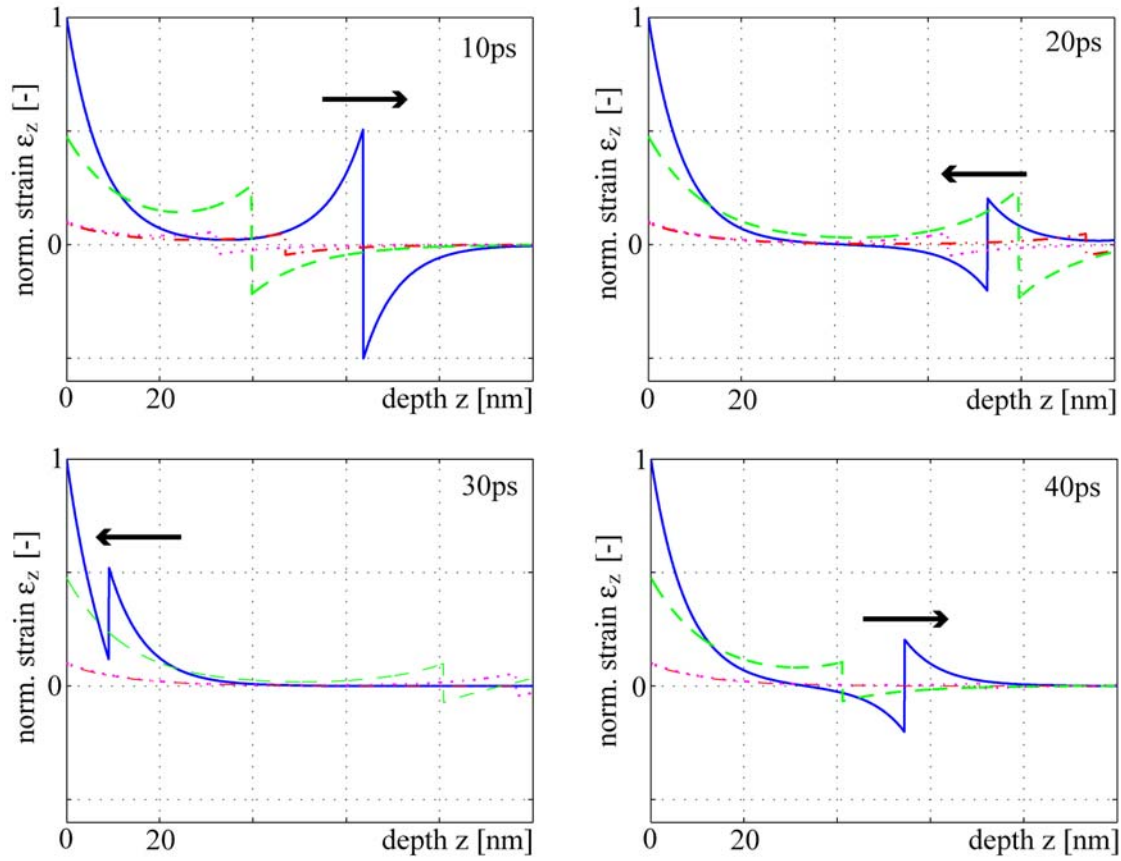


Figure 2.4 Bulk acoustic wave propagation in an Al (solid line), Pt (dashed), Cu (dash-dotted) and Au (dotted) thin film (thickness 100nm) on a sapphire substrate after 10ps, 20ps, 30ps and 40ps (physical properties as well as the laser parameters are the same as in Figure 2.3 (left), the arrow indicates the propagation direction of the acoustic pulse in the aluminium film (solid line))

In Figure 2.4 the propagation of an acoustic pulse in a 100nm Al, Pt, Au and Cu thin film on a sapphire substrate is shown every 10ps. Because the diagrams show only the region of the thin film the right hand side corresponds to the interface of thin film and sapphire substrate. After 10ps the acoustic pulses in all thin films are propagating towards the interface. Again 10ps later the acoustic pulse in the aluminium film has been reflected the first time whereas in the other materials the pulses are still propagating towards the interface. Aluminium has the highest bulk wave speed c_l of the four materials. The reflection coefficient r of the aluminium-sapphire combination amounts to 0.408 and has a positive sign. This means that the amplitude of the reflected acoustic pulse is 40% of the incident and the pulse shape of the incident pulse is the same as the reflected one. The acoustic pulse in the platinum thin film has a smaller amplitude than the pulse in the aluminium case. Also, the acoustic reflection coefficient r is smaller and furthermore has a negative sign. The

variation in signs of the back propagating pulse caused by the different reflection coefficient r is illustrated in Figure 2.4 if the strain distribution in the aluminium and platinum thin films are compared. In the copper case, the reflectivity coefficient is very low, hence, nearly the total acoustic pulse is transmitted into the substrate. This fact should be kept in mind because it is one of the limiting conditions for experiments. Measurements for aluminium thin films and platinum thin films are presented in Chapter 4.

2.2 Numerical modelling

2.2.1 Numerical model of the one-dimensional linear elastic wave propagation

On the one hand the presented analytical model gives a fast but rough idea of the travelling acoustic pulse without extensive calculations. But on the other hand numerical models are more flexible for describing the travelling wave in specimens consisting of a stack of various layers. In addition, numerical models are the only way for calculating the wave propagation in 2 or 3 dimensions. Furthermore, numerical modelling makes it possible to describe the excitation of the acoustic pulses by the induced temperature in a more accurate way.

2.2.1.1 Implementation

For the calculation of hyperbolic differential equations like the wave equation (2.13) it is according to Luh Y. [36] not worthy to use implicit algorithms. The much higher calculation costs do not result in "smoother" solutions as it is the case with parabolic or elliptic differential equations. This is the reason why an explicit staggered algorithm is used. The staggered algorithm presented by Schubert F. et. al. [68] has the advantage of the simple implementation of the boundary condition and in addition this algorithm can also be used in 2D or 3D problems. We follow the deduction of Bryner J. [5] which is equivalent to the one dimensional case of the algorithm presented by Schubert F. et. al. [68]. If the derivative with respect to time of the stress-strain relation (2.10) and the kinematic relation (2.13) is used we get the following set of differential equations:

$$\text{wave equation (Newton): } \rho \frac{\partial^2}{\partial t^2}(u_z) = \frac{\partial \sigma_z}{\partial z} \quad (2.18)$$

$$\text{stress-strain relation: } \frac{\partial \sigma_z}{\partial t} = (\lambda + 2\mu) \frac{\partial \varepsilon_z}{\partial t} + \frac{\partial \sigma_{z, therm}}{\partial t} \quad (2.19)$$

$$\text{kinematic relation: } \frac{\partial \varepsilon_z}{\partial t} = \frac{\partial^2 u_z}{\partial t \partial z} \quad (2.20)$$

$\sigma_{z, therm}$ is the thermal excitation (2.12) induced by the absorbed laser pulses. If the velocity is introduced

$$v_z = \frac{\partial u_z}{\partial t} \quad (2.21)$$

the resulting set of equations is

$$\frac{\partial v_z}{\partial t} = \frac{1}{\rho} \frac{\partial \sigma_z}{\partial z} \quad (2.22)$$

$$\frac{\partial \sigma_z}{\partial t} = (\lambda + 2\mu) \frac{\partial v_z}{\partial z} + \frac{\partial \sigma_{z, therm}}{\partial t} \quad (2.23)$$

Equations (2.22) and (2.23) are now discretized in the time and space domain. In the space domain the grid as presented in Figure 2.5 is used.

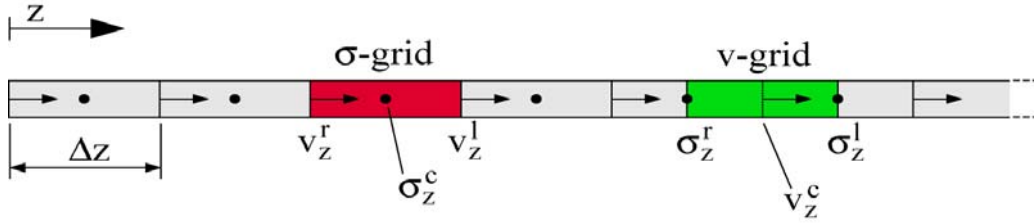


Figure 2.5 Discretization in space domain of the staggered algorithm

In the following 1-D spatial discretization the z -direction corresponds to the thickness direction of the thin film/substrate configuration and the superscripts c , r and l denote the center, right and left of the corresponding grid-cell. The spatial discretization of Equation (2.22) and Equation (2.23) is now as follows

$$\frac{\partial v_z^c}{\partial t} \approx \frac{1}{\rho} \frac{\sigma_z^r - \sigma_z^l}{\Delta z} \quad (2.24)$$

$$\frac{\partial \sigma_z^c}{\partial t} \approx (\lambda + 2\mu) \frac{v_z^r - v_z^l}{\Delta z} + \frac{\partial \sigma_{z, therm}^c}{\partial t} \quad (2.25)$$

The temporal discretization is realized in a similar way

$$\frac{\partial}{\partial t} f(T) \approx \frac{f(T + \Delta t) - f(T - \Delta t)}{2\Delta t} \quad (2.26)$$

The derivative of function f is estimated at time T with Equation (2.26) in

which Δt denotes the time-step. If this equation is rewritten one can estimate the function at time $T + \Delta t$

$$f(T + \Delta t) \approx f(T - \Delta t) + \dot{f}(T)2\Delta t \quad (2.27)$$

With Equation (2.27) and a staggered grid in time domain similar to Schubert F. et. al. [68] the temporal integration is

$$v_z(T) \approx v_z(T - \Delta t) + \dot{v}_z\left(T - \frac{\Delta t}{2}\right)\Delta t \quad (2.28)$$

$$\sigma_z\left(T + \frac{\Delta t}{2}\right) \approx \sigma_z\left(T - \frac{\Delta t}{2}\right) + \dot{\sigma}_z(T)\Delta t \quad (2.29)$$

The finite difference equations (2.24)-(2.29) approximate the derivatives by truncated Taylor series. Therefore, inaccuracies occur which can usually not completely be omitted but can be reduced by choosing the right step size in time and space domain. For reducing numerical dispersion which results from frequency dependent velocity errors, the propagating acoustic pulse must be sufficiently sampled in space domain. According to Leutenegger T. [33] this leads to the following condition

$$\Delta z \leq \frac{1}{8} \frac{c_l}{f_{max}} \quad (2.30)$$

It is obvious that the travelling acoustic pulse (Figure 2.3 (right)) has high frequency content which is caused by the abrupt sign change. Therefore the spatial grid has to be chosen fine enough to reduce errors caused by the numerical dispersion.

To avoid the exponential growth of the amplitude during calculation, it is necessary to choose a time step Δt which is limited in size by Equation (2.31)

$$\Delta t \leq \frac{\Delta z}{c_l} \quad (2.31)$$

The critical time step Δt is governed by the Neumann stability analysis (Leutenegger T. [33]) applied to this one dimensional scheme. The special case in which

$$\Delta z = \Delta t c_l \quad (2.32)$$

is called magic time step, because of the remarkable properties of the resulting finite difference expressions. The solution of the finite difference scheme is also an exact solution of the wave equation (2.18) despite of the approximation by Taylor series (Taflove A. et. al. [76]). Numerical dispersion is totally avoided if the magic time step (2.32) is applied to solve the discretized equations. Appendix B is dedicated to the discussion of the magic time step.

The spatially staggered finite difference scheme has a big advantage in the simple implementation of the mechanical boundary conditions. In the following two special cases - the stress free boundary and the rigid fixing - are discussed. On a stress free boundary the stress in normal direction vanishes at the surface. An illustration of the implementation of the boundary condition is presented in Figure 2.6.

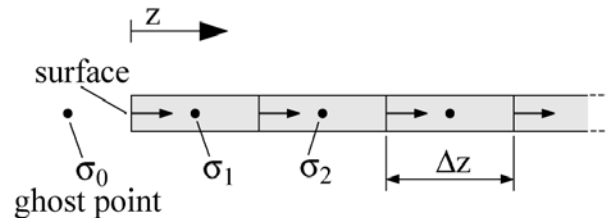


Figure 2.6 Implementation of a stress free boundary

The grid cells are chosen in a way that on the physical boundary of the specimen lies a grid point for the calculation of the velocity - illustrated by an arrow in Figure 2.6. For the implementation an additional grid point - a "ghost point" (σ_0) outside of the specimen is set to the negative value of the occurring stress on the first grid point (σ_1) inside the physical boundary.

$$\sigma_0 = -\sigma_1 \quad (2.33)$$

The approximation of the velocity is determined by the interpolation of the neighboring stress grid points (2.24). Therefore, the stress on the surface vanishes due to the value of the "ghost point".

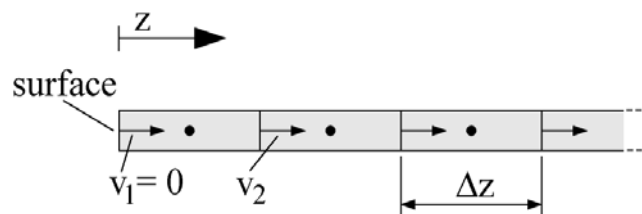


Figure 2.7 Implementation of a rigid boundary

To implement a rigid boundary is even easier since the grid point for the calculation of the velocity is on the surface which is simply set to zero.

$$v_1 = 0 \quad (2.34)$$

2.2.1.2 Discussion

Figure 2.8 shows the bulk wave propagation in an aluminium film on a sapphire substrate calculated with the presented finite difference scheme. In the aluminium part as well as in the sapphire substrate the magic time step is applied to the solution of the finite difference approximation. For the pre-

sented results a time step Δt of 4fs is chosen. The spatial step size of the grid in both media is determined by the wave speed c_l and the time step Δt (2.32). As the results show the expected numerical dispersion due to the very high frequency content of the acoustic signal is completely eliminated by means of magic time step. Nevertheless, slight differences arose when comparing the analytical solution (Figure 2.4) and the numerically calculated results (Figure 2.8). The spatial grid is slightly too rough for sampling the sharp positive and negative peaks (marked by dashed circles in Figure 2.8) occurring at the sign change of the travelling acoustic pulse. Far enough from the surface the normalized propagating strain pulse should have an amplitude of ± 0.5 and the peak-peak amplitude should always be 1 as in the analytical solution (Figure 2.4). By reducing the temporal and the spatial step size as well, this inaccuracies of the sampling can nearly be eliminated.

At interface of thin film and substrate the propagating acoustic pulse is reflected according to the acoustic reflection coefficient r (2.17). The ratio of the amplitudes of the incident and the reflected stress pulse is 0.408 and because of the linear elastic stress-strain-relation the ratio is the same for the strain pulse. Since the impedance of the substrate is higher than the impedance of the thin film the amplitude of the transmitted stress pulse with respect to the incident one is >1 . The amplitude of the transmitted strain pulse is in the order of the reflected one because the substrate (sapphire) is much stiffer than the thin film. The higher bulk wave velocity in the sapphire substrate leads to a slightly broader pulse which can be observed comparing reflected and transmitted strain pulse.

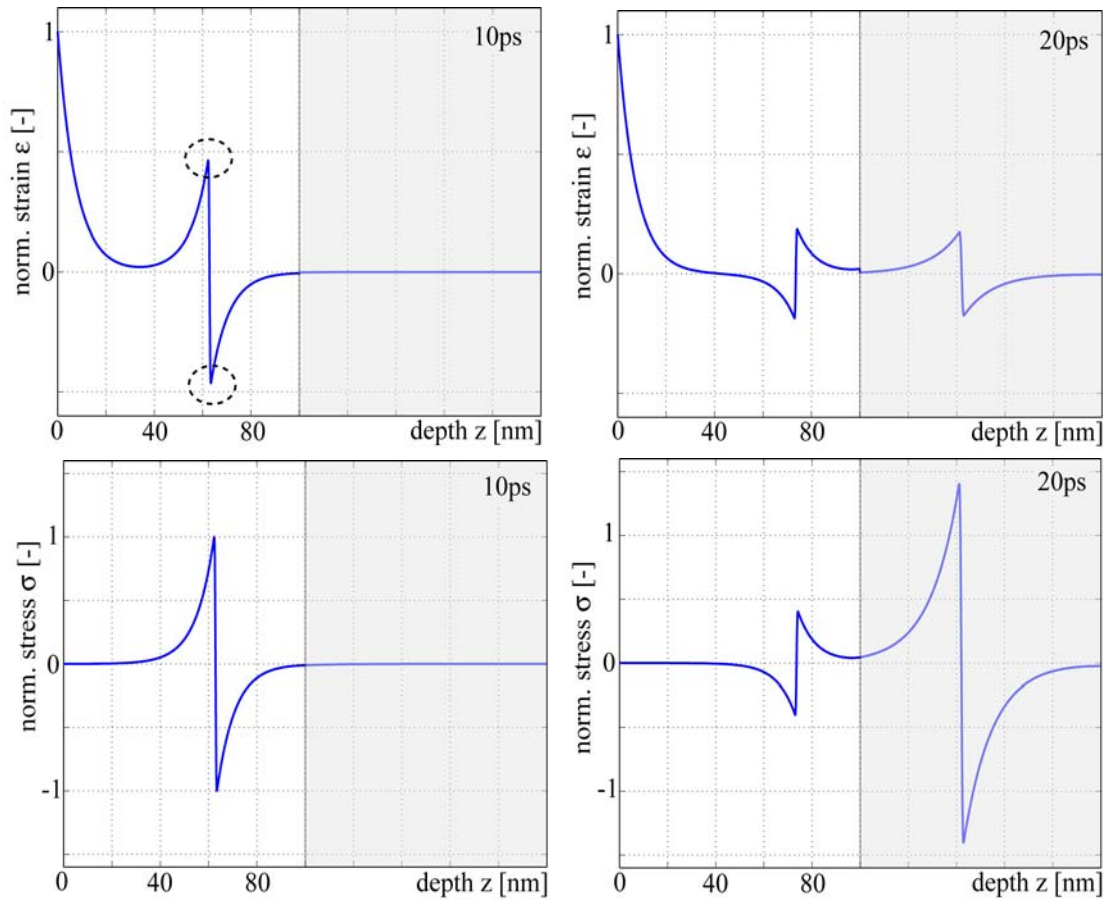


Figure 2.8 Simulated strain (top) and stress (bottom) in a 100nm aluminium film on a sapphire (gray) substrate (left at 10ps, right at 20ps)

This numerical solution enables the implementation of more accurate descriptions of the laser induced transient heating in the surface region which is the subject matter of the following two chapters.

2.2.2 Numerical model for the ultrashort pulse laser heating

As mentioned before, the heat conduction inside the thin film has not been considered in the excitation of the mechanical strain pulses. But while and after the laser pulse is absorbed the heat diffuses into underlying layers and the substrate. A numerical solution of the heat conduction equation enables the consideration of the temporal laser pulse shape which can be very interesting since the acoustic pulse shape can be modified with the appropriate laser pulse or laser pulse train.

2.2.2.1 Theoretical considerations

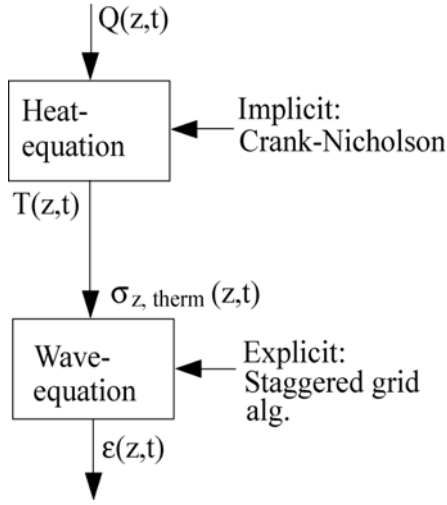


Figure 2.9 Algorithm for the solution of the heat and wave equation

Due to the heat conduction the induced temperature is not constant in time domain thus the thermal induced stress varies. So the excitation varies in time and space

$$\sigma_{z, therm} = -(3\lambda + 2\mu) \alpha \Delta T(z, t) \quad (2.35)$$

The feedback of the resulting strain or displacement, respectively, on the simulation of the induced temperature is neglected because of its very small contribution, thus the two parts can be performed sequentially. For determining the varying temperature distribution the heat conduction equation must be solved which leads to a complete solution as illustrated in

Figure 2.9. First, an implicit Crank-Nicholson scheme (Strauss W.A. [74]) is applied for calculating the temperature distribution. Secondly, the wave propagation problem is solved numerically with an excitation described in Equation (2.35).

2.2.2.2 Implementation

The heat conduction is described by the following parabolic partial differential equation

$$\frac{\partial T}{\partial t} = \frac{K}{C} \frac{\partial^2 T}{\partial z^2} + \frac{1}{C} Q \quad (2.36)$$

K denotes the thermal conductivity, C the heat capacity and $Q(z, t)$ is the source term related to the absorbed energy of the incident laser pulse. According to Strauss W.A. [74] the equation is discretized with the \mathfrak{G} -scheme

$$\begin{aligned} \frac{T(z)^{k+1} - T(z)^k}{\Delta t} &= (1 - \mathfrak{G}) \frac{T(z+1)^k - 2T(z)^k + T(z-1)^k}{(\Delta z)^2} + \\ &+ \mathfrak{G} \frac{T(z+1)^{k+1} - 2T(z)^{k+1} + T(z-1)^{k+1}}{(\Delta z)^2} \end{aligned} \quad (2.37)$$

which yields for Equation (2.36)

$$\begin{aligned}
& -\frac{\Delta t K \mathcal{G}}{C(\Delta z)^2} T(z+1)^{k+1} + \left(\frac{2\Delta t K \mathcal{G}}{C(\Delta z)^2} + 1 \right) T(z)^{k+1} - \frac{\Delta t K \mathcal{G}}{C(\Delta z)^2} T(z-1)^{k+1} = \\
& = \frac{\Delta t K (1 - \mathcal{G})}{C(\Delta z)^2} T(z+1)^k + \left(-\frac{2\Delta t K (1 - \mathcal{G})}{C(\Delta z)^2} + 1 \right) T(z)^k + \\
& + \frac{\Delta t K (1 - \mathcal{G})}{C(\Delta z)^2} T(z-1)^k + \frac{\Delta t}{C} Q(z) \tag{2.38}
\end{aligned}$$

Δt is the temporal step size, Δz the step size in the space domain. k denotes the number of the actual time step and z the number of the actual spatial step. Q is the source in W/m^3 and \mathcal{G} the so-called \mathcal{G} -parameter. The special case of \mathcal{G} equal to $1/2$ is the well-known Crank-Nicholson-scheme which is stable for arbitrary temporal Δt and spatial Δz step sizes.

In a first step the boundary conditions for an adiabatic system are implemented. Consequently, the heat flux out of the simulated region (thin film) must vanish, which is equivalent to a vanishing derivative of the temperature with respect to z . Thus for all time steps k the finite difference (2.39) is valid at the boundary

$$\frac{T(2)^k - T(0)^k}{2\Delta z} = 0 \tag{2.39}$$

Equation (2.39) yield

$$T(0)^k = T(2)^k \tag{2.40}$$

and similar for the back surface or interface, respectively.

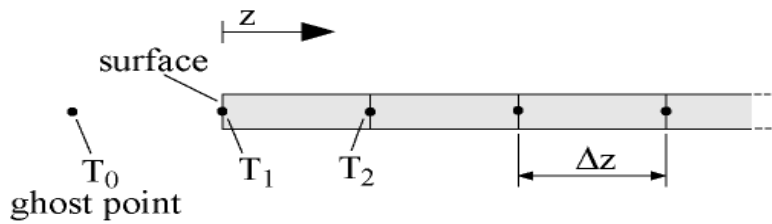


Figure 2.10 Implementation of the adiabatic boundary condition

2.2.2.3 Discussion

Shortly after absorption of the ultra-short laser pulse the induced temperature change is approximately the same as the analytical solution which is shown if the results in the corresponding figures (Figure 2.2 and Figure 2.11 (solid line, right)) are compared. Then the heat diffuses into the thin film and after several tens of picoseconds - depending on the thermal conductivity - the thin film is

in thermal equilibrium. All results of the following figures are calculated using the same laser parameters as previously used. The 100nm aluminium film is exposed to laser pulses (FWMH) with 100fs duration and 4.8nJ pulse energy. It is assumed that the spot on the surface has a diameter of 50 microns. For the adiabatic solution a spatial grid size Δz of 1nm and a step size in the time domain Δt of 2fs is used. Variations of the step size both in time and space domain showed no significant change in the simulation accuracy. A reduction of the grid size in time or space domain to the half of the usual values leads to maximal variations of the induced temperature change (ΔT) below 0.5%.

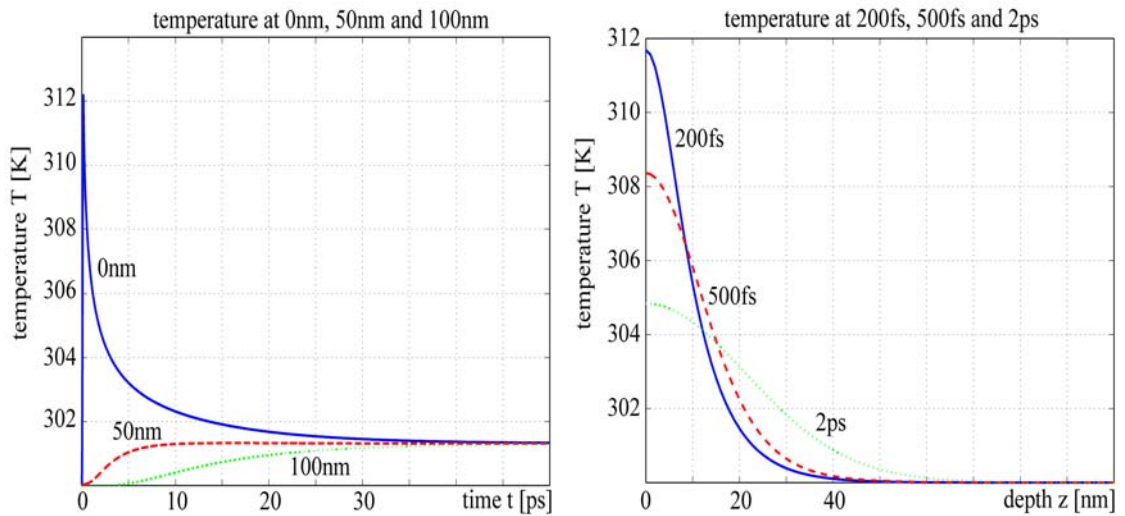


Figure 2.11 Temperature increase in a 100nm aluminium thin film (adiabatic system with boundary conditions according to Equation (2.40)) after absorbing a 100fs (full width at medium height - FWMH) ultra-short laser pulse; left: with respect to time (at the free surface - solid line, at a depth of 50nm - dashed line and at the back surface (100nm) - dotted line); right: with respect to thickness (after 200fs - solid line, after 500fs - dashed line and after 2ps - dotted line)

The main difference of the analytical and the discrete model is that the temperature in the thin film is not constant anymore but diffuses into the thin film. Since the temperature is varying with time at every spatial point, a non-symmetric travelling strain pulse is excited. The shape of the strain pulse is mainly determined by the ratio

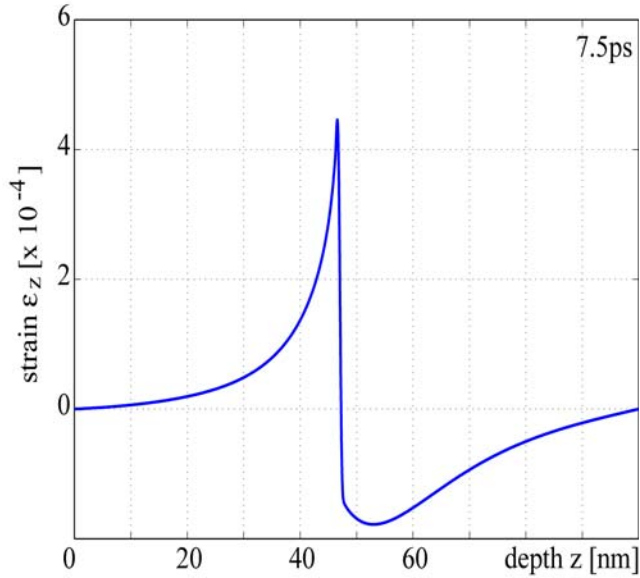


Figure 2.12 Excited strain pulse (only the propagating part) in an 100nm aluminium thin film (freestanding) calculated with numerical modelling of heat conduction (adiabatic) and wave propagation

$$\frac{D}{c_l \xi} \quad (2.41)$$

in which $D=K/C$ denotes the ratio of the thermal conductivity K and C the heat capacity (Thomsen C. et. al. [81]). If the ratio (2.41) is comparable to 1 the changes affected by heat diffusion must be considered. On the other hand if the ratio (2.41) is much smaller than 1 ($\ll 1$) the effect on the strain pulse can be disregarded, because the acoustic pulse has left the heated region before the heat transport affects its shape.

The strain pulse presented in Figure 2.12 is calculated using the finite difference scheme

described previously, applying the magic time step (2.32) and a step size in the time domain Δt of 10fs. Figure 2.3 shows that the positive part of the strain pulse has the same amplitude but the negative part is strongly influenced by the heat conduction.

2.2.3 Non-equilibrium numerical modelling of the ultrashort laser pulse heating

Experiments on metallic thin films, above all, on thin films of materials such as copper or gold showed a very strong heat flux during the short time period of absorption of the laser pulse. This strong heat flux is caused by non-equilibrium heating during the first picosecond after the incidence of the laser pulse which can not be described with the previous models of Chapter 2.1 and Chapter 2.2.2. Therefore in this chapter the concept of non-equilibrium heating is introduced and the corresponding models are discussed. In the following it is shown, that the non-equilibrium heating has a significant effect on the amplitude and distribution of the induced temperature increase and therefore on the amplitude and shape of the excited acoustic pulse. Especially with decreasing dimensions of thin films or microstructures, respectively, the non-equilibrium heating must be considered in an appropriate model.

Apart from the application of such models for describing the excitation of

acoustic pulses the accurate prediction of the thermally affected zone is usually important for high-precision controllability, since manufacturing technology progresses into the nanoscale area. Meanwhile ultrashort pulse lasers are becoming common for cutting foils and thin sheet metals or for structuring metallic coatings, for instance, because of their tremendous pulse but low average power.

According to Qiu T.Q. et. al. [59] there exist basically two different models describing the mechanism of energy transport during short-pulse laser heating. One is based on the hyperbolic heat conduction model (Tzou D.Y. [83]) which was first postulated for gases by Maxwell in 1867. A second model is based on the thermal non-equilibrium concept of microscopic energy carriers, i.e., electrons and phonons having different temperatures during the heating process (Kaganov M.I., et.al. [28], Anisimov S.I., et. al. [1] and Qiu T.Q. et. al. [58]). The latter has been adapted, numerically implemented and connected with the modelling of wave propagation in a similar way as shown in Figure 2.9.

2.2.3.1 Theoretical considerations

The non-equilibrium short-pulse laser heating of metals consists of two major steps:

- 1) The absorption of the laser radiation by the electrons due to their very small heat capacity
- 2) The transmittance of the energy from the electrons to the lattice system by an inelastic electron-phonon scattering process

The transmittance of the energy from the electrons to the lattice depends on the material properties and takes about 0.1-1ps until the electrons and lattice are just about in thermal equilibrium [59]. If the laser pulse duration is in the same order or shorter than this time period, an appropriate thermal model is necessary to describe the heating of the material. This non-equilibrium heating process can be described by the hyperbolic two step model which can be simplified for most cases to the parabolic two-step radiation heating model (PTS, Qiu T.Q. et. al. [61]) or simply the two-temperature model. The two-temperature model was first proposed by Anisimov S.I., et. al. [1], based on the work of Kaganov M.I., et.al. [28]. The two-temperature model is described with the following equations

$$C_e(T_e)\frac{\partial T_e}{\partial t} = \nabla(K_e \nabla T_e) - G(T_e - T_l) + Q \quad (2.42)$$

$$C_l \frac{\partial T_l}{\partial t} = G(T_e - T_l) \quad (2.43)$$

presented by Qui T.Q. et. al. [61]. T_e , T_l , C_e , C_l and K_e are the temperature, heat capacity and thermal conductivity of the electron (e) and the lattice (l) system, respectively. G is the electron-lattice coupling constant and Q the laser heating source term. Due to the small ratio between film thickness d or absorption length ξ and diameter of the irradiated spot, which is in the order of 10^{-3} , the coupled differential equations are solved in one dimension with the coordinate z perpendicular to the surface of the thin film. In plane heat conduction in the thin film is neglected. The temperature dependence of the electron heat capacity $C_e(T_e)$ and the thermal conductivity $K_e(T_e)$ are given by

$$C_e(T_e) = \gamma T_e \quad (2.44)$$

$$K_e(T_e) = K \frac{T_e}{T_l} \quad (2.45)$$

in which γ is the electron specific heat constant and K the thermal conductivity at equilibrium (Tas G. et. al. [79], Hostetler J.L. et. al. [24]). Heat transport through the film-substrate interface is assumed to be negligible in the electron system. In the lattice system the heat flux through the interface is disregarded for these first series of computations, but in the results presented in Chapter 4.1.3.3 it is taken into account according to

$$C_l \frac{\partial T_l}{\partial t} = \nabla(K_l \nabla T_l) + G(T_e - T_l) \quad (2.46)$$

In general, the heat conduction in the lattice is considered if the coatings are thin and therefore the acoustic pulse shape is significantly influenced. The source term $Q(z, t)$ is defined as

$$Q(z, t) = I(t) \frac{(1-R) J}{\xi A_s} \cdot e^{-\frac{z}{\xi}} \quad (2.47)$$

in which R represents the optical reflectivity of the thin film. The reflectivity R as well as the absorption length ξ are wavelength dependent. A_s denotes the irradiated area, J the pulse energy, and $I(t)$ the time profile of the femtosecond pump pulses.

2.2.3.2 Implementation

The equations (2.42) and (2.43) are solved numerically with a Crank-Nicholson-scheme (2.37) [13] with a constant grid spacing and also considering addi-

tionally the temperature dependent thermal properties (2.44) and (2.45). Usually, a maximum grid spacing of 1nm is chosen and it is also assumed, that the boundary at the free surface and at the interface, respectively, is thermally insulated in the electron and lattice system. In the lattice system the thermal properties (heat capacity) are kept constant, which is a good approximation since the induced temperature change is very small. The derivative of the temperature with respect to the time is estimated with a forward differential coefficient. If this simulation is used together with a numerical solution of the wave equation it is connected with the resulting lattice temperature by adapting Equation (2.35)

$$\sigma_{z, therm} = -(3\lambda + 2\mu) \alpha \Delta T_l(z, t) \quad (2.48)$$

2.2.3.3 Results and Discussion

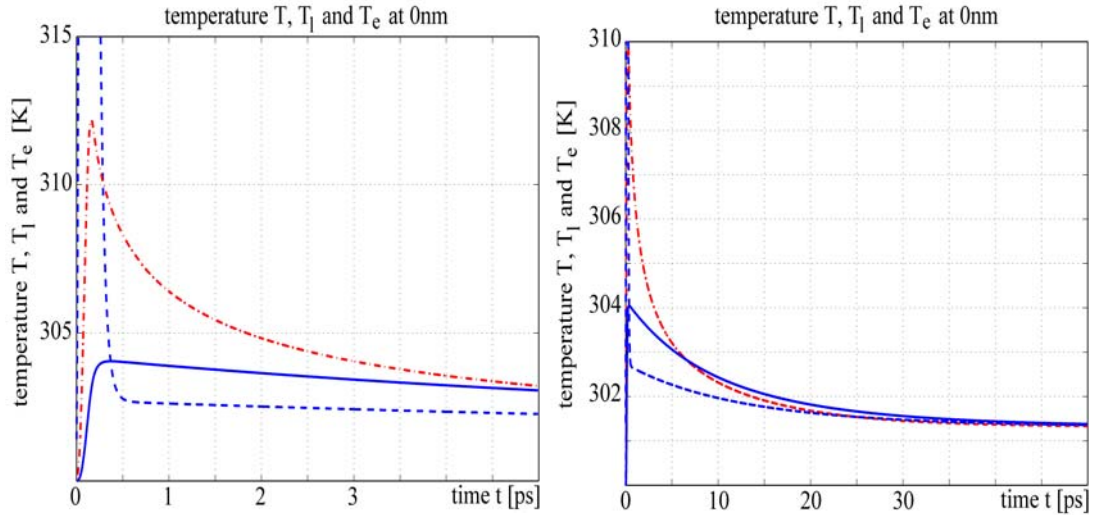


Figure 2.13 Induced temperature calculated with the non-equilibrium model (lattice system - solid line, electron system - dashed line) and with the one-temperature model (dash-dotted line)

The small heat capacity of the electron system enables that during the absorption of the ultrashort laser pulse the temperature in the electron system rises very fast. In most common metal films the electron heat capacity at room temperature C_{e0} [30] is two orders of magnitude smaller than the heat capacity of the lattice C_l , which is in the order of the bulk value C . The heat capacity of the lattice is kept constant because the induced temperature change is small and is calculated from $C = C_{e0} + C_l$. In cases with higher temperature changes, such as applications of ultrashort pulse lasers in manufacturing technology, the lattice heat capacity variations caused by the increased temperature must be taken also into account [7]. Compared with the electron system the lattice tem-

perature rises much more slowly, which means that during the absorption of the laser pulse in the first hundreds of femtoseconds the difference of the temperature in the lattice and electron system is the highest (compare Figure 2.14 and Figure 2.15). Consequently the temperature dependent electron heat conductivity (2.45) is the highest during and shortly after absorbing the laser pulse. Hence, the electron temperature is distributed nearly uniform in the film after the first picoseconds which can be observed in Figure 2.14.

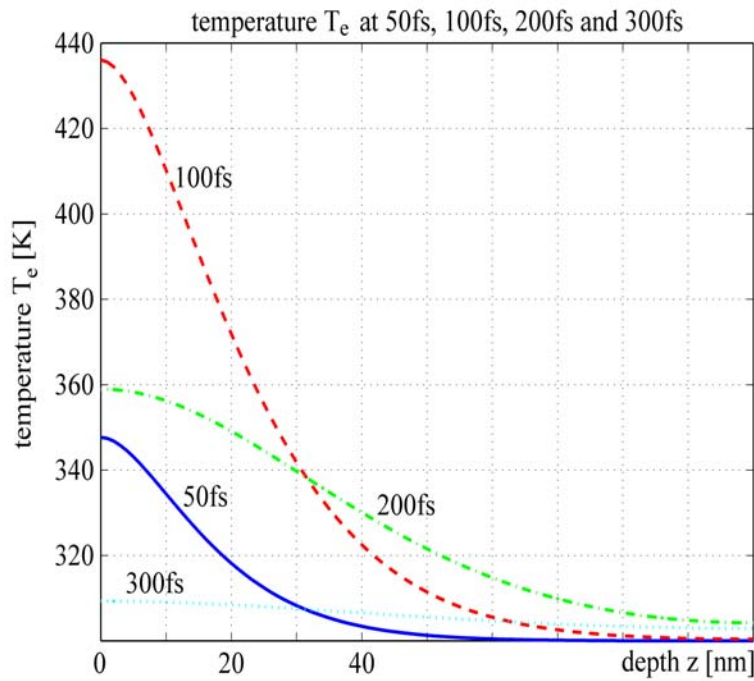


Figure 2.14 Electron temperature at 50fs (solid line), 100fs (dashed line), 200fs (dash-dotted) and 300fs (dotted) after incidence of the laser pulse

Simultaneously the energy of the electrons is transferred through electron-phonon collision to the lattice. The intensity of the coupling depends on the electron-phonon coupling parameter G which is strongly material dependent. An overview of the electron-phonon coupling G of 8 different metal films is given by Hohlfeld J. et. al. [23] where also values of the electron specific heat constant, thermal diffusivity and the thermal conductivity

can be found. The coupling parameter G of aluminium is chosen from Tas G. et. al. [79]. If the value of the electron-phonon coupling G is low i.e. for gold and copper films, the electrons may diffuse significantly more than in cases where the coupling is stronger (i.e. aluminium, chromium). Thus, the spatial area over which the energy is spread is much larger than calculated with the previous models of Chapter 2.1 and Chapter 2.2.2. Therefore, the induced lattice temperature is much lower than determined before, but is being distributed over a much wider region.

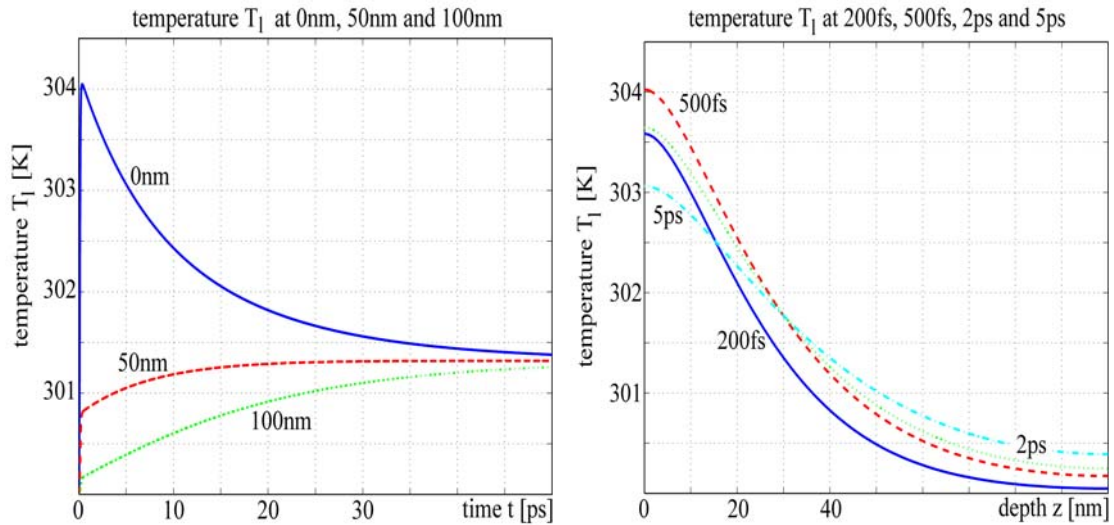


Figure 2.15 Left: lattice temperature in a 100nm aluminium (freestanding, adiabatic) thin film plotted with respect to time (at the free surface - solid line, at a depth of 50nm - dashed line and at the back side (100nm) - dotted line); right: spatial distribution of the lattice temperature (after 200fs - solid line, after 500fs - dashed line, 2ps - dash-dotted line and after 5ps - dotted line)

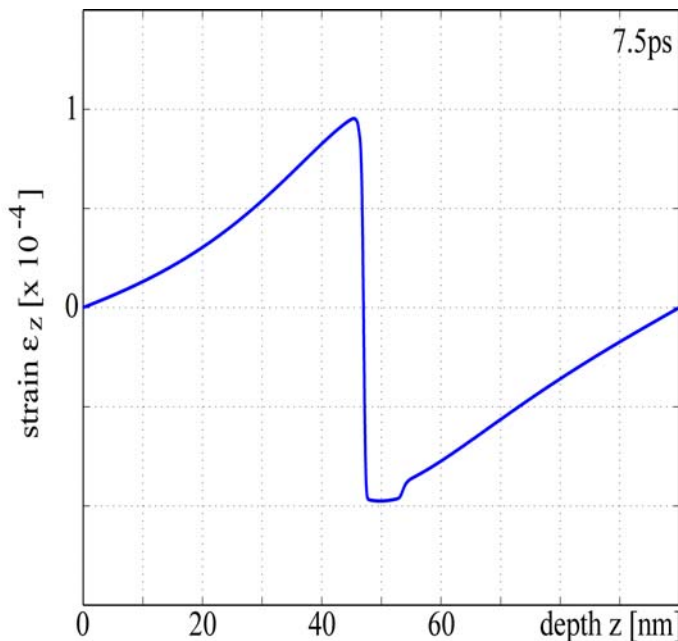


Figure 2.16 Excited strain pulse (only the propagating part) by the induced temperature calculated with the two-temperature model in a 100nm aluminium film (freestanding)

Hence it follows that the amplitude of the acoustic pulse must be smaller. This is the case if the amplitude of the acoustic pulse in Figure 2.16 ($\sim 1 \times 10^{-4}$) is compared with the strain pulses in Figure 2.12 ($\sim 4.5 \times 10^{-4}$) and Figure 2.3. ($\sim 4.5 \times 10^{-4}$). In addition Figure 2.16 shows also a significant broadening of the acoustic pulse due to increased heat conduction even for aluminium thin films. In copper or gold films this effect is much stronger. If the film thickness is sufficiently thin (in the order of 100nm depending on the material)

the temperature change at the back of the thin film (in Figure 2.16 on the right hand side) excites also a propagating acoustic pulse which travels towards the front surface. The amplitude of the acoustic pulse excited at the back of the thin film depends on the strong initial temperature increase at the back during and shortly after the absorption of the laser pulse. The amplitude of this additional pulse depends on the boundary conditions and the induced temperature increase at the back. In general, an additional acoustic pulse can be expected if a sharp increase of the temperature is induced on boundaries or interfaces of different thin films. In the example presented, in Figure 2.16, the strain pulse excited at the front surface covers a distance of approximately 47nm after 7.5ps. The acoustic pulse excited at the back of the film propagates the same distance and occurs in Figure 2.16 as a small step at a position z of approximately 53nm.

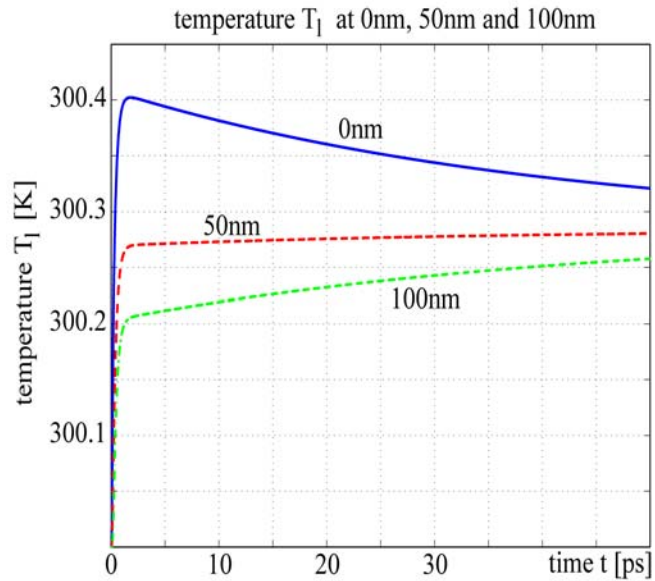


Figure 2.17 Calculated lattice temperature in a 100nm freestanding copper thin film (adiabatic) (free surface - solid line, depth of 50nm - dashed, depth of 100nm - dotted line)

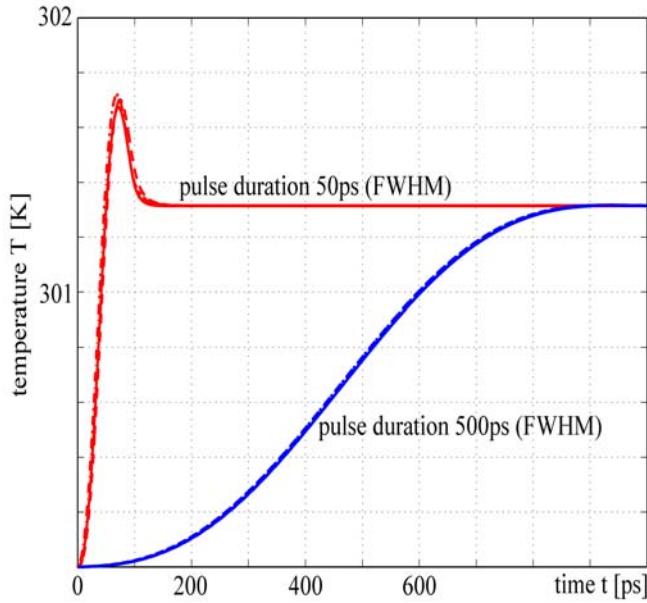


Figure 2.18 Temperature of electron and lattice system, respectively calculated with the two- and for comparison with the one-temperature model in a 100nm aluminium film (freestanding, adiabatic) (lattice system - solid line, electron system - dashed line) and with the one-temperature model (dash-dotted line)

It is important to consider this phenomenon if the film becomes thinner or the electron-phonon coupling G is low because this leads to a stronger initial temperature increase at the back of the thin film. For example: for a copper thin film with thickness of 100nm deposited on silicon substrate the acoustic pulse excited at the interface is in same order of magnitude than the pulse excited at the front surface (see Figure 4.20). Figure 2.17 shows the temperature distribution in a 100nm copper film after absorption of a 100fs (FWHM) laser pulse. In general the temperature increase in a copper film is much lower than in aluminium due to the higher optical reflectivity. In addition, the

lower electron-phonon coupling yields a nearly uniform temperature distribution shortly after absorbing the laser pulse, because the electrons can diffuse over a larger distance, before they are losing their energy. A fact which usually leads to two propagating acoustic pulses except in films thicker than about 500nm. In such cases the two pulses propagating in opposite directions add up to a standing bulk wave i.e. a resonance in the thickness direction of the thin film. Corresponding measurements on copper have been presented in [47].

If the electron-phonon coupling is very high or if the electrons and the lattice are in thermal equilibrium, equations (2.42) and (2.43) reduce to the classical Fourier law (2.36). Thermal equilibrium arises if the pulse duration is much larger than the electron-lattice thermalization time. Two such results are shown in Figure 2.18. During the absorption time of the 50ps (FWHM) pulse as well as during the 500ps (FWHM) pulse the electrons and the lattice are in thermal equilibrium. In both cases, the obtained results match the solution of the classical Fourier law (2.36) very well.

All laser parameters are the same as used previously, that is to say that the

pulse energy fluence is 2.45J/m^2 and the duration amounts to 100fs (FWHM). The material and thermal properties of the aluminium and copper film are given in Appendix A.

2.3 Further aspects of the propagation characteristics of the acoustic pulses

2.3.1 Surface roughness

The wavelength of the excited high frequency acoustic pulses in the metallic thin film is in the nanometer range. Since the surface roughness is in the same order of magnitude this section deals with the effects of surface roughness on the propagating acoustic pulse.

In the paper of Zhu T.C. et. al. [95] the influence of the surface roughness on the attenuation of the acoustic pulse is discussed with the assumption of a nearly constant film thickness. If the film thickness is constant only the variations of the acoustic path lengths cause an attenuation of the acoustic pulse (see Figure 2.19). These variations of the acoustic path length are proportional to the film thickness (Zhu T.C. et. al. [95]) and therefore the broadening of the acoustic pulses increases with increasing film thickness.

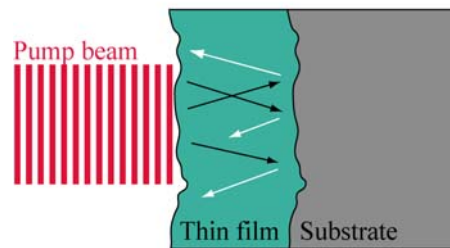


Figure 2.19 Influence of the surface roughness

The interface roughness and slight changes of the film thickness have an additional influence, which is illustrated by the paper of Natarajan A. et. al. [46] which shows acoustic pulse broadening caused by rough interfaces.

Furthermore, the absorption and reflection of light is affected by the surface roughness.

2.3.2 Limits of continuum-mechanics

From the governing differential equation, the wave propagation velocity is determined by the stiffness tensor and the density and hence, it is constant. The acoustic wave propagation in 1D can be understood at the microscopic level by a mass and spring model which is well known in solid state physics. Atomic layers are modeled as hard spheres with the corresponding masses,

and the interatomic forces are modeled with springs of different spring constants.

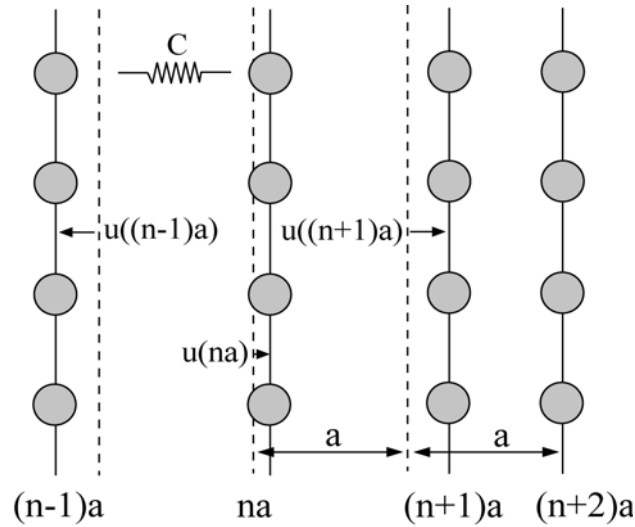


Figure 2.20 Illustration of the one spring constant atomic model (1D)

The forces which act on the atom at position na are

$$F(na) = C [u((n+1)a) - u(na)] + C [u((n-1)a) - u(na)] \quad (2.49)$$

The equation of motion of the atom at position na and the force given by Equation (2.49) leads to

$$M \frac{d^2}{dt^2} u(na) = C [u((n+1)a) + u((n-1)a) - 2u(na)] \quad (2.50)$$

M is the mass of an atom, C the appropriate spring constant and a denotes the spacing between the atoms. Assuming harmonic oscillations of the masses with a frequency ω

$$-\omega^2 M u(na) = C [u((n+1)a) + u((n-1)a) - 2u(na)] \quad (2.51)$$

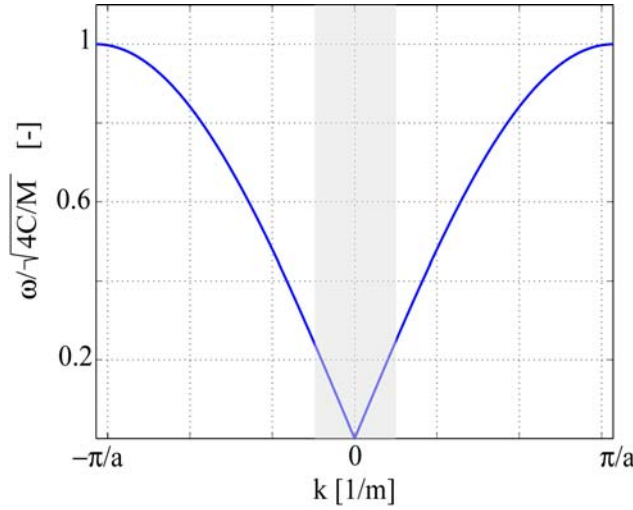


Figure 2.21 Plot of the dispersion relation (2.54) - first Brillouin zone (illustration: the occurring wave numbers of an acoustic pulse in an aluminium film are grey underlaid)

Equation (2.50) reduces to (2.51) with propagating waves according to Equation (2.52)

$$u(na) = u e^{-inak} \quad (2.52)$$

as a solution in which k denotes the wave number. Equation (2.51) and (2.52) lead to the dispersion relation of the travelling waves

$$\omega^2 = \frac{2C}{M} (1 - \cos(ka)) \quad (2.53)$$

or

$$\omega^2 = \frac{4C}{M} \left(\sin\left(\frac{1}{2}ka\right) \right)^2 \quad (2.54)$$

In the long wavelength limit ($ka \ll 1$) the dispersion relation

reduces with

$$\cos(ka) \approx 1 - \frac{1}{2}(ka)^2 \quad (2.55)$$

to

$$\omega^2 = \frac{C}{M} (ka)^2 \quad (2.56)$$

which shows that for $ka \ll 1$ the frequency is directly proportional to the wave number, or in other words that the phase velocity is independent of frequency. In the continuum limit ($a \rightarrow 0$) the group velocity, which is defined as the derivative of the frequency ω with respect to the wave number k tends to ω/k , which is exactly as in the continuum theory. The grey underlaid area in Figure 2.21 corresponds to the occurring wave numbers in an aluminium film after excitation with an ultrashort laser pulse. Although this comparison is a strong simplification of the facts it shows that one can still work with the continuum theory even with the small wavelength in the order of 10-20nm.

2.4 Detection of the acoustic pulses

Recently a variety of different detection configurations have been presented. All these detection techniques have the same goal: probing the modulation of the dielectric constants by an incident ultrashort optical laser pulse. This mod-

ulation can be caused by several different reasons, for example by increased temperature and thermal diffusion or propagating acoustic pulses. It is important to probe these phenomena with a time resolution that is sufficiently high to cover the whole frequency range. The spatial resolution of this technique is limited by the Rayleigh criterion which describes the fact that optical pulses can in the best case only be focussed to half of the optical wavelength. In the case presented here the optical spot size is in the order of some microns when working with microscope objectives.

The simplest way to detect the reflectivity change caused by a modulation of the dielectric constants is to measure the intensity of the reflected probe pulse (see Thomsen C. et. al. [81]). To enhance the resolution, in order to measure very small changes of the reflectivity, one has the possibility to improve the optical part of the detection and the signal processing. One option is to reduce the spot size in order to increase the probe light intensity, which is however limited by the damage threshold of the surface material. Another possibility is to use interferometrical detection which measures the phase change. Different interferometrical detections were presented for example Sagnac interferometer (Nikoonahad M. et. al. [47], Hurley D.H. et al. [25]), Michelson interferometer (Richardson C.J.K. et. al. [63]) or Mach-Zehnder interferometer (Perrin B. et. al. [51]). It should be noted that working with interferometrical detection the detected reflectivity change is caused by the displacement of the top surface and the modulation of the dielectric constants. A further possibility for the detection is to measure the angular deflection of the incident probe pulse by the occurring displacement on the top surface (Wright O.B. et. al. [92]).

In the experimental setup presented here the detection is performed by measuring the reflectivity in a similar way as proposed by Thomsen C. et. al. [81]. Further enhancements are realized in the signal processing (see Chapter 3).

The overall reflectance or transmittance measured by one of the discussed configurations is affected by the following two mechanisms:

- Perturbations of the dielectric constants or the (complex) refractive index.
- Perturbations of the interface or surface positions implying variations of the film thicknesses.

For the following derivations it is assumed that the coherence length of the laser pulse is much larger than the film thickness. Since the coherence length of 100fs laser pulses is in the order of $\sim 30\mu\text{m}$, films thinner than $\sim 5\mu\text{m}$ satisfy this assumption (Matusda O. et. al. [40]). According to Figure 3.7 (right) the bandwidth of the laser pulse depends on the temporal shape and is usually in the order of $\pm \sim 10\text{-}15\text{nm}$ around the central wavelength in the order of 800nm. It is therefore assumed that the laser pulse is monochromatic and exists only of a single wavelength.

2.4.1 Perturbations of the dielectric constants (or refractive index)

The dielectric constants can be perturbed by
 - the induced temperature in the thin film and
 - the time varying strain in the thin film.

In the following two subsections both cases are discussed.

2.4.1.1 Perturbations of the dielectric constants by the mechanical strain

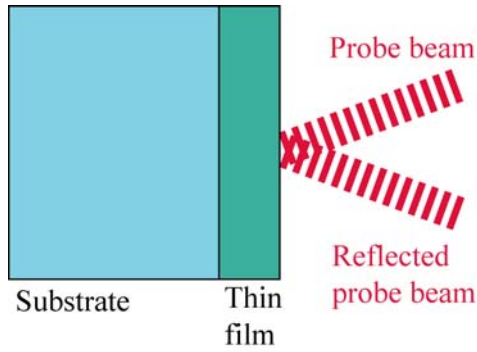


Figure 2.22 Detection configuration with opaque top layer

In order to isolate the reflectivity change caused by the mechanical strain only, the reflection r of the stationary system is subtracted from the measured optical reflection ($r + \Delta r$) according to Equation (2.57)

$$\Delta R = |r + \Delta r|^2 - |r|^2 \quad (2.57)$$

Δr denotes the modulation of the optical reflection by the induced mechanical strain. The dielectric constant ε in a material in the absence of any strain is

$$\varepsilon = (n_f + i\kappa_f)^2 \quad (2.58)$$

in which n_f and κ_f denotes the real and imaginary part of the optical refractive index. The perturbation of the dielectric constant $\Delta\varepsilon$ by the changes induced by the acoustic pulse (strain ε_z) is represented as (Thomsen C. et. al. [81])

$$\Delta\varepsilon = 2(n_f + i\kappa_f) \left(\frac{\partial n_f}{\partial \varepsilon_z} + i \cdot \frac{\partial \kappa_f}{\partial \varepsilon_z} \right) \varepsilon_z(z, t) \quad (2.59)$$

ε_z is the strain in z -direction and depends on the thickness coordinate z and the time t . The derivatives $(\partial n_f)/(\partial \varepsilon_z)$ and $(\partial \kappa_f)/(\partial \varepsilon_z)$ describe the photoelastic behavior. In most cases and in particular for metallic thin films, information about the dependence of the complex refractive index on strain is very rare. In addition, the photoelastic behavior depends on the probe laser light wavelength, which is illustrated for aluminium thin films by Devos A. et. al. [15]. There it is reported about three measurements on aluminium thin film with probe light wavelength of 810nm, 850nm and 880nm. The measurements at 810nm and 880nm show reflectivity peaks, which have opposite signs. At a

wavelength of 850nm the reflectivity change is nearly negligible. The reason for this behavior is the dependency of the photoelastic response on the probe light wavelength. The strain pulse, which gives rise to the reflectivity peaks has always the same shape. As surmised by Thomsen C. et. al. [81] and shown by Devos A. et. al. [15] the photoelastic response is strong in spectral regions of singularities of interband transitions. Also, thermorefectance measurements have revealed the sensitivity to the interband transitions by showing a sudden inversion of the detected signal near 1.5eV (830nm) (Devos A. et. al. [15]). Examples of the thermomodulation spectra of aluminium, gold and copper are given by Rosei R. et. al. [66] - a discussion of the dependency of the photoelastic response to strain, which is also called piezo-optic behavior is discussed by Jiles D. C. et. al. [27]. In the Appendix C the connection of the derivatives $(\partial n_f)/(\partial \varepsilon_z)$ and $(\partial \kappa_f)/(\partial \varepsilon_z)$ with the photoelastic (piezo optical) constants P_{kl} is presented.

Similar to Thomsen C. et. al. [81] we can find a change Δr in the reflection coefficient r caused by the perturbation $\Delta \varepsilon$ of the dielectric constant of

$$\Delta r = \frac{ik_v^2}{2k_f} \cdot t_{vf} \cdot t_{fv} \cdot \int_0^{\infty} e^{2ik_f z'} \Delta \varepsilon(z', t) dz' \quad (2.60)$$

k_v and k_f are the wave numbers in vacuum and the film and t_{vf} is the optical transmission coefficient (amplitude) from the vacuum into the film and t_{fv} vice versa (see Hecht E. [22]). It is assumed that the wave numbers in vacuum and air are the same. Together with Equation (2.59) Equation (2.60) yields

$$\Delta r = \frac{ik_v^2}{k_f} \cdot t_{vf} \cdot t_{fv} \cdot (n_f + ik_f) \cdot \int_0^{\infty} e^{2ik_f z'} \left(\frac{\partial n_f}{\partial \varepsilon_z} + i \cdot \frac{\partial \kappa_f}{\partial \varepsilon_z} \right) \Delta \varepsilon_z(z', t) dz' \quad (2.61)$$

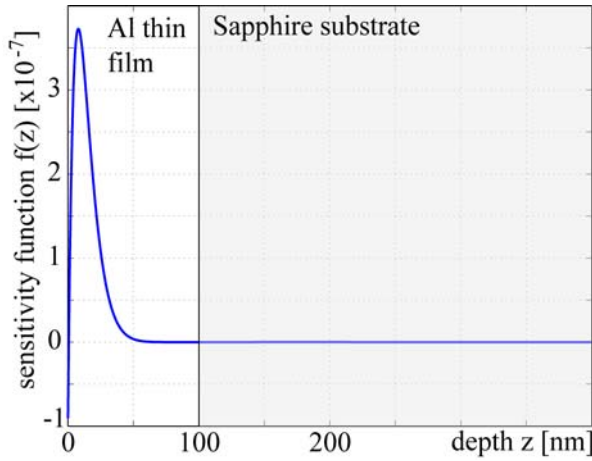


Figure 2.23 Sensitivity function $f(z)$ of an aluminium film (calculated with properties given in Appendix A)

This result can be combined with equation (2.57), which leads to the reflectivity change ΔR

$$\Delta R(t) = \int_0^{\infty} f(z') \varepsilon_z(z', t) dz' \quad (2.62)$$

$f(z)$ is the so called sensitivity function, which determines how strain in different depths contributes to the reflectivity change measured on the top surface (Thomsen C. et. al. [81]). The sensitivity function $f(z)$ depends on the complex optical refractive index, the probe pulse optical

wavelength, and on the photoelastic behavior of the film material. In general, the sensitivity function has an overall exponential decaying tendency ($e^{-(z/\xi)}$) and shows that strain at positions z below the 2 or 3 times the absorption length ξ has a negligible contribution to the reflectivity change

2.4.1.2 Perturbations of the reflectivity caused by the induced temperature

Apart from the strain distribution, the induced temperature modulates the dielectric constants also. Similar calculations as shown in the previous Chapter 2.4.1.1 can be performed with the temperature instead of the strain distribution. The general idea is shown in the appendix of the paper presented by Matsuda O. et. al. [40] and in the report of Miklos A. et. al. [43]. Usually this problem can be solved with reasonable accuracy by calculating the reflectivity change with

$$\Delta R = a \Delta T_e + b \Delta T_l \quad (2.63)$$

where a and b are constant coefficients describing how electron and lattice heating (ΔT_e and ΔT_l) affect the reflectivity.

2.4.1.3 Complete simulation of the experiment on a single opaque thin film

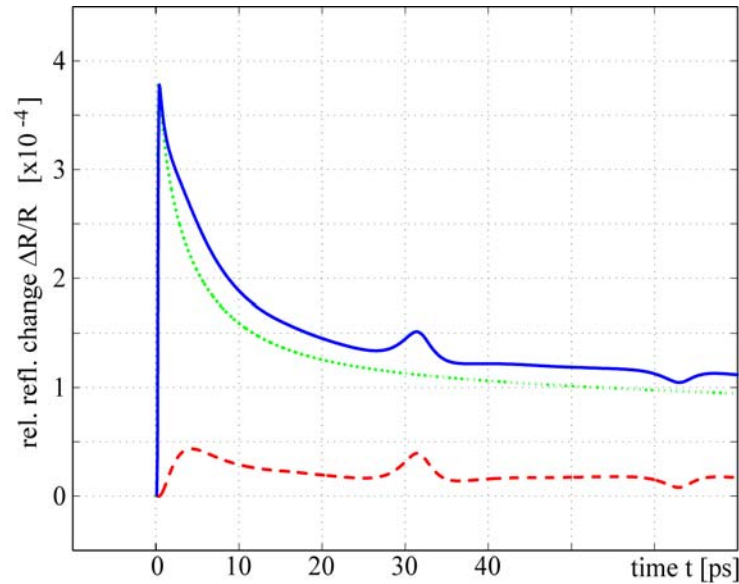


Figure 2.24 Calculated reflectivity change in a 100nm aluminium film on a sapphire substrate (solid line - overall reflectivity change, dashed line - contribution caused by strain, dotted - contribution caused by induced temperature)

Figure 2.24 shows the simulated reflectivity change measured on the surface of an aluminium film. Time varying induced temperature and strain are calculated numerically with the previously discussed two-temperature model and subsequently by solving the wave equation. All material properties, optical constants and laser parameters, are as usual, except the pump pulse laser fluence of 1.225J/m^2 , which corresponds to an average laser power of 200mW. Both contributions to the reflectivity change, namely the photoelastic, as well as the contribution caused by the induced temperature, are presented. The unknown constants (photoelastic behavior $(\partial n_f)/(\partial \varepsilon_z)$ and $(\partial \kappa_f)/(\partial \varepsilon_z)$, a and b which are constant coefficients describing reflectivity change on the heating) determining the amplitude of both contributions are chosen in a way that the results are similar to measurements on aluminium films. An estimation of these constants is possible by fitting simulations and measurements.

2.4.2 Perturbations of the refractive index in transparent thin films and of the interface positions

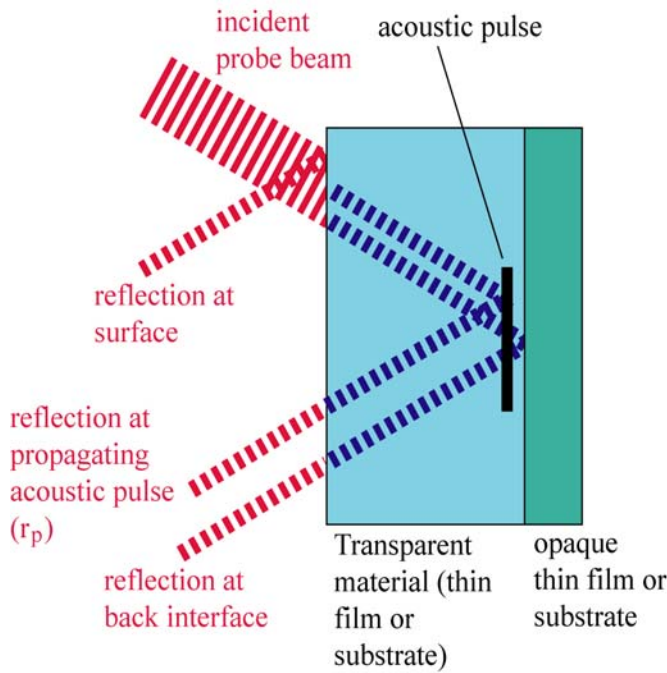


Figure 2.25 Reflections of the incident probe laser pulse in a transparent configuration

probe laser pulses, can be observed. According to Figure 2.25 the incident probe laser pulse is partly reflected at the surface. The transmitted part is partly reflected at the propagating acoustic pulse. The remaining part of the probe laser pulse is finally reflected at the back surface or interface. These three parts of the probe light pulse interfere, constructively and destructively depending on the geometrical dimensions and on the propagating acoustic pulse, which leads to oscillations in the reflectivity (also shown in Figure 4.24). Since the laser pulse reflection at the propagating pulse r_p depends, according to (2.64) [34]

$$r_p = ik_v \int_0^{\infty} e^{-2ik_{tr}z} \frac{\partial n_{tr}}{\partial \varepsilon_z} \varepsilon_z(z, t) dz \quad (2.64)$$

on the derivative $(\partial n_{tr})/(\partial \varepsilon_z)$, the photoelastic behavior of the transparent material has a strong influence on the amplitude of the oscillating interferences. k_v and k_{tr} are the wave numbers in vacuum and the transparent material and n_{tr} denotes the optical refractive index. If further reflections of the laser

A further interesting configuration is the case of a transparent top layer. In this case, three contributions to the reflectivity change are to be distinguished (Matsuda O. et. al. [40], Wright O.B. [89], Gusev V. [20]).

- The oscillations of the reflectivity change caused by interferences of various reflections
- The photoelastic response of the underlying opaque thin film or substrate
- The perturbations of the interface positions

Oscillations, which are caused by interferences of the reflected parts of the

pulse on the propagating acoustic pulse are taken into account (second reflection for instance) the accuracy of the describing theory is increasing (Wright O.B. [89]). A solution of the reflectivity change in a transparent substrate coated with an opaque thin film is derived by Lin H.-N. et. al. [34] - for a transparent thin film on an opaque thin film or substrate, respectively by Matsuda O. et. al. [40], Wright O.B. [89] and Gusev V. [20]. Measurements of such oscillations are presented in Chapter 4.2.

The photoelastic effect of the strain distribution in the underlying opaque substrate or thin film is the second contribution to the overall measured signal. The principal theory has been described previously (Chapter 2.4.1).

Aside from the photoelastic contribution, the third effect, which is less known, contributes also to the overall reflectivity change. This effect is independent of the coupling of the strain to the refractive index but the optical reflectance is affected by the motion, of the specimens interfaces or surfaces, respectively (Matsuda O. et. al. [40], Wright O.B. [89], Gusev V. [20], Perrin B. et. al. [51]). The varying interferences of the optical probe light reflections at the interfaces or surfaces which are moving cause the change in the probe light reflectivity.

Chapter 3

Experimental setup

To perform dynamic measurements, such as the measurement of the bulk wave propagation in very thin films or microstructures with dimensions varying from tens of nanometers to several microns, it is necessary to have a technique with temporal resolution of femtoseconds or at least picoseconds (Table 3.1). This can easily be understood if one takes into account that the bulk wave speed of most materials is in the order of 3000m/s to 11000m/s. With the pump-probe technique - which will be explained in this chapter - it is possible to perform measurements with a temporal resolution of several femtoseconds. The resolution in the time domain is only limited by the laser pulse duration, which at the moment is in the order of 10fs for commercially available ultrashort pulse laser systems.

<i>Dynamic measurements in</i>	<i>Frequencies</i>	<i>Temporal resolution</i>
mm range	kHz - MHz	μ s
μ m range	MHz - GHz	ns
nm range	GHz - THz	ps

Table 3.1 Dependency of the necessary temporal resolution on the geometrical dimensions

This technique is also applied in solid-state physics in order to analyze structural properties and electronics for observation of fast rise times. In addition it is used in non-linear optics, and in chemistry, enabling a time resolved observation of very fast processes and phenomena such as chemical reactions.

3.1 Setup

Figure 3.1 shows the schematic experimental setup. The essential parts of this technique are two optical paths (pump and probe) with variable lengths which are used to precisely control the time shift between two synchronously emitted short laser pulses. Usually the setup is built in a way that laser pulses of a common source are split into pump and probe pulses and the different optical path lengths are realized with a moving translation table. Another possibility would be two exactly synchronized ultrashort pulse lasers. The pump laser pulse is used for excitation, the probe pulse for measuring the experimental response. This technique leads to a temporal resolution which is only limited by the laser pulse duration, thus, phenomena occurring beyond bandwidth and rise time of currently available equipment become accessible.

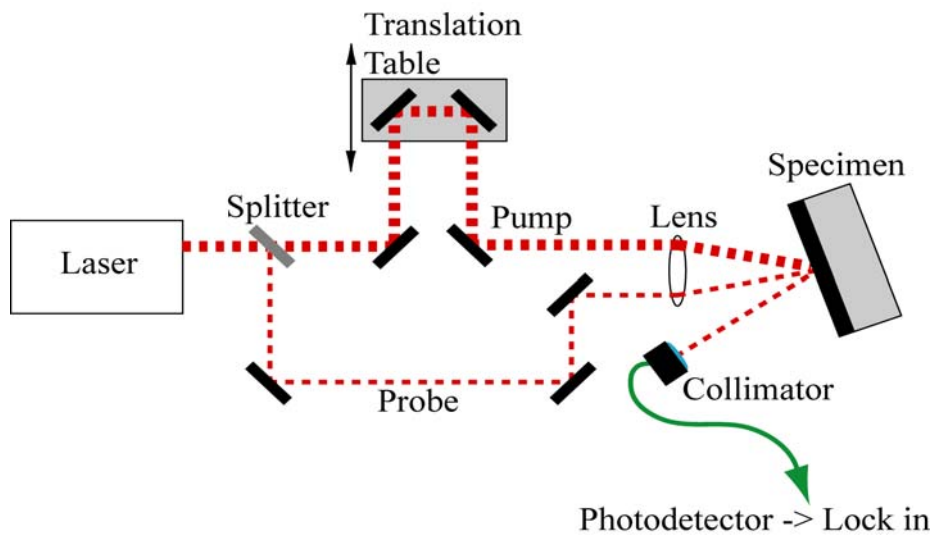


Figure 3.1 Schematic experimental setup

A detailed scheme of the experimental setup with all optical components is presented in Figure 3.2. A titanium sapphire laser emits short laser pulses having durations of less than 70fs and a wavelength of 780nm to 830nm at a repetition rate of 81MHz. This laser system is described in detail in Chapter 3.2.1. The wavelength in the order of 800nm is chosen because light of this particular frequency is well absorbed by aluminium leading to a strong thermo-elastic interaction which results in relatively high acoustic amplitudes, which can be easily detected.

Following the laser pulses from the left to the right hand side (Figure 3.1), the beam is split into a pump beam carrying 90% of the energy and a weaker probe beam by a partly transmitting mirror (beam splitter).

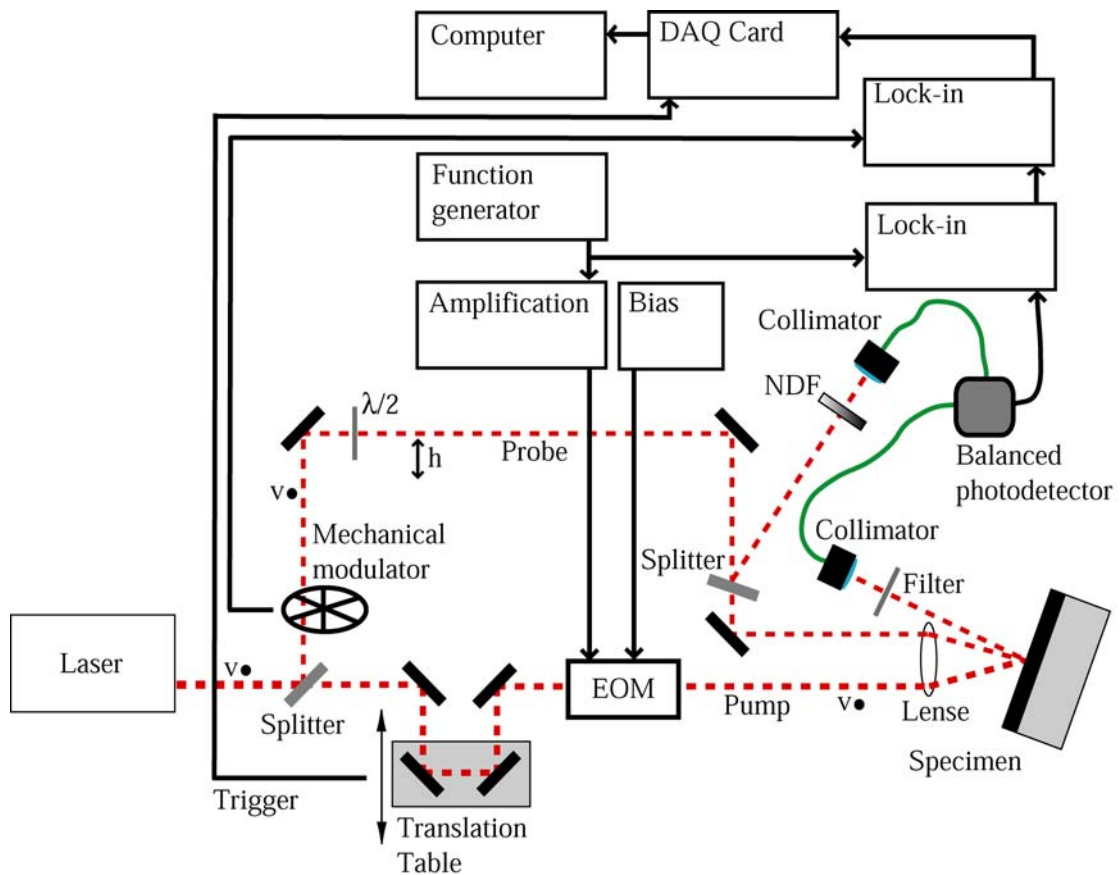


Figure 3.2 Detailed experimental setup (NDF - neutral density filter)

The pump pulses are absorbed within a thin surface layer depending on the measurement configuration and the material characteristics. The pump pulses induce a temperature increase. Mechanical pulses are excited, caused by the increased temperature and propagate perpendicular to the surface into the material. At every impedance mismatch the acoustic pulses are partly reflected according to the acoustic reflection coefficient. The acoustic pulses and the increased temperature change the optical reflectivity (Chapter 2.4) at the surface of the material which is measured with the probe laser pulse and a photo diode. The frequencies of the acoustic pulses, and consequently of the optical reflectivity change, are depending on the thickness of the absorbing surface layer but are usually in the order of 100GHz or higher. To measure with picosecond time resolution, which is necessary for experiments with frequency content of hundreds of GHz, the optical path of the pump laser pulse is varied while the path length of the probe pulse remains constant. Thereby the relative time between measurement and excitation is changed. The whole experiment is constantly repeated with a repetition rate of the laser (81MHz). Figure 3.3 illustrates how the optical reflectivity is scanned by varying the relative time

shift of pump and probe laser pulses. The presented measurement is done with a specimen of an approximately 100nm aluminium film on a sapphire substrate. Before the pump laser pulse hits the specimen the probe laser pulse measures no relative change in the optical reflectivity. When the path length of pump and probe laser pulses is exactly the same, both laser pulses hit the specimen at the same time and an initial reflectivity jump is observed. This reflectivity jump is caused by the increased temperature and strain.

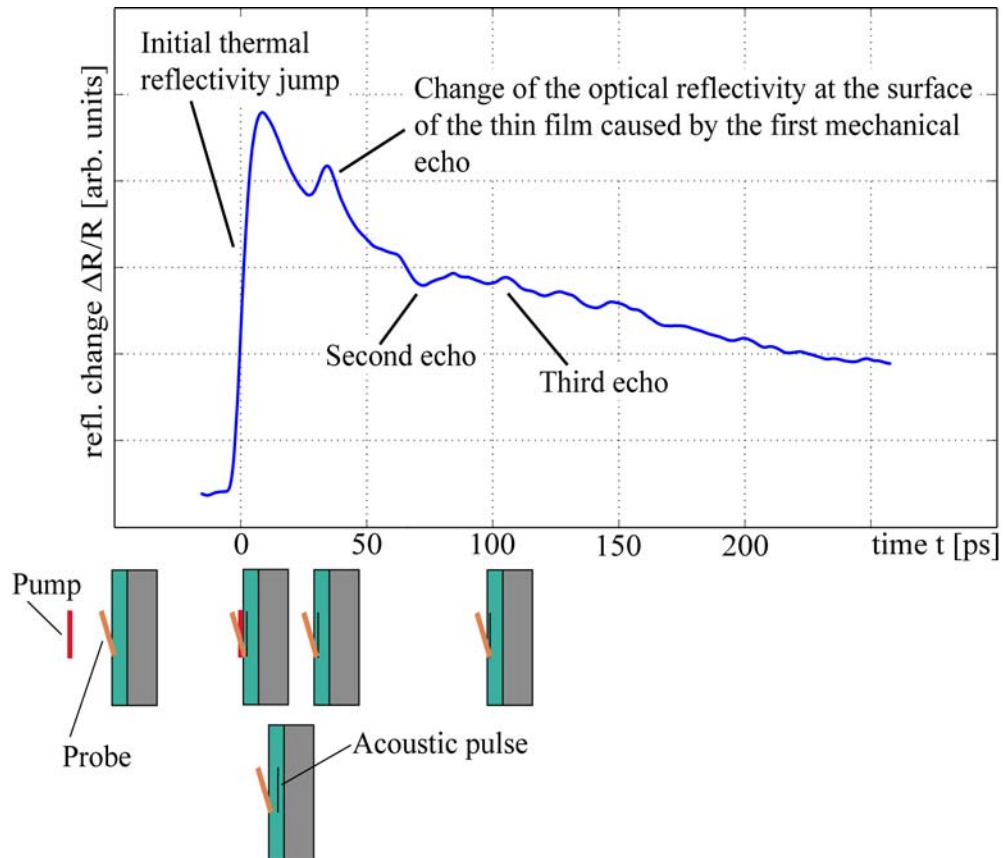


Figure 3.3 Measurement of a 100nm aluminium film on a sapphire substrate

Superimposed on the smooth decay of the reflectivity, which is caused by the slowly decreasing temperature in the thin film, are acoustic echo induced peaks in the reflectivity. These peaks are caused by photoelastic effects and appear when the acoustic pulses reach the surface where the reflectivity is measured. The sign of the reflectivity peaks depends on the acoustic configuration of the specimen. In this example, the first reflection is measured after 36ps, the second after 72ps and the third is observed after approximately 108ps.

Since the optical reflectivity change is usually very small the goal of the experimental setup is to increase the signal to noise ratio in a way that the thermo-acoustic information can be measured. Various concepts, which are

described in the following, are used for an enhancement of the signal to noise ratio.

The pump laser beam is modulated harmonically with a frequency of 19MHz with an electro-optical modulator. The probe laser beam is modulated with very low frequency in the order of 400Hz using a mechanical modulator (chopper). Both modulation frequencies are used for lock-in amplification as described in Chapter 3.3. The exciting laser beam and also the optical path of the pump beam have vertical polarization, however, the optical path of the probe laser pulses has horizontal polarization behind the half-wave-plate. The cross polarization (pump and probe pulse propagates with different polarization planes) of pump and probe laser pulses is used to achieve a higher signal to noise ratio. A polarization filter mounted in front of the main collimator suppresses disturbing influences of scattered light from the pump laser pulses. The reflected probe laser pulses are filtered by the polarizer and collected with a collimator. A single mode fiber transmits the light to the balanced photodetector. The second fiber connected to the balanced photodetector collects the light of the reference probe laser beam, which is not affected by the reflectivity change at the surface of the specimen. The intensities of these two probe pulses are carefully equalized by a variable neutral density filter (NDF) and a variable time adjustment line (controller: Newport MM4005, stage: Newport MTM250PP1), before the experiment is started. During the experiment the difference of its intensities is amplified by the photodetector. Advantages of this configuration are the following: The measured and amplified signal of the photodetector is caused by the reflectivity change only and also lower frequency fluctuations of the laser (caused by the laser unit for instance) are strongly reduced, thus, the noise is reduced.

A biconvex lens focusses the pump and probe beam on the surface of the specimen. The lens is split with each part mounted on an individual x-y-z-stage, allowing the position and the focal plane of each laser beam to be adjusted. Also, the specimen itself is mounted on a motorized x-y-stage (controller: Newport MM4005, stages: Newport MTM200PP.1) which allows scanning of a large area. The motorized stage is controlled by a LabViewTM program via GPIB port of the computer. In addition, the specimen holder has several other features, such as fibers and photodiodes for initial adjustments when setting up new experiments. The x-y-stage is twisted about 17 degrees to avoid disturbances caused by reflected light, which is following the pump and probe path back to the laser.

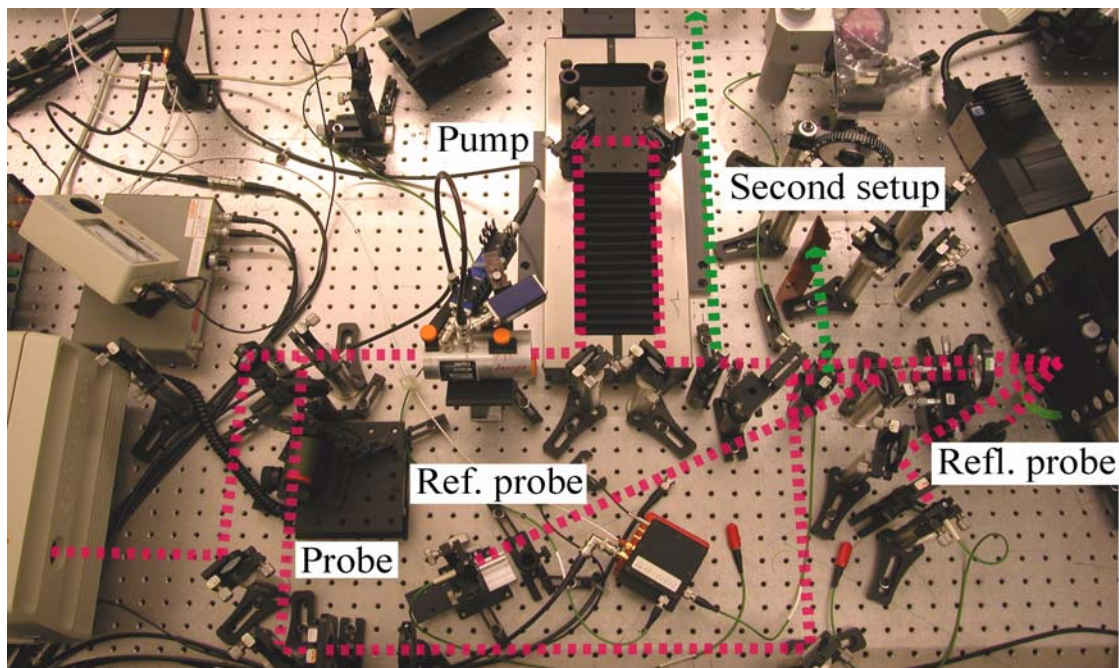


Figure 3.4 Experimental setup with laser beam path (dashed lines)

3.2 Most important components of the experimental setup

3.2.1 Ultrashort pulse laser

The laser system consists (see Figure 3.5, Figure 3.6) of a diode pumped Spectra Physics MillenniaTM V (5W) continuous wave laser with a wavelength in the order of 532nm and a Spectra Physics TsunamiTM ultrashort pulse laser.

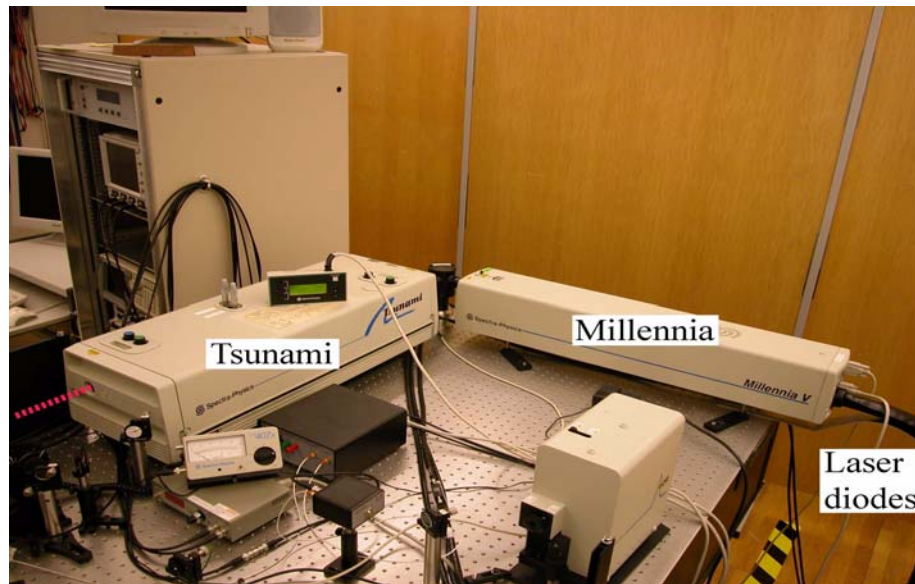


Figure 3.5 Laser System

The MillenniaTM V houses the optical resonator, the neodymium yttrium vanadate (Nd:YVO₄) gain medium, diode laser fiber delivery, telescope focusing system, a lithium triborate (LBO) doubling crystal and the output beam telescope system. The highly efficient, diode pumped Nd:YVO₄ laser crystal requires far less cooling water than a plasma tube of comparable output power. According to Spectra PhysicsTM [72] this virtually eliminates low-frequency optical noise, which is a major problem for water-cooled ion lasers. The output laser beam of the MillenniaTM V pumps the ultrashort pulse titanium sapphire laser with approximately 5W.

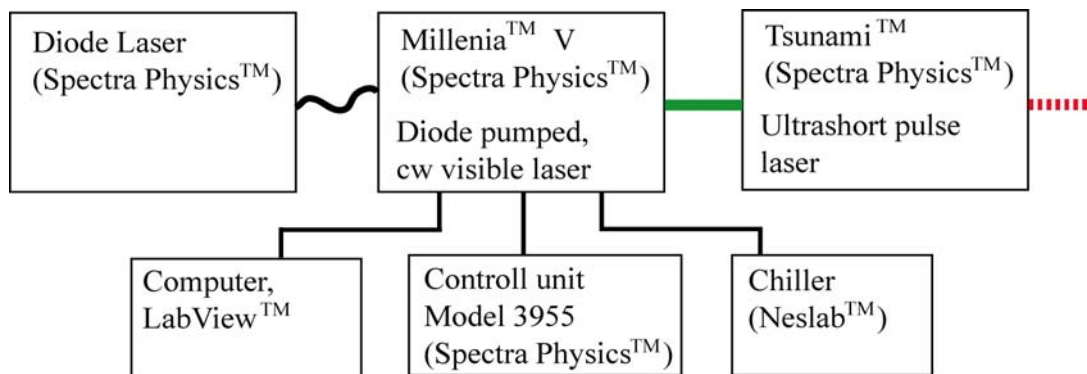


Figure 3.6 Scheme of the laser system

The titanium sapphire laser (Spectra PhysicsTM TsunamiTM) emits pulses with duration (FWMH, full width at medium height) shorter than 80fs. As shown in Figure 3.7 (left) the temporal shape of a 85fs and a 110fs (FWMH) laser pulse which is measured with the Spectra Physics Autocorrelator (Model 409) is nearly gaussian.

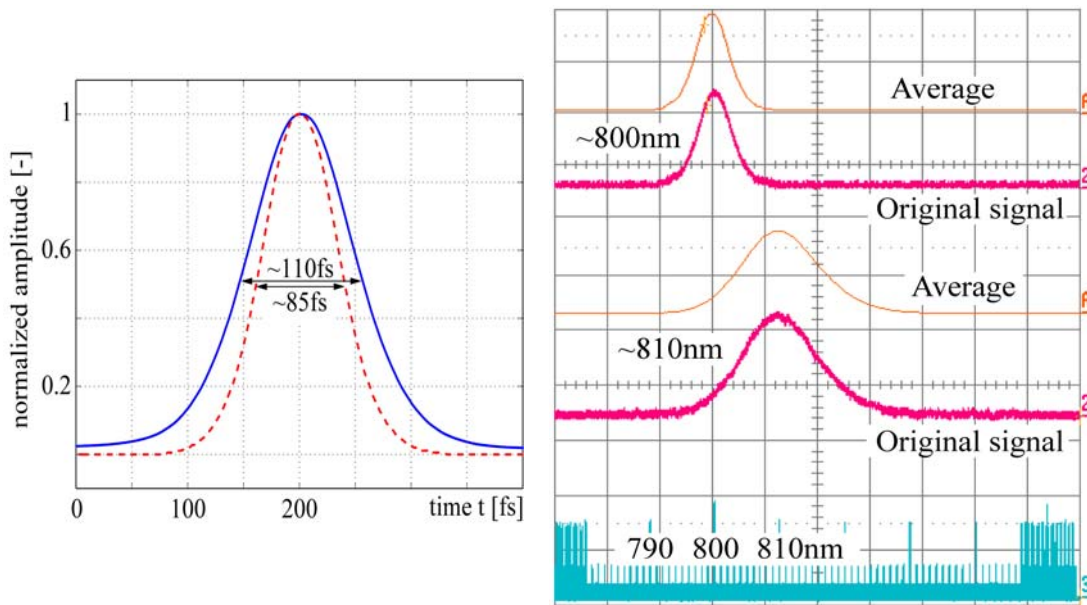


Figure 3.7 Left: temporal shape of a 85fs and 110fs ultrashort laser pulse; right: wavelength content of two different laser pulses with central wavelength at 800nm and 810nm

With the prism dispersion compensation control and the wavelength control of the TsunamiTM, the laser pulse duration as well as the wavelength range can be adjusted. The chosen standard mirror-set of the TsunamiTM limits the wavelength range from approximately 720nm to 850nm [73]. Experience has shown that usually further alignment is necessary working outside a smaller spectral content of 780nm to 830nm. In general, laser alignment has always a slight effect on the beam path in the laser and setup. Additionally, the wavelength content of a laser pulse depends on the laser pulse duration, which is shown on two examples measured with the laser spectrometer (Figure 3.7 (right)). The maximum average output power of the ultrashort pulse laser is in the order of 1W. With a laser pulse repetition rate of 81MHz the resulting pulse energy amounts to 12.3nJ. Nevertheless this small pulse energy leads with an average pulse duration of 100fs to a peak power higher than 120kW.

3.2.2 Electro-optical modulator

The Conoptics electro-optical modulator (Conoptics 350-50) is used for the modulation of the pump laser beam in the higher frequency range.

The electro-optical modulator has two different inputs, one for the bias connection (DC voltage) and another for the high frequency modulation signal (RF). The high frequency modulation signal is in the order of 19MHz. The EOM is made of a KD*P crystal, which changes the polarization of the laser light depending on the input voltage.

Outgoing laser pulses are filtered with a polar filter behind the crystal. Both the high frequency modulation signal (RF) and the bias voltage are connected to the crystal which yields a voltage on the crystal according to Figure 3.9.

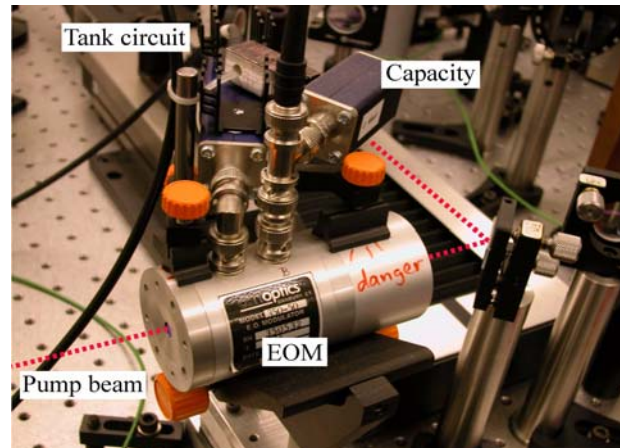


Figure 3.8 EOM (Conoptics 350-50) with tank circuit and capacity

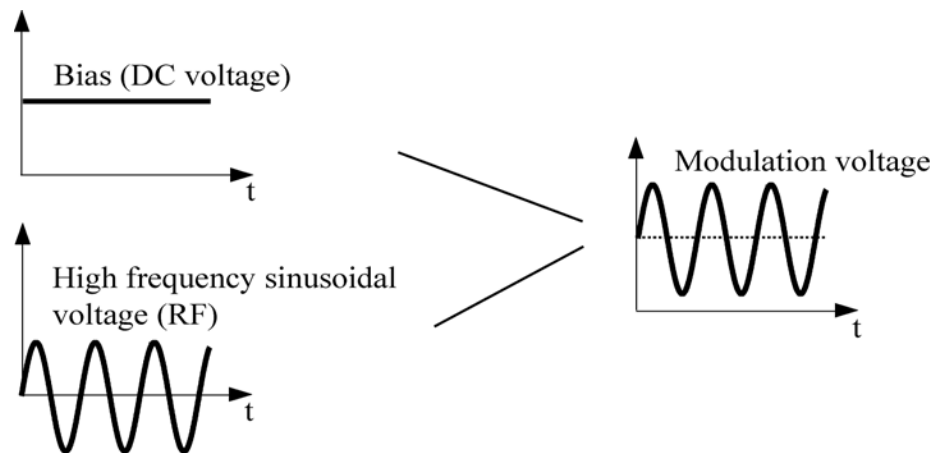


Figure 3.9 High frequency modulation signal

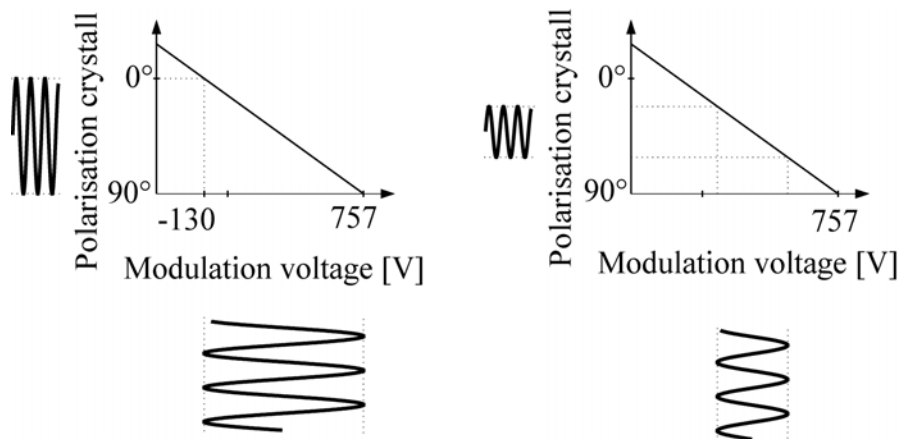


Figure 3.10 Connection between polarization change and the electrical high frequency signal (out of Bryner J.[5])

The highest modulation depth is reached when the polarization change of the crystal oscillates between 0° and 90° . The electrical modulation signal must be conditioned in a way that it is oscillating between the voltages corresponding to 0° and 90° polarization change, respectively. In Figure 3.10 the schematic working of the EOM is shown. The manufacturer gives a voltage of 757V for changing the polarization of 90° . So, if we have vertically polarized light coming into the EOM the polarization is changed by about 90° through the feed voltage of 757V and therefore, the outgoing light has horizontal polarization. Since the polarization filter at the optical output of the EOM lets only the vertically polarized part of the laser light pass, the EOM blocks the total incoming light at voltage of 757V.

The high-frequency modulation signal is excited by an electronic function generator (Stanford Research Systems (SRS) DS345) and amplified by a high-frequency amplifier (ENI 325LA RF Amplifier) as shown in Figure 3.11.

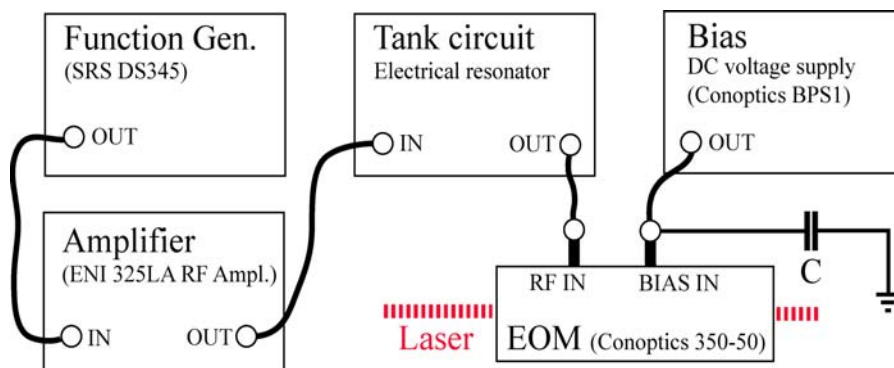


Figure 3.11 Electrical scheme of EOM

An electrical resonator amplifies the voltage again before it is connected to the high-frequency input of the EOM. The electrical resonator is built according to Figure 3.12. The capacity $C1$ is 300pF, the coil $L1$ has 1.6 μ H and the capacity $C2$ is variable between 0.8pF and 12pF, which leads to a resonance frequency between 18.97MHz and 21.97MHz, depending on the capacity $C2$.

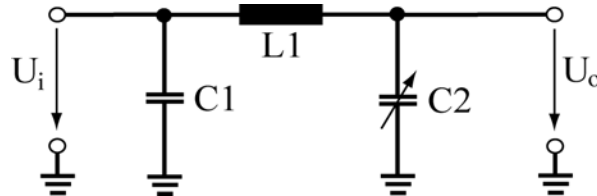


Figure 3.12 Tank circuit (electrical resonator)

In Appendix D the calculation of the resonance frequency of the tank circuit is explained. A resonance frequency of 19MHz is chosen because the laser noise decreases with increasing frequency except at fractions of the repetition frequency. The high capacity C in Figure 3.11 is very important to keep the resonance frequency at the chosen value, because the capacity C connects every high frequency signal to ground. If the capacity C is missing the high frequency signal is also connected to the bias DC-power supply, which strongly affects the resonance frequency of the tank circuit.

3.2.3 Mechanical modulator

The mechanical modulator (Figure 3.13), also called chopper (Stanford Research Systems (SRS) SR540), modulates the probe laser beam with a box car signal. The modulation frequency lies between 10Hz and 3kHz.

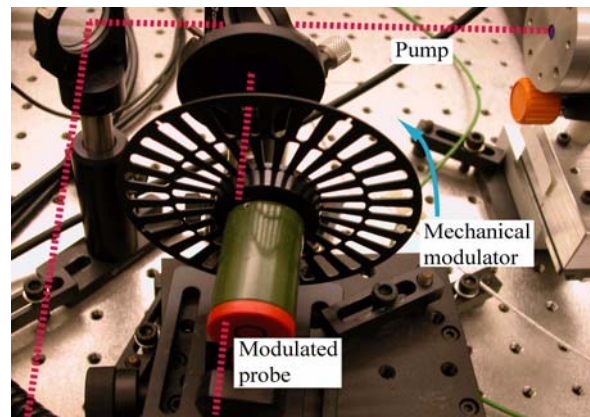


Figure 3.13 Mechanical modulator

3.2.4 Balanced photodetector

The balanced photodetector (New Focus Model 1607-AC, Figure 3.14) amplifies the difference of the incident laser beams. Optical fibers connect the reflected probe and the reference probe laser beam to the photodetector. High frequency electrical output is directly connected to the first lock-in amplifier.

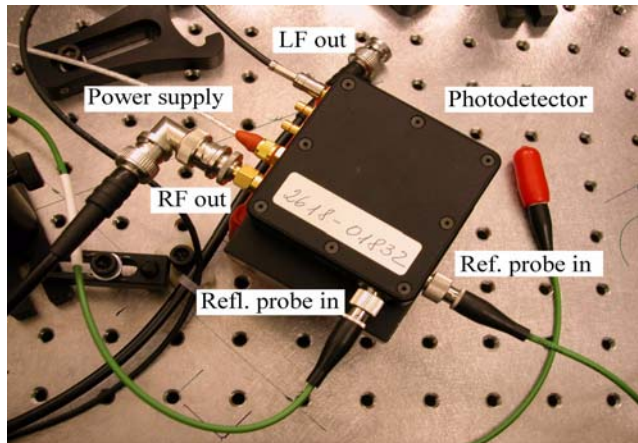


Figure 3.14 Balanced photodetector (New Focus Model 1607-AC)

The photodetector is designed for a wavelength range from 320nm and 1000nm with highest sensitivity at about 780nm. The bandwidth of the RF output is 40kHz - 650MHz.

3.2.5 Lock-In amplifiers

With lock-in amplifiers it is possible to measure very small signals even if the noise is orders of magnitudes higher than the signal of interest. The principle working of a lock-in amplifier is explained with the following example. In the lock-in amplifier the signal of interest with a frequency f_s is pre-amplified and then multiplied by the reference signal (frequency f_r). The multiplication leads to two signals, one at the difference frequency ($f_s - f_r$) and the other at the sum frequency ($f_s + f_r$) which is removed by low pass filtering. Since the reference signal has usually exactly the same frequency as the signal of interest the difference frequency component is a DC signal. The amplitude of this DC signal corresponds to the amplitude of the signal with frequency f_s . The DC signal is superimposed by higher frequency signal components which depend on the characteristics of the low pass filter (time constant of the filter (bandwidth), filter-order (filter roll-off)). The bandwidth of lock-in amplifiers (low pass filter) can be chosen very small in the order of mHz and therefore the noise is strongly reduced which allows the measurement of very small signals (frequency f_s). A small bandwidth (\sim mHz) corresponds to a high time constant (\sim s) of the low pass filter and high filter order.

In our case the reference frequency has exactly the same frequency as the amplitude modulation of the laser beams. The chosen modulation frequencies, bandwidth and signal processing is discussed in Chapter 3.3.

In our setup two lock-in amplifiers are used - one high frequency lock-in

amplifier (Stanford Research Systems (SRS) SR844) and one for lower frequencies (Stanford Research Systems (SRS) SR850).

3.2.6 Computer-based signal processing with LabView™

The output signal of the lock-in amplifier is recorded with a data acquisition system (DAQ system PCI-MIO-16XE-10) of National Instruments™ connected with a common Windows™-PC. A LabView™ virtual instrument controls the movement of the delay table via GPIB port and records the measurement signal with the mentioned DAQ system. Each measurement and an average of all measurements is shown on the display. It is possible to move the specimen after a certain number of measurement for lateral scanning processes.

3.3 Signal processing

Direct time domain detection of transient reflectivity changes is the simplest technique but its use in our case is limited by two facts: First of all, every component in the setup must have a bandwidth in the order of the reflectivity changes, otherwise it is acting as a low pass filter and affects the measured signal shape. In the moment commercial available oscilloscopes and amplifiers have bandwidth slightly beyond 10GHz, which corresponds to a time resolution in the order of 100ps, hence, they are too slow for measuring the very fast reflectivity changes directly. Second, the high necessary bandwidth leads to a higher noise level (thermal noise, 1/f noise and shot noise) which limits the sensitivity of the setup.

These two reasons show quite clearly why the pump-probe technique and its signal processing is used. In Figure 3.15 the components of the signal processing after the optical reflectivity measurement at the surface of the specimen are presented. Some detailed specifications and the operation of the electro-optic modulator (EOM), the mechanical modulator and the balanced photodetector were explained in the previous chapter. The principle of the signal processing becomes clear when discussed in terms of frequency spectra and how they are modified by each component. In the presented frequency spectra the DC component as well as the higher frequency components are omitted because they are not needed in this investigation. Since the pump beam and the probe beam come from the same pulsed laser source, both beams have the same repetition frequency of 81MHz (Figure 3.15, (1)). The two beams are modulated, which means multiplied in the time domain with signals of two different frequencies. A harmonic signal of 19MHz (as generated for the EOM) is used for the modulation (Figure 3.15, (4)) of the pump beam (Figure 3.15, (5)). The probe

beam is multiplied with a rectangular signal of 400Hz (as generated by the mechanical chopper). Although a rectangular signal has a characteristic spectrum, it is represented as a narrow bar at its center frequency for simplicity reasons in the spectra shown in Figure 3.15 (2)

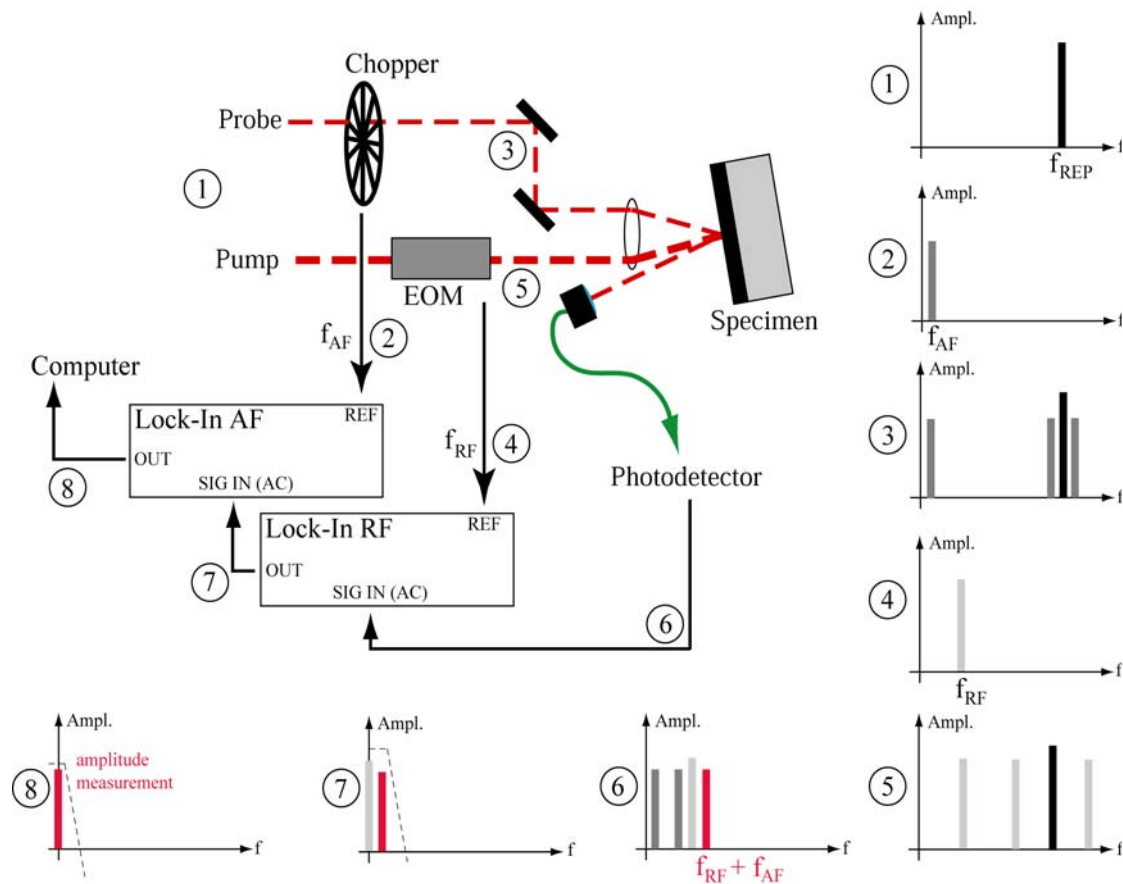


Figure 3.15 Signal processing

A multiplication in the time domain corresponds to a convolution or Faltung in the frequency domain. The measurement based on a photoacoustic effect, i.e. the changing optical reflectivity caused by the acoustic pulses, represents a multiplication in time domain as well, in which the modulated probe beam and the modulated pump beam are multiplied (Figure 3.15, (6)). The modulation of the short pulse laser beam leads to a spectrum which consists of the 19MHz and 81MHz peak and two characteristic side peaks at 62MHz and 100MHz (Figure 3.15, (5)). The situation for the modulated probe beam is similar (Figure 3.15, (3)). The multiplication in the time domain of the modulated pump beam and the modulated probe beam leads to the spectrum shown in Figure 3.15, (6). In this graph the higher frequency components are omitted because they are not needed in this investigation. The signal of interest which corresponds to the occurring reflectivity change is the amplitude of the most

right side peak having a frequency which amounts to the sum of the modulation frequency of the EOM (f_{RF} , 19MHz) and the frequency of the mechanical modulation (f_{AF} , ~400Hz). The signal with the sum frequency is chosen to avoid optical and electrical crosstalk and disturbances which have either the frequency of the driving voltage of the EOM or the frequency of the chopper. In the first lock-in amplifier the signal shown in Figure 3.15, (6) is multiplied with the reference signal (Figure 3.15, (4)) and low pass filtered. According to the explanations in Chapter 3.2.5 the 19MHz signal is shifted to DC. Provided that the bandwidth (illustrated by the dashed line in Figure 3.15, (7)) of the RF lock-in amplifier is broad enough, the amplitude of the 19MHz peak is measured while the signal still contains its side peak, which is shifted to 400Hz (Figure 3.15, (7)). The amplitude of this peak, which is proportional to the optical reflectivity change caused by the photoacoustic effects, is measured by a second lock-in amplifier (Figure 3.15, (8), bandwidth of the second lock-in amplifier illustrated by the dashed line). The pump modulation frequency is chosen as high as possible but well below the repetition rate. It is also important to avoid the situation that the modulation frequency equals or lies near a rational fraction of the repetition rate (81MHz). 19MHz was chosen after analyzing the laser noise spectrum and identifying a low noise interval therein. The frequency of the mechanical modulator is set to ~400Hz because the frequency is small enough to be in the bandwidth of the high frequency lock-in, working with the filter of highest order.

It is also possible, to work only with a modulation of the pump beam so that the spectrum of the measured reflectivity change (Figure 3.15, (6)) is equal to the frequency content of the pump laser beam after the EOM (Figure 3.15, (5)). But working only with the modulation of the pump laser beam has, apart from the slightly smaller sensitivity, also the disadvantage that the elimination of electrical crosstalk and disturbances, caused by the relative high amplitude of the driving voltage of the EOM, cannot always be ensured.

3.4 Discussion of quantitative aspects

Spot size

For discussing quantitative aspects of the measurements it is essential to know the absorbed energy fluence which is the ratio of the absorbed energy and the laser spot size on the surface. Although this sounds easy, an accurate determination of the spot size in the focal plane has its difficulties. The measurements of the intensity in vertical and horizontal direction in Figure 3.16 are performed with a 50 μ m fiber connected to a photodetector using the experimental setup according Figure 3.18.

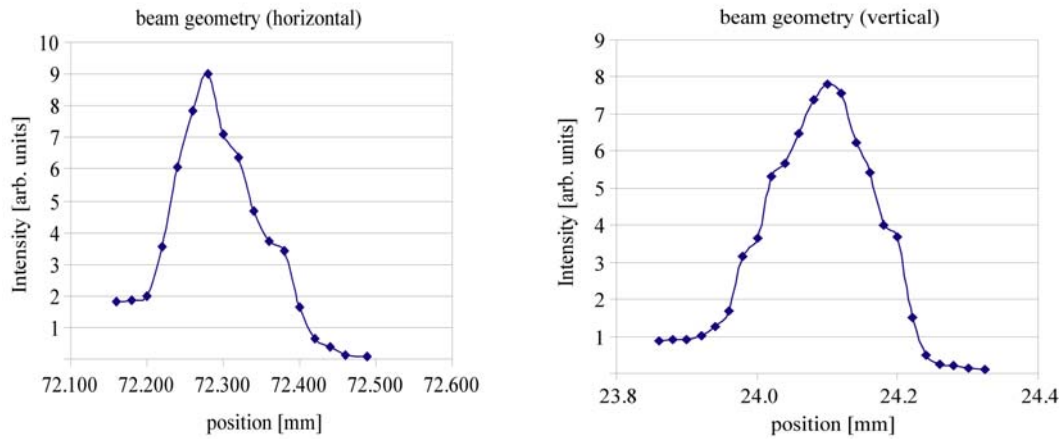


Figure 3.16 Horizontal and vertical beam geometry

Figure 3.16 shows a spot size diameter in horizontal and vertical direction in the order of $200\mu\text{m}$. Since the diameter of the fiber has almost the same order of magnitude as the spot size, the measured intensity is strongly affected by the fiber. Nevertheless the spot size can be estimated and has in the best case a diameter of about $100\mu\text{m}$.

Signal amplitude and noise

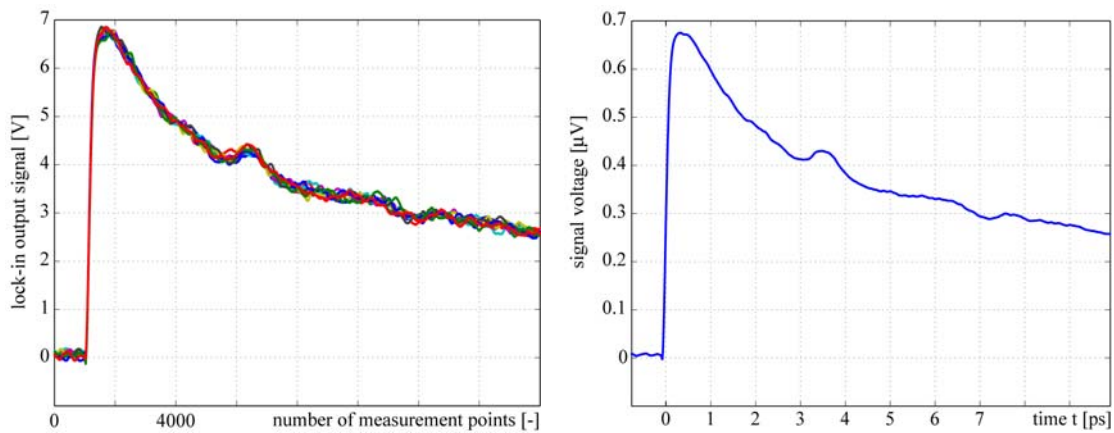


Figure 3.17 Picosecond ultrasound measurement of an approximately 100nm thick aluminium film; left: raw data of the 10 measurements; right: average of these 10 measurements on the left hand side

Figure 3.17 (left) shows the raw data of 10 measurements recorded with a time constant of the second lock-in of 100ms and a speed of the delay table of 0.5mm/s , which results according to Wright O.B. [89] in an estimated effective time constant below 1ps . The time constant of the first lock-in was set to $100\mu\text{s}$. Both lock-ins are using filters with a slope (filter roll-off) of 24dB/octave so that the -3dB cut-off frequency $f_{-3\text{dB}}$ is determined by

$$f_{-3dB} = \frac{0.435}{2\pi\tau} \quad (3.1)$$

in which τ denotes the time constant. Therefore, the cut-off frequency f_{-3dB} of the first lock-in is in the order of 700Hz and of the second one approximately 700mHz. The sensitivity of the first lock-in is usually 100 μ V and of the second 100mV from there the overall gain is 10^7 ($10^5 \times 10^2$), since both lock-ins have a maximum output voltage of 10V. In Figure 3.17 (left) the output voltage of the second lock-in of each measurement cycle is shown, however, in Figure 3.17 (right) the total gain is taken into account and the plotted signal is equivalent to the output of the photodetector, which is proportional to the reflectivity change.

With the second lock-in a noise level of 1.4mV/(Hz)^{1/2} was measured and yields with the appropriate bandwidth (781mHz) 1.23mV. Since the gain of the second lock-in is 10^2 the noise is almost two orders of magnitude smaller than the measured signal, which also appears from Figure 3.17 (left). A comparison of the single measurements in Figure 3.17 (left) and the average in Figure 3.17 (right) clearly shows that an expected further noise reduction is achieved by averaging several measurements.

Reflectivity change

The time varying signal in Figure 3.17 (right) is proportional to the transient reflectivity change, which occurs at the surface of the thin film. In general, the reflectivity R is the ratio of the power of the reflected beam P_{OUT} and incident beam P_{IN} so that $R = P_{OUT}/P_{IN}$. On the other hand, the change in the reflectivity ΔR is $\Delta R = \Delta P_{OUT}/P_{IN}$, which (similar to Richardson C.J.K. et. al. [64]) leads to

$$\frac{\Delta R}{R} = \frac{\Delta P_{OUT}}{P_{OUT}} = \frac{\Delta U_{OUT}}{U_{OUT}} \quad (3.2)$$

Since the signal magnitude ΔU_{OUT} , measured with the experimental setup, is proportional to the change in reflected power, a signal, which corresponds to the power of the reflected beam, is required for the estimation of $\Delta R/R$. The amplitude (U_{OUT}) of the reflected probe beam measured independently with a lock-in at the lower modulation frequency (Figure 3.15, f_{AF}) is equivalent to the reflected power P_{OUT} . In the previously discussed case the voltage U_{OUT} was 20mV, hence, the maximum relative reflectivity change $\Delta R/R$ in the measurement shown in Figure 3.17 (right) was about $3.4 \cdot 10^{-5}$. When measuring the voltage U_{OUT} one should make sure that the photodetector is not saturated.

3.5 Different measurement configurations

With the experimental setup it is possible to work with two different measurement configurations.

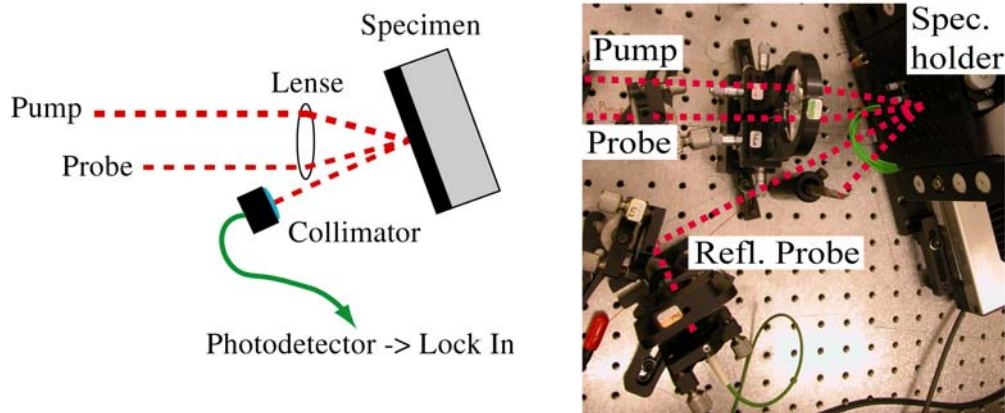


Figure 3.18 Left: specimen accessed from one side, scheme; right: experimental setup

In the first configuration shown in Figure 3.18 the specimen is accessed from one side thus the excitation and the measurement is realized from the same side. The pump laser beam is focussed with a split biconvex lens towards the specimen under an angle of 23.4° with respect to the specimen surface. The incidence angle of the probe laser beam is 11.4° . All reflected probe light is collected by a collimator, which is connected to one channel of the balanced photodetector by a single mode fiber. The spot size in this configuration is in the order of $100\mu\text{m}$ (Figure 3.16).

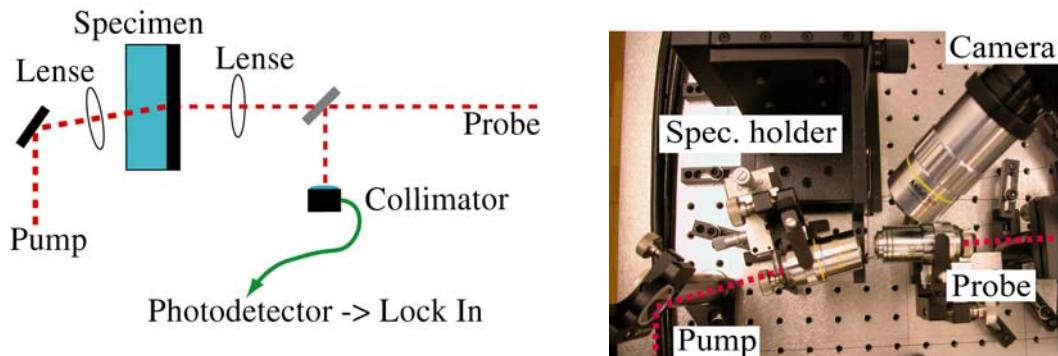


Figure 3.19 Left: measurement configuration for transparent substrates and microstructures; right: corresponding experimental setup

The second measurement configuration is realized for freestanding structures, such as membranes or cantilevers and thin films on transparent substrates. Two microscope objectives focus pump and probe laser beam towards the specimen according to Figure 3.19. The incidence angle of the pump laser beam is in the order of 10° , and the probe laser beam has perpendicular inci-

dence. Both microscope objectives allow to focus the laser beams to a very small spot size, which is necessary while working with microstructures. The spot diameter is estimated to be in the order of $5\mu\text{m}$.

Chapter 4

Results

The described measurement technique is applied to thin films, multilayer stacks and microstructures, such as membranes and cantilevers for the characterization of their mechanical properties or geometrical dimensions. Therefore, the first chapter is dedicated to the measurements and simulations on thin films and multilayer stacks on a substrate followed by a discussion of measurements in transparent media. The characterization of microstructured silicon nitride membranes shows that this technique can also be applied on micro- and even nanostructures. Finally, measurements on silicon cantilevers and truncated silicon tips are presented at the end of this chapter.

In this chapter the term 'acoustic reflectivity change' stands for the reflectivity change only caused by the propagating strain pulse. In these cases the reflectivity change, which corresponds to the induced temperature is subtracted.

4.1 Measurements on thin films

Mechanical characterization of thin film on substrates is one of the main applications of this measurement technique and is often used in the semiconductor industry. Semiconductor industry is one of the driving forces for further developments and places great demand on research because with changing materials some key parameters for the successful application, such as the photoacoustic properties, are also widely varying.

This first subsection deals with measurements and corresponding simulations on various thin films and multilayer stacks. The measurements on single thin films (aluminium or platinum thin films) show the influence of material properties such as the linear expansion coefficient or the photoelastic behavior on

the measurements. Also the application of picosecond ultrasound for the determination of film thicknesses or material properties on several points on a wafers is demonstrated and the dependency of the bulk wave velocity of aluminium on the film thickness is discussed. A discussion of the influence of the measurement configuration and the boundary conditions is presented in the next subsection. Two new fields of the application of picosecond ultrasound and the corresponding simulations are presented in the last two subsection. First the characterization of functionally graded materials (materials with smooth variations of the material properties) is shown on the example of a Al/Au/Al multilayer with smooth material transitions. Second, the limitations and accuracy of the thickness determination of diffusion barriers, especially of Ta and Ta/TaN barriers below a copper top layer, are discussed, using accurate simulations and measurements.

4.1.1 Aluminium thin films

Since the experimental setup used is optimized for aluminium thin films, first some measurements on aluminium thin films are discussed.

4.1.1.1 Specimens

All aluminium thin films presented in this investigation with thicknesses smaller than 100nm are manufactured with the Edwards E306 deposition system (Figure 4.1). The aluminium thin films were deposited at room temperature. The temperature rise during the electron beam evaporation of the aluminium can be neglected. The substrates are usually randomly oriented sapphire wafers or glass wafers of 2" diameter. All key parameters are presented in Table 4.1.

Pressure chamber	$1.5 \cdot 10^{-2}$ mTorr
Current e-beam	80mA
Deposition rate	$\sim 5 \text{ \AA/s}$

Table 4.1 Parameters of the electron beam evaporation deposition

All other films are deposited with a deposition system of Leybold Balzers under approximately the same conditions. The sputter deposition of the aluminium films is done with a magnetron sputter device with the following parameters (Table 4.2)

Pressure	5 mTorr
Power	400W
Deposition rate	$\sim 5\text{\AA}/\text{s}$

Table 4.2 Parameters of the sputter deposition

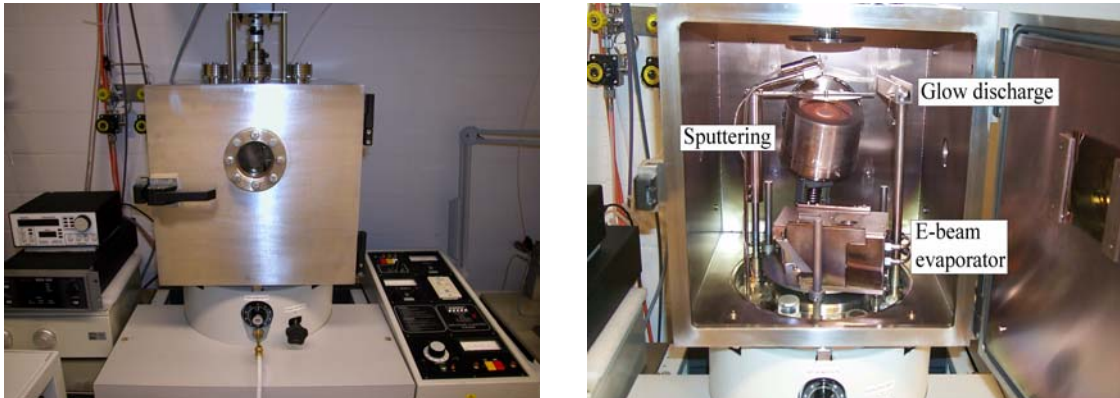


Figure 4.1 Left: deposition system Edwards E306; right: inside vacuum chamber

4.1.1.2 Measurements and Discussion

Figure 4.2 shows measurements on 3 different aluminium thin films with nominal thicknesses of 100nm, 200nm and 300nm, which are deposited according to Chapter 4.1.1.1.

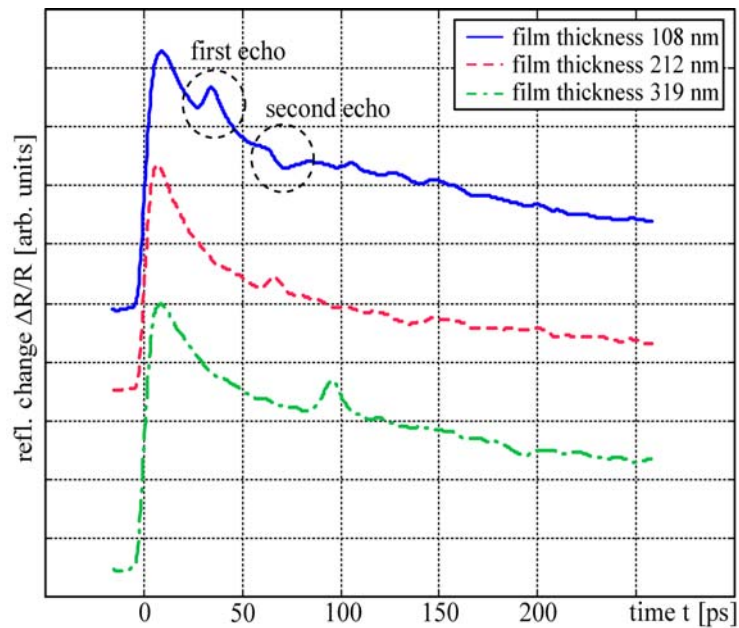


Figure 4.2 Measurement on aluminium thin films

According to the explanations in Chapter 3.1 the reflectivity jump at the beginning ($t = 0$ ps) is caused by the induced temperature and strain. The excited strain pulse propagates towards the interface of the aluminium thin film and the sapphire substrate. The acoustic pulse is partly reflected at the interface according to the acoustic reflectivity coefficient r , which amounts to 0.408. No polarity change occurs because the acoustic reflection coefficient is positive. Reaching the free surface, the acoustic pulse causes a reflectivity change due to the photoelastic effect. These peaks in reflectivity are superimposed on the smooth decrease which is caused by the decreasing temperature. At the free surface the acoustic pulse is totally reflected with a polarity change, which is the reason for the polarity change of the next reflectivity peak. In the case of the 100nm aluminium film, the first reflection is measured after 36ps, the second after 72ps and the third is observed after approximately 108ps. The first reflection of the 200nm film occurs shortly before the second reflection of the 100nm film because of the slightly smaller thickness, which is given in the inset of Figure 4.2. The case with the ~ 300 nm film is also similar. Each curve of Figure 4.2 represents an average of 30 single measurements. The pump laser power is in the order of 400mW.

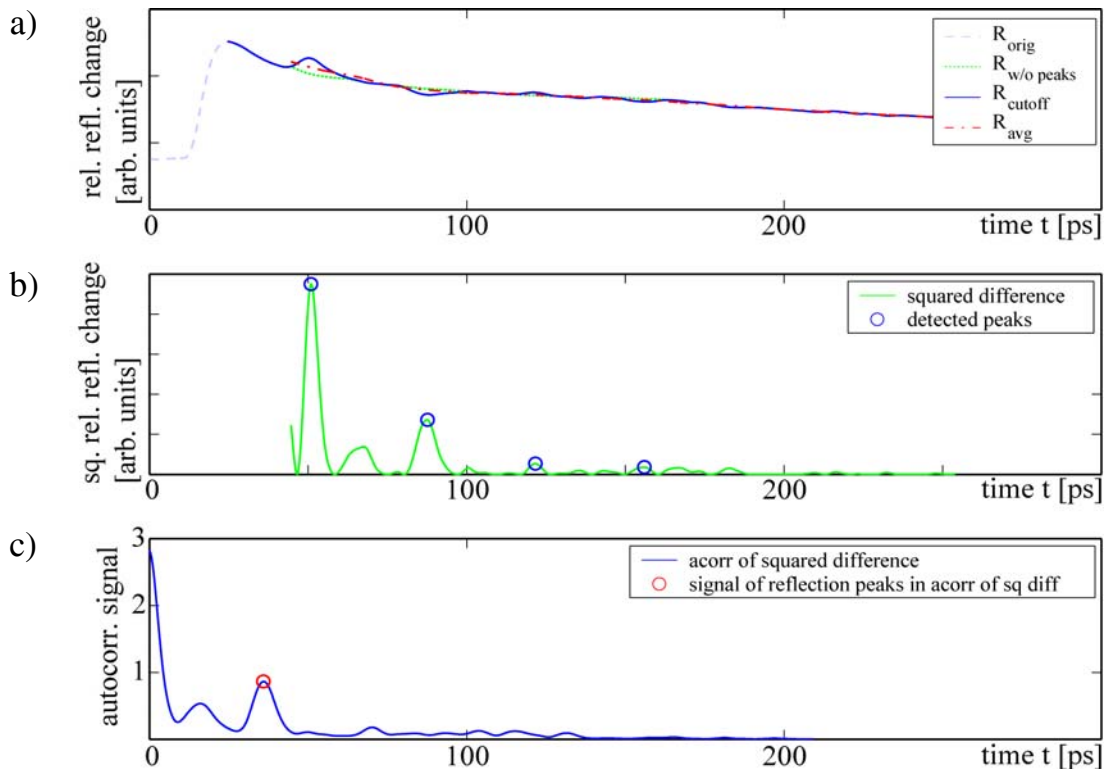


Figure 4.3 Evaluation of measurement on 100nm aluminium film on sapphire substrate, a) original measurement and filtered, b) squared difference of the relative reflectivity change, c) auto correlation signal

Figure 4.3 shows the separation of the thermally and the acoustically caused modifications of the optical reflectivity change at the surface. The detailed evaluation of the measurement of the 100nm aluminium thin film is presented. In the upper graph the original measurement is presented (dashed line) and the part which is used for the evaluation is illuminated (solid line). In this evaluation, the origin of time is set at the beginning of the measurement, not at the occurring reflectivity jump. The measured data is low-pass filtered and subtracted from the original measurement. The result is squared and the peaks in reflectivity are identified through local maximum search. The evaluated mean value of the time of flight between the detected peaks is 35.00ps. The lower graph shows the auto correlation signal of the squared difference with an automatically identified maximum at 36.00ps. This procedure enables the determination of the bulk wave velocity without any model or fitting process with an accuracy of better than $\pm 5\%$. Thus, the determination of the bulk wave velocity or the determination of the thickness of a single layer is very fast.

The thickness of thin films and the deposition method can have a strong influence on the bulk wave speed of the deposited material (see for example Lee Y.-C. et. al. [32]). The influence of the thickness and the sample preparations on the bulk wave velocity of aluminium films is characterized using 11 samples with different thicknesses varying from approximately 21nm to 300nm. First, the film thickness is determined with profilometer measurements. Second, the bulk wave velocity is calculated with the round trip time (i. e. time between the first and second echo) of the bulk acoustic wave (BAW), determined by the measured reflectivity change. In Figure 4.4 (left) three pump-probe measurements on a 40nm, 63nm and 86nm aluminium film on random oriented sapphire substrates are shown. The profilometer and the pump-probe measurements of each thin film are performed on the same small area ($\sim 2 \times 2$ mm) to minimize errors caused by the variation of the film thickness over the whole sapphire wafer. The average value of the wave speed of each thin film sample is computed with the average of the round trip time and the average of the thickness measurements. The results are presented in Figure 4.4 (right). Every measured wave speed is inside the indicated error bands. The errors in thinner films increase. With decreasing thickness the wave speed is nearly constant and independent of the thickness of the aluminium thin films. When compared to the value for bulk material, the values for films which are thicker than 40nm, lie within $\sim 5\%$ error limits. For aluminium films thinner than 40nm a strong decrease of the wave velocity in the order of 25% is observed but these values are not considered in Figure 4.4 (right) because of the following uncertainties.

A decrease in the bulk acoustic wave velocity can be caused by changes in the material properties (Young's modulus or Poisson ratio) or the density. If it is assumed that the density of a thin film remains constant, independent of the film thickness, a change in the wave velocity must be the result of variations of the material properties, which can be caused by several reasons:

- In Mizubayashi H. et. al. [45] and Mizubayashi H. et. al. [44] a decrease of the Young's modulus of films thinner than 100nm is reported and furthermore it is noted that the density shows a good agreement with the values for bulk aluminium. But for thin films with thicknesses smaller than 20nm the Young's moduli are only fractions of the values for bulk aluminium. The decrease of the Young's moduli with decreasing thicknesses depend on deposition conditions. It is reported in [45] that the decrease of the Young's moduli of films deposited in a vacuum of 10^{-4} Pa on a silicon substrate (100) starts with thicknesses in the order of 200nm. The decreasing tendency is smooth and gets stronger for film thicknesses below 20nm. For films deposited at 10^{-5} Pa the decrease starts at film thicknesses of approximately 25nm and is much stronger than in the previous case. Our aluminium thin films are deposited at a pressure below $2 \cdot 10^{-3}$ Pa (Table 4.1) on sapphire substrates. The decrease in the bulk acoustic wave velocity starts at about 40nm. In Mizubayashi H. et. al. [45] it is argued, that the reason for the decrease of the Young's modulus is caused by an increasing effect of grain boundaries for smaller film thicknesses. It is assumed that the grain boundary subregions show a lower Young's modulus, whose influence is increased by the smaller grain size.
- On the other hand, one can also expect an influence of a slightly increased average temperature induced by the laser pulses.
- The accuracy of the profilometer is in the order of 5nm and it is obvious that inaccuracies of the thickness determination plays a more significant role with thinner films.

For the thicker films the Young's modulus is estimated of 71GPa, which is also in good agreement with the modulus of bulk aluminium.

Measurements on sputtered aluminium thin films, manufactured according to Table 4.2 show a decrease of the wave velocity of about 20% (see for example one measurement in Figure 4.4 (left) (circle)).

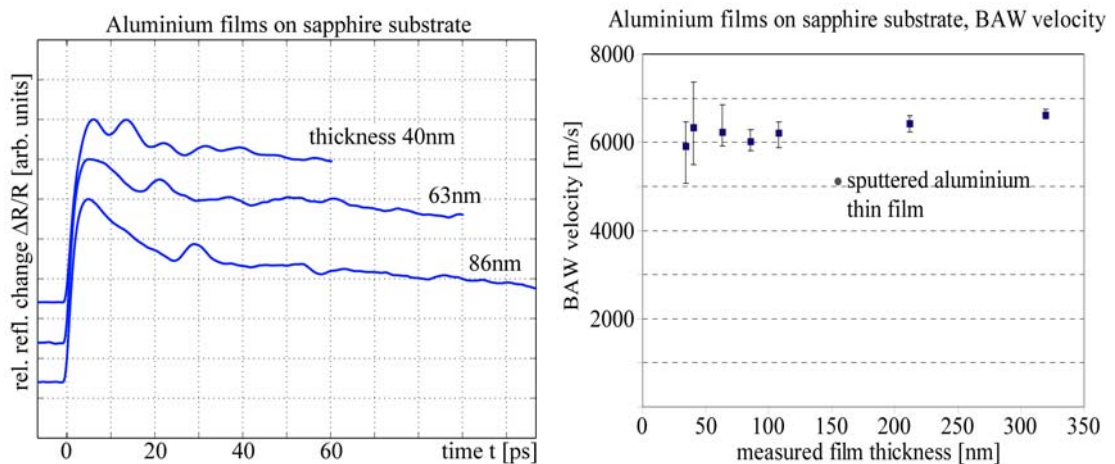


Figure 4.4 Left: measurements on very thin aluminium films; right: summary of the bulk wave speed of aluminium with different thicknesses

The material properties of sputtered aluminium thin films can vary strongly with the deposition condition. An overview of the variation of the Young's modulus of sputtered aluminium thin films with the deposition conditions, especially with the argon pressure in the deposition chamber, is given by Chinmulgund M. et. al. [9]. The Young's modulus is estimated with the determined wave velocity taken from the measurements and the known Poisson's ratio of the aluminium thin film. For the density $\rho = 2700 \text{ g/cm}^3$ is chosen and for the Poisson's ratio ν the value 0.34 is taken. From the measured value of the bulk wave velocity one can calculate a Young's modulus of 45.7GPa (47.45GPa with Poisson's ratio ν 0.33) for the DC planar magnetron sputtered aluminium thin film, which is in perfect agreement with the measured results of Chinmulgund M. et. al. [9]. Since the measured property is the bulk wave velocity it is important to know that the calculated Young's modulus depends on the used density and Poisson's ratio. Therefore they are given in this chapter and also in Appendix A.

Thickness measurement of wafers

For the measurement of thicknesses or material properties, such as the bulk acoustic wave velocity or the estimation of the Young's modulus of coated wafers, this technique is the right approach. Without any additional effort it is possible to determine the time of flight of the acoustic pulse on several points on a wafer.

Grid measurement Al-film (140nm) on a sapphire substrate

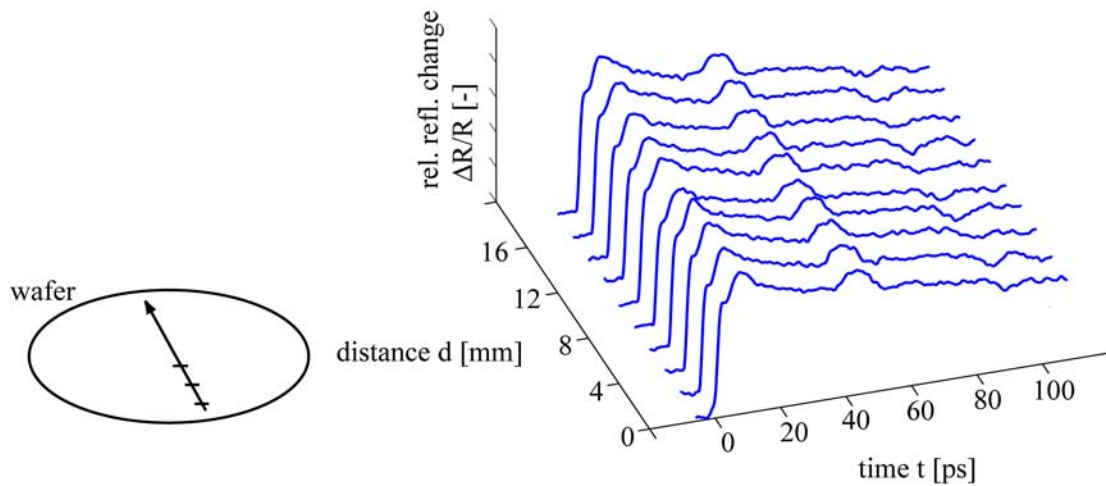


Figure 4.5 Grid measurement of 140nm aluminium thin film on sapphire substrate

Figure 4.5 shows an example of a line scan of a 2" wafer. Every 2mm a measurement of the bulk acoustic wave propagation is performed. Since the first acoustic reflections occur almost at the same time the measurements show that the thickness of the 140nm aluminium film is nearly uniform over the scanned area. This application of the measurement technique is used in chip production lines for monitoring and analyzing [67].

4.1.1.3 Influence of the measurement configuration and the boundary conditions

The influence of the measurement configuration and the corresponding boundary conditions has been discussed by Wright O.B. et. al. [88]. If a measurement configuration similar to Figure 4.6 is used, it has been shown that the strain pulse is unipolar in contrary to previous experiments, where the excitation was on a stress free surface. Some new aspects such as the influence of the measurement configuration on the measured temperature distribution (thermal reflectivity change) and corresponding numerical simulations are added in this chapter.

For the measurements presented in Figure 4.6, the experimental setup is modified in a way that the probe and the pump laser pulses hit the specimen from opposite sides (Figure 3.19). Additionally, microscope objectives are used to focus both laser pulses towards the specimen. This results in a smaller spot size and a higher signal/noise ratio while working with the same average power.

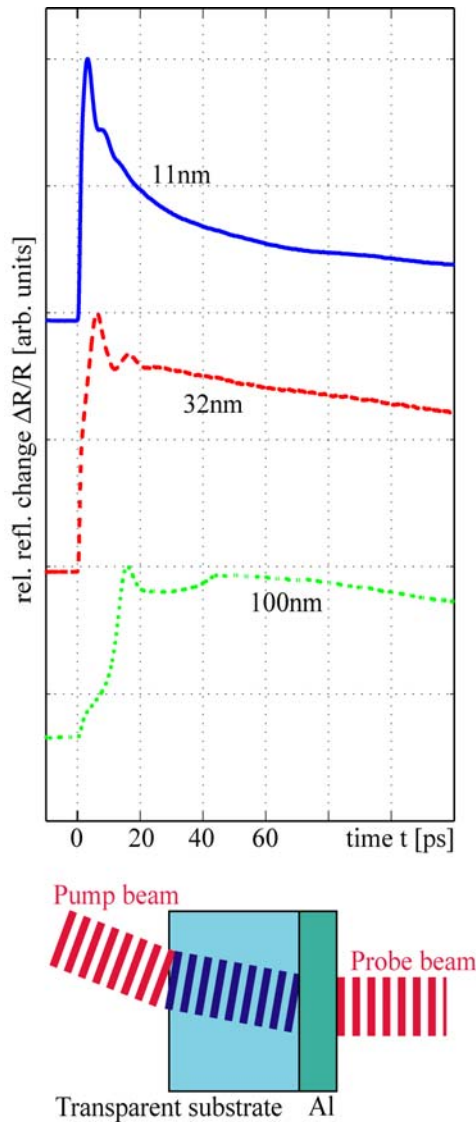


Figure 4.6 Measurements of aluminium thin films on glass using the indicated configuration

For the measurements presented in Figure 4.6 a transparent substrate (borofloat glass) is coated with different aluminium films. The excitation of the acoustic pulses is done through the transparent substrate - the reflectivity is still measured on the free surface of the aluminium film. In the first case, the aluminium film has a thickness of 11nm. The incident pump pulse is partly absorbed by the semitransparent 11nm aluminium thin film. The absorption of the pump laser pulse initiates an instantaneous heating of the very thin aluminium coating. The temperature distribution is nearly uniform in the thickness direction. Usually, the initiated temperature decreases exponentially with increasing depth. But due to the very small thickness (Figure 2.2, right) of the aluminium layer, which is in the order of the absorption length, the temperature distribution within the aluminium layer can be assumed to be uniform. This is the reason why the sudden increase at a time of approximately 0ps and the slow decrease of the measured reflectivity change (which is caused by the temperature in the aluminium thin film) can be measured on the opposite side of the excitation. The measured reflectivity change of the 11nm aluminium is almost the same as the measurement in a configuration according to Figure 3.18, where the excitation and the measurement of the acoustic pulse is performed from the same side.

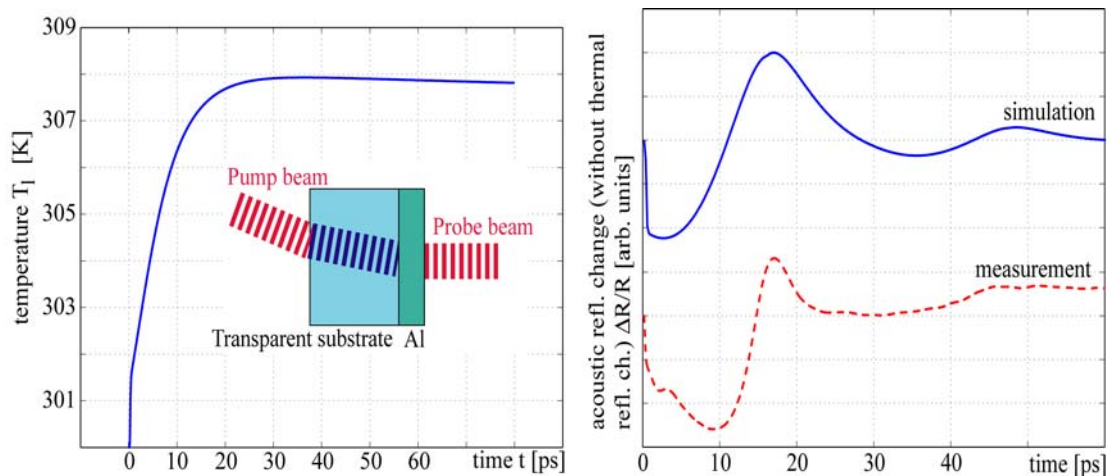


Figure 4.7 Left: simulation of the induced temperature in the aluminium thin (thickness 100nm), measured at the free surface of the thin film according to the indicated configuration; right: measurement and simulation of the reflectivity change caused by the predominant strain distribution (acoustic reflectivity change)

The characteristics of the reflectivity change measured in the second case on a 32nm aluminium film is in general similar to the 11nm film. But in the third case, the measurement in a configuration, according to Figure 3.19 of a specimen (borofloat glass) coated with 100nm aluminium, looks different. The reflectivity change caused by the induced temperature in the thin film is approximately proportional to the temperature increase. A simulation of the increased temperature is shown in Figure 4.7 (left). The simulation is performed with the material properties of Appendix A and the laser fluence is set to 15J/m^2 , which is approximately the same as in the experiments. Uncertainties in the laser fluence are mainly caused by the estimation of the laser spot size. Borosilicate glass properties are given in Table 4.10. The temperature at the stress free front surface increases shortly after the absorption of the pump laser pulse at the back. During non-equilibrium short-pulse laser heating of metals the electrons of a metal absorb the laser radiation energy first because of their very small heat capacity. These so-called hot electrons diffuse very fast through the metal film and lose their energy by inelastic electron-phonon scattering processes (Chapter 2.2.3). The subsequent diffusion and the energy transferred from the electrons to the lattice leads to a further increase of its temperature. After that, the temperature stays nearly constant because the heat diffusion into the glass substrate, which is considered in the simulation, is very slow. Although, the spot size is reduced by the means of microscope objectives, the radius is still more than thirty times bigger than the film thickness.

Thus, the simulation is performed in a one-dimensional way, according to Chapter 2.2.3 with the extension described in Chapter 4.1.3.3.4. The fast increase in reflectivity visible in the measurement on the 100nm film presented in Figure 4.6, is caused by the induced temperature. If we subtract the temperature reflectivity change, which is proportional to the surface temperature, from the measurement in Figure 4.6 we can compare the resulting mechanical response with the simulated one. The reflectivity change caused by the electron temperature is neglected. The comparison is presented in Figure 4.7 (right) and shows a good agreement. The strain pulse is excited at the interface of the glass and the aluminium thin film and is affected by the changed boundary condition. Hence, the strain pulse is unipolar in contrary to previous simulations, where the excitation was on a stress free surface (Wright O.B. et. al. [88]).

4.1.2 Platinum thin films

Since the optical reflectivity of platinum is lower than the reflectivity of aluminium, the induced temperature is usually higher when using the same laser power.

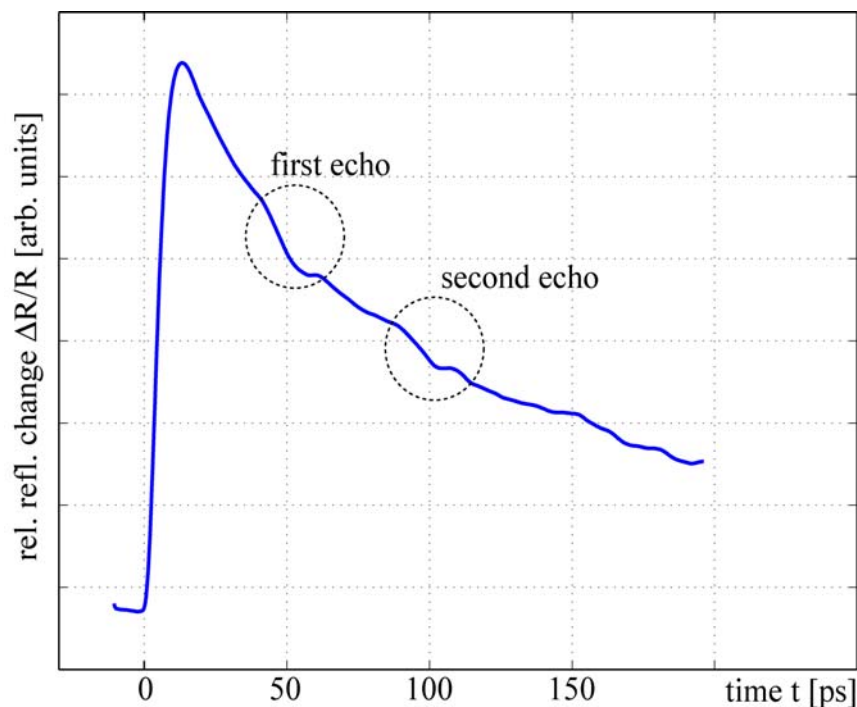


Figure 4.8 Measurement on 90nm platinum film

Nevertheless, the amplitude of the excited acoustic pulse is about half the one in aluminium (Figure 2.3) due to the smaller expansion coefficient. The height of the peaks in reflectivity is much lower than in the measurements with aluminium thin films, which is caused by the lower amplitude of the excited

acoustic pulse and the difference in the photoelastic properties. The measurement indicates that the photoelastic properties of platinum are smaller in contrast to aluminium and it shows clearly that an appropriate photoelastic response is essential for the detection of the acoustic pulses. This should be considered when measurements on other thin film materials are performed. Both acoustic reflections have the same negative sign because on the interface and on the free surface the signs of the acoustic pulses are changed. According to Table 2.3 the acoustic reflection coefficient of platinum-sapphire combination amounts to -0.35. The time of flight of the acoustic pulse is 45.5ps, which corresponds to a thickness of 90.3nm.

4.1.3 Multilayers, stacks of thin films

This measurement technique is a good approach to measure thicknesses or material properties of complete thin film stacks. Apart from unknown material properties of several thin films, the application of this technique for the detection and determination of interface layers between two different thin films, or the determination of material properties in very thin underlying diffusion barrier layers, are discussed in this section. Also, other groups performed various measurements on many different thin film-substrate combinations, such as presented by Perrin B. et. al. [50], Wright O.B. et. al. [91] and Grahn H.T. et. al. [18].

4.1.3.1 Aluminium - Gold

In Figure 4.9 a measurement of the picosecond ultrasound propagation in an aluminium-gold-silicon oxide multilayer is presented. The acoustic pulse is excited at the free surface of the aluminium top layer and propagates towards the aluminium gold interface where the acoustic pulse is partly reflected and partly transmitted. The transmitted part is again partly reflected on the gold-silicon oxide interface.

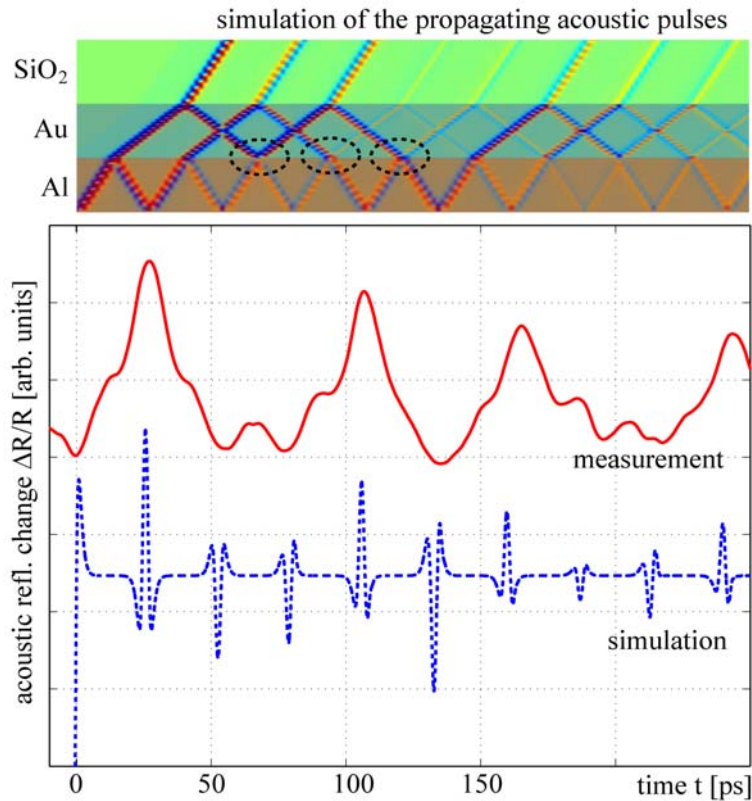


Figure 4.9 Measurement on a aluminium-gold-multilayer (measurement (solid line) and simulation based on a simple model (dashed line) by J. Bryner [5])

The illustration of the propagation of the acoustic pulses above the reflectivity change in Figure 4.9 makes it possible to assign the peaks of the reflectivity change to the corresponding acoustic reflections. For the simulation it is assumed that both films (aluminium and gold thin film) have the same thickness of 85nm because the measured total thickness is 170nm. The material properties used for the simulation are the same as in Chapter 2 (Table 2.1, Table 2.2 and Table 2.3) and Appendix A, respectively. The performed simulation is based on a very simple model and is aimed for discussing the wave propagation characteristics. Therefore the shape of the reflectivity peaks of simulation and measurement do not fit very well. Since the bulk wave velocity of gold is approximately the half of aluminium, the strain pulses in the aluminium and gold thin film superimpose periodically at the aluminium-gold interface, which is indicated by the circles in Figure 4.9. Gold has the tendency to diffuse into aluminium especially at higher temperatures, which is the motivation for investigations presented in the following chapter.

4.1.3.2 Functionally graded materials (FGM), in-depth profiling and applications

This section deals with quantitative in-depth profiling methods as described by Vollmann J. et.al. [87]. The material combinations and the dimensions of the specimen are chosen in accordance with the parameters for an optimal detectability. Several methods and techniques have been tested and compared, in order to obtain a more or less defined continuous transition of the mechanical properties of one layer to the properties of the neighboring layer within a few 10nm. Among those methods are an electron beam vapor deposition chamber with two beams and targets, which can individually be controlled, an alternating sequence of various layers of different thicknesses, ion beam implantation, and thermally induced diffusion. Thermally induced diffusion turned out to be the best choice since this method allowed the realization of series of varying thicknesses by varying the temperature. A standard specimen consists of a vapor deposited 30nm Au layer embedded between two 60nm Al layers on a sapphire (Al_2O_3) substrate. A series of specimen has been exposed to 100°C, 200°C and 300°C in a vacuum oven during 30 minutes. In parallel, a series of reference specimen consisting of 150nm Al films on sapphire substrates has been exposed to the same temperature cycles, in order to exclude potential effects of the grain structure or of the optical surface reflectivity on the photo-acoustic detection.

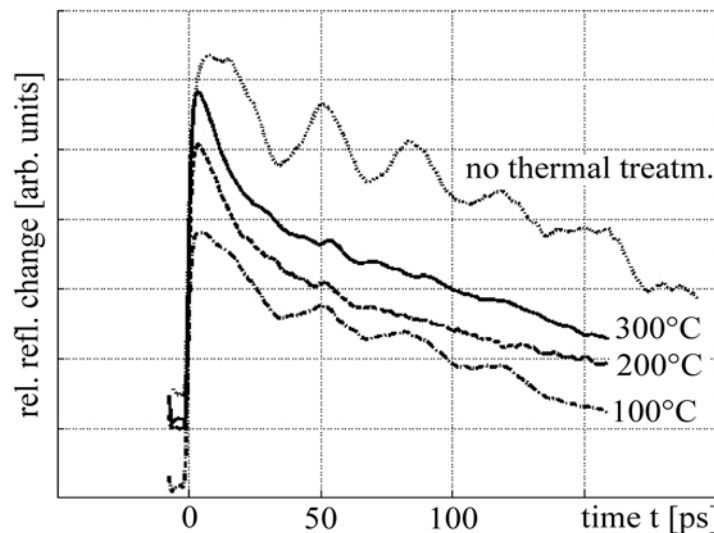


Figure 4.10 Measurement of the diffusion at the interface of aluminium-gold thin films after exposure to different temperatures (figure by Vollmann J. et.al. [87], modified)

The diagram of Figure 4.10 shows four independently measured reflectivity curves. The thicknesses of the multilayer are: 60nm Al / 30nm Au / 60nm Al on a sapphire substrate. Each curve represents an average of 50 individually

measured curves.

In the uppermost reflectivity curve one can see the periodic alternation of the optical reflectivity change which is caused by the stress pulse echoes reaching the surface, superimposed on the thermal effects. The acoustic pulse is mainly reflected at the first Al/Au interface. So, in order to demonstrate the dependence of the reflection/transmission ratio on the wavelength/smooth-acoustic-interface-thickness ratio experimentally, the thickness of the soft acoustic interface needs to be varied. This has been realized by the exposure of a series of equally manufactured specimen to different temperature treatments, which leads to different grades of thermally induced intermetallic diffusion. The broadening of the diffusion zone causes variations in the acoustic interface, which results according to Vollmann J. et. al. [87] in a wavelength dependent acoustic reflection coefficient.

Figure 4.10 shows the photo acoustic measurements of the three standard specimen which were heated up to 100°C, 200°C and 300°C, in comparison with the measurement of an untreated specimen. The measured reflectivity change curves of the thermally treated specimen clearly indicate the broadening of the diffusion zone, i.e. the broadening of the soft acoustic interface, suppresses the acoustic contrast and therefore, the main part of the propagating acoustic pulse passes the smooth interfaces and is reflected at the Al/sapphire interface. So, one can see, that the echo which occurs at the Al/sapphire substrate interface remains detectable even after the thermal treatment of 300°C. Rutherford back scattering (RBS) measurements, which give material profiles of the cross section, as well as a more detailed description of the one-dimensional bulk wave propagation in smoothly varying interfaces, has been presented by Vollmann J. et. al. [87].

The Rutherford back scattering (RBS) measurements are performed at the PSI/ETH Ion Beam Physics Laboratory. RBS relies on the fact that the energy of a MeV ion backscattered from a target material is a function of the target atomic mass and the depth at which the scattering took place. Therefore, quantitative depth profiles of the elemental composition of the target can be obtained. A depth resolution of 2 nm can be obtained in the near surface region. A detailed description of the method is given by Chu W.K. et al. [10].

Since the acoustic reflection and transmission of broadened interfaces becomes wavelength dependent, this technique can be used for filtering high frequency bulk acoustic waves (Vollmann J. et. al. [86]). An important requirement for the realization of filter devices using this effect, is the defined fabrication of the appropriate interfaces. Such filter devices can be considered as an application of functionally graded materials.

4.1.3.3 Copper - tantalum - tantalum-nitride

For some years copper has been replacing aluminium in the semiconductor industry. Copper has the advantages of superior electrical and thermal properties, which are necessary for building even higher performing and smaller microprocessors. Aluminium on the other hand, is a poorer electrical and thermal conductor but has one essential property that copper does not have - aluminium does not diffuse into the silicon semiconductor. To prevent copper diffusing into the silicon semiconductor thin barrier layers, i.e. tantalum or tantalum-nitride are deposited in between.

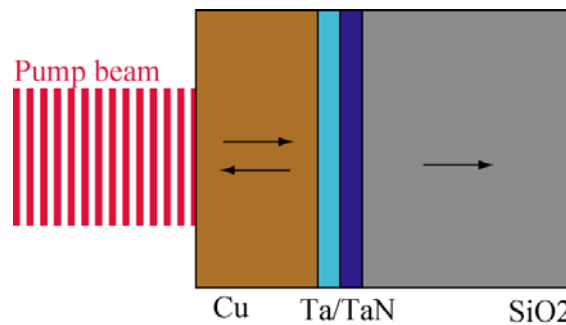


Figure 4.11 Example of copper-multilayer-stack

The wide variety of problems and defects occurring in chip manufacturing is reported in [31]. With copper, new materials and new processes are used in the semiconductor industry, which demand together with the permanently shrinking feature sizes, corresponding metrology techniques.

4.1.3.3.1 Barrier layers

To avoid copper diffusion into a silicon semiconductor diffusion barrier layers are deposited in between. Apart from a single tantalum (Ta) layer, also tantalum-nitride (TaN), tantalum/tantalum-nitride multilayers and tungsten-nitride (WN) layers are suitable candidates for diffusion barriers below copper films. According to Chin B.L. et. al. [8] tantalum and tantalum-nitride are implemented because of the specific film properties that are required for integration in the copper metallization scheme. In addition to being a good copper diffusion barrier, tantalum and tantalum-nitride have good adhesion to dielectric and copper films. Since tantalum-nitride has better diffusion barrier properties than tantalum but the tantalum layer, on the other hand, has other advantages regarding the reliability, both layers are combined to take advantage of each of the individual film's properties (Chin B.L. et. al. [8]).

4.1.3.3.2 Problem formulation and solution strategy

Problem formulation

The semiconductor industry has an increasing demand to verify the proper deposition of each individual layer in a non-destructive way. Therefore this chapter deals with the application of picosecond ultrasound for the non-destructive determination of the thickness of diffusion barrier layers and its limitations and accuracy. It is of interest for semiconductor industry if the thicknesses of the diffusion barrier layers can be determined below a copper layer which is even more challenging because in copper it is not possible to generate acoustic pulses with such high frequencies as known from aluminium. The reason is the fast heat conduction caused by the electrons during the absorption of the optical laser pulse, which is illustrated in Figure 2.17. In addition it is discussed if it is possible to measure the thickness of each part of a tantalum/tantalum-nitride multilayer below a copper top layer. The problem formulation in summary:

- limitations and accuracy of the non-destructive determination of the thickness of a single diffusion barrier layer (Ta or TaN) below a copper film using picosecond ultrasound
- non-destructive determination of the thickness of each part of Ta-TaN-multilayer below a copper top layer using picosecond ultrasound

Solution strategy

Since no other paper have been published discussing these questions, the following solution strategy is chosen:

- Determination of bulk wave velocity of the Cu, Ta and TaN layers.
- Thermomechanical simulation of Cu/Si, Cu/Ta/Si and Cu/Ta/TaN/Si multilayers to investigate the limitations of the thickness determination of the diffusion barriers.

Since the mechanical properties (for example Young's moduli) and therefore the bulk wave velocity vary strongly with thickness, deposition technique and deposition conditions it is necessary to determine the bulk wave velocity of each layer. Furthermore no reliable values of the mechanical properties of Ta and TaN were available at the time these simulations and measurements were performed. But their properties are very important to determine their dimensions below a copper film.

The limitations and accuracy of the thickness determination of a single or multilayered diffusion barrier below a copper top layer are investigated using thermomechanical simulations because the experimental setup presented in this

thesis is optimized for aluminium and so an optical wavelength of 800nm is used. For measurements on copper the optical wavelength must be in the order of 600nm or 400nm because of the photoelastic behavior. While the transformation of the laser pulses with a wavelength of 800nm to a wavelength of 400nm could easily be realized by second harmonic generation (SHG) with a beta barium borate (BBO) crystal, most of the detecting devices and beam guiding is realized with components, which are chosen for a small spectral bandwidth around 800nm.

4.1.3.3.3 Detailed procedure for investigating diffusion barrier layers

Determination of film properties (bulk wave velocity) of Cu, Ta and TaN

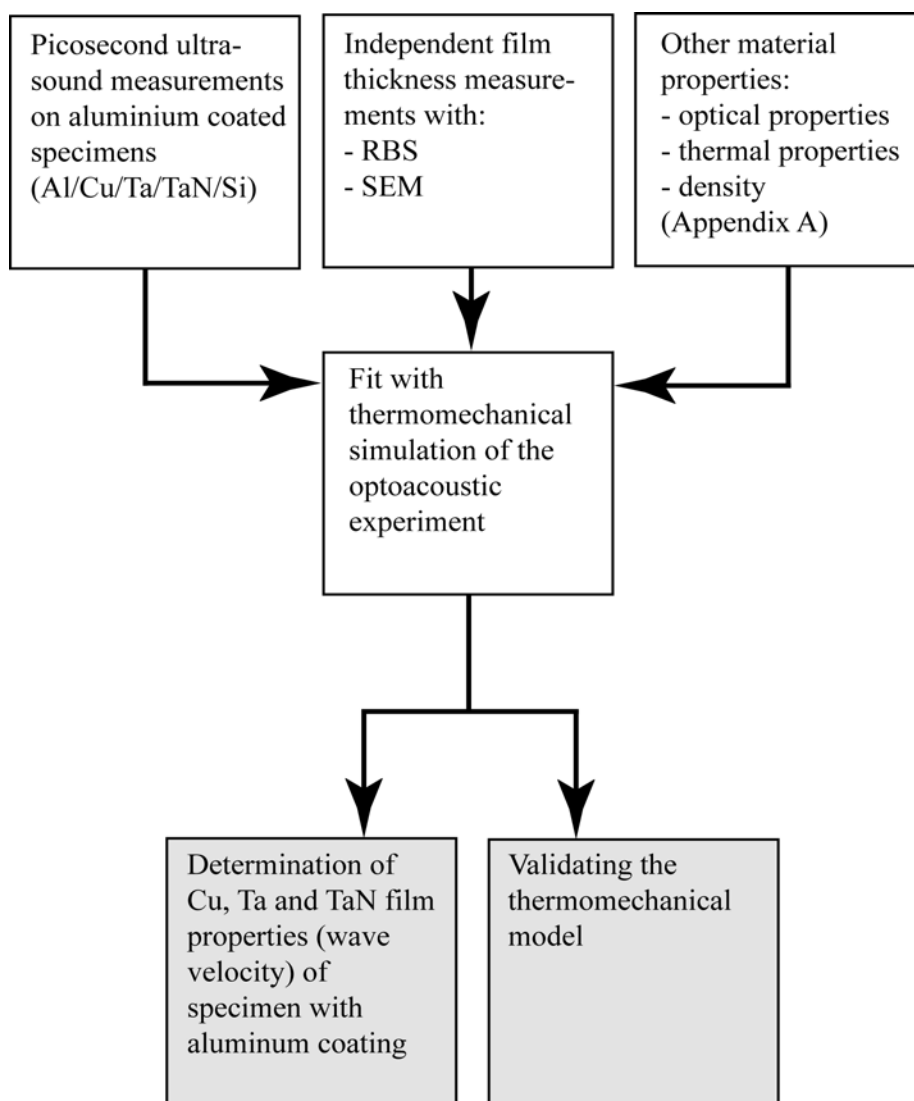


Figure 4.12 Detailed procedure for the determination of film properties bulk wave velocity) of Cu, Ta and TaN layers (Chapter 4.1.3.3.5)

On 6 different specimens, which are listed in Table 4.3, simulations and measurements are performed.

<i>Number</i>	<i>Specimen with nominal thickness</i>
1	Ta 30nm/Si(100)
2	Ta 60nm/Si(100)
3	Ta 30nm/TaN 30nm/Si(100)
4	Ta 60nm/TaN 30nm/Si(100)
5	Cu 100nm/Ta 30nm/TaN 30nm/Si(100)
6	Cu 100nm/Ta 60nm/TaN 30nm/Si(100)

Table 4.3 Specimens

The different specimen stacks consist of copper, tantalum or tantalum nitride and additionally, for the measurements using picosecond ultrasound an aluminium film has to be deposited as the top layer. This is necessary, because the experimental set-up presented in this thesis is optimized for aluminium. The used optical wavelength of 800nm is not suitable for measurements on copper. The deposited top aluminium layers are about 40nm thick, except for specimen 3, which is coated with three different aluminium films (thicknesses are given in the corresponding figures in Chapter 4.1.3.3.5).

According to Figure 4.12 the procedure for the determination of the mechanical properties (bulk wave velocity) of the Ta, TaN and Cu films is as follows: First of all measurements with picosecond ultrasound are performed on each specimen of Table 4.3 with the additional aluminium coating.

Then independent measurements of the thicknesses are necessary (Figure 4.12), since the nominal thicknesses given in Table 4.3 are only guiding values. Therefore, thickness measurements using Rutherford back scattering (RBS, short description in Chapter 4.1.3.2) are performed. With the Rutherford back scattering measurements the stoichiometry of the layers is also measured and with it a significant and unexpected argon component in the TaN layer has been detected. Very thin oxide layers on the tantalum film, which are measured with Rutherford back scattering, are not taken into account in the simulations. But their thickness is added to the measured thickness of the tantalum layer. Additionally, the thickness is measured in images of the cross section of the thin films using SEM (scanning electron microscopy). But the contrast is not always high enough to resolve all layers, espe-

cially the Ta and TaN layer. The result of the thickness measurements with Rutherford backscattering and SEM are listed in Table 4.4.

In the third step the results of the thermomechanical model (with extensions described in Chapter 4.1.3.3.4) are fitted to the measured results by varying the bulk wave velocity in the model. The density, on the other hand, is kept constant. Specimen 2, 4 and 6 are used for the determination of the bulk wave velocity. The other specimen of the same type but with other film thicknesses are used for validating the model and the fitted results.

All other material properties which are necessary for the simulations (Figure 4.12), such as the optical properties, the thermal properties and the density are taken from Appendix A.

Procedure for the detection threshold quantification using thermomechanical simulations

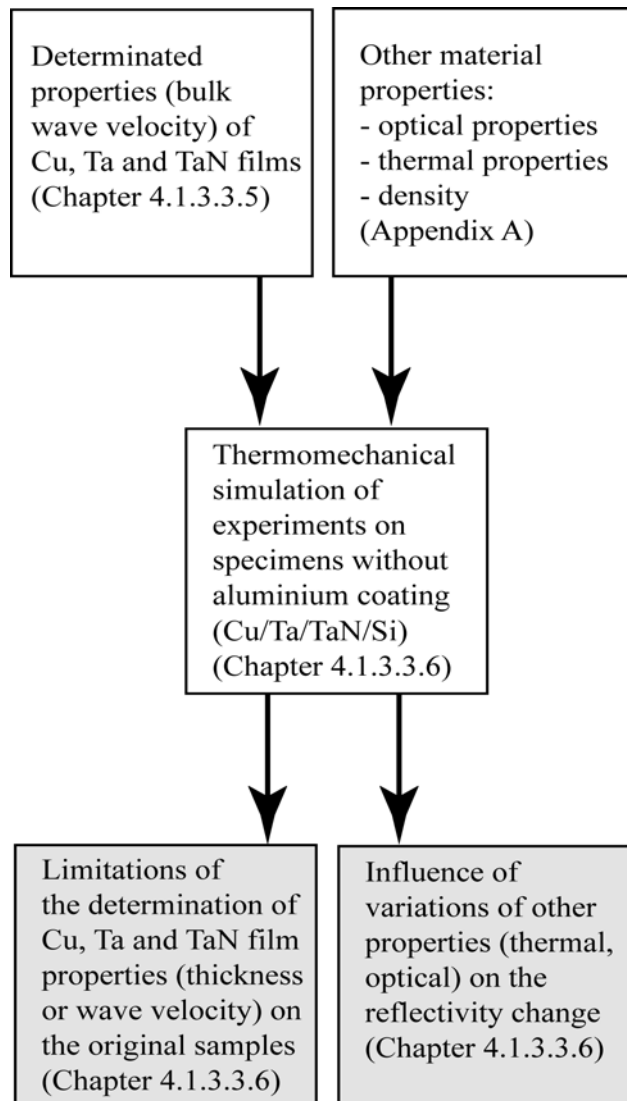


Figure 4.13 Detailed procedure for investigating the limitations of the thickness determination of diffusion barrier layers by means of thermomechanical simulations (Chapter 4.1.3.3.6)

For the discussion of the limits of the thickness determination of diffusion barriers below a copper film accurate simulations with extensions according to Chapter 4.1.3.3.4 are used. The reason therefore is that for measurements the optical wavelength would have to be modified, as mentioned before. In this simulation properties of Appendix A as well as the determined wave velocities of Ta and TaN are used, for comparison (procedure see Figure 4.13). Also the influence of variations of other properties, such as the thermal conductivity of

the tantalum layer, is discussed.

4.1.3.3.4 Extension of the simulations - considering heat flux in the lattice

The simulation of the non-equilibrium heating process, of which basics are described in Chapter 2.2.3, is extended with a term corresponding to the heat flux in the lattice system $\nabla(K_l \nabla T_l)$, so that the extended two-temperature model can be described with the following equations (Qiu T. et. al. [60])

$$C_e(T_e) \frac{\partial T_e}{\partial t} = \nabla(K_e \nabla T_e) - G(T_e - T_l) + Q \quad (4.1)$$

$$C_l \frac{\partial T_l}{\partial t} = \nabla(K_l \nabla T_l) + G(T_e - T_l) \quad (4.2)$$

T_e , T_l , C_e , C_l , K_e and K_l are the temperature, heat capacity and thermal conductivity of the electron (e) and the lattice (l) system, respectively. G is the electron-lattice coupling constant and Q the laser heating source term. Heat conduction in the in-plane direction of the thin film is neglected, therefore, both the equations describing the heating process and the mechanical response are solved only in the thickness dimension. The temperature dependence of the electron heat capacity $C_e(T_e)$ and the thermal conductivity $K_e(T_e)$ is given in Chapter 2.2.3. The boundary conditions are chosen as follows (Qiu T. et. al. [60]):

The heat loss at the surface is small compared to the incident laser intensity and hence, an insulating boundary condition is assumed

$$K_l \frac{\partial T_l}{\partial z} \Big|_{Surface} = K_e \frac{\partial T_e}{\partial z} \Big|_{Surface} = 0 \quad (4.3)$$

At the interfaces of the different thin films the heat flux is continuous in the lattice system

$$K_{l_n} \frac{\partial T_l}{\partial z} \Big|_{Material\ n} = K_{l_{n+1}} \frac{\partial T_l}{\partial z} \Big|_{Material\ n+1} \quad (4.4)$$

$$T_l \Big|_{Material\ n} = T_l \Big|_{Material\ n+1} \quad (4.5)$$

The heat flux out of the first layer provided by the electrons is neglected.

$$K_{e_1} \frac{\partial T_e}{\partial z} \Big|_{Interface\ 1} = 0 \quad (4.6)$$

If this simulation is used together with a numerical solution of the wave equation, it is connected with the resulting lattice temperature by adapting Equation (2.35) for each layer n .

$$\sigma_{z, therm} = -(3\lambda_n + 2\mu_n) \alpha_n \Delta T_l(z, t) \quad (4.7)$$

In general, the numerical solution is realized in a similar way as presented in Chapter 2.2.3.

4.1.3.3.5 Measurements and simulations with aluminium top layer for the determination of the bulk wave velocity of Ta, TaN and Cu

In this subsection the measurements and simulations of copper-tantalum-multilayer stacks, which are coated with an aluminium film (thickness $\sim 40\text{nm}$ except specimen 3), are discussed. All presented measurements with picosecond ultrasound are an average of 10 or 30 single measurements, using a pump laser power of approximately 400mW and a probe laser power of about 20mW. The spot size is in the order of $100\mu\text{m}$.

For the 6 different specimens (Table 4.3) thickness measurements using RBS and SEM are presented in Table 4.4.

<i>Number</i>	<i>Specimen with nominal thickness</i>	<i>Measured thickness^(a)</i>	<i>Determined with SEM^(b)</i>	<i>Used thickness for wave velocity</i>	<i>Determined thickness^(c)</i>
1	Ta 30nm/ Si(100)	43nm/sub- strate	-	-	38nm (44nm)/ sub.
2	Ta 60nm/ Si(100)	71nm/sub- strate	79nm/sub.	71nm (79nm)/ sub.	-
3	Ta 30nm/ TaN 30nm/ Si(100)	31nm/18nm/ substrate	56nm (Ta+ TaN)/sub- strate	-	31nm*/ 20nm/sub.
4	Ta 60nm/ TaN 30nm/ Si(100)	67nm/18nm/ substrate	86nm (Ta+ TaN)/sub- strate	67nm**/ 18nm/sub- strate	-
5	Cu 100nm/ Ta 30nm/ TaN 30nm/ Si(100)	150nm/ 35nm/21nm/ sub.	157nm/ 70nm (Ta+ TaN)/sub.	-	153nm/ 58nm (Ta+ TaN)/sub
6	Cu 100nm/ Ta 60nm/ TaN 30nm/ Si(100)	130nm/ 69nm/17nm/ sub.	130nm/ 98nm (Ta+ TaN)/sub.	130nm/ 69nm/ 17nm/sub.	-/90nm (Ta+TaN)/ substrate

*Table 4.4 Specimens ^(a) - measured with RBS, ^(b) - measured from SEM image (for bilayer diffusion barriers (Ta+TaN) only the total thickness can be estimated), ^(c) - determined from acoustic measurement, *,** - thickness and material properties fixed during fit)*

Specimen 2, 4 and 6 are used for determining the bulk wave velocity by fitting the thermomechanical model to the results measured with picosecond ultrasound. The other specimen of the same type but with other film thicknesses (specimen 1, 3 and 5) are used for validating the model and the fitted results.

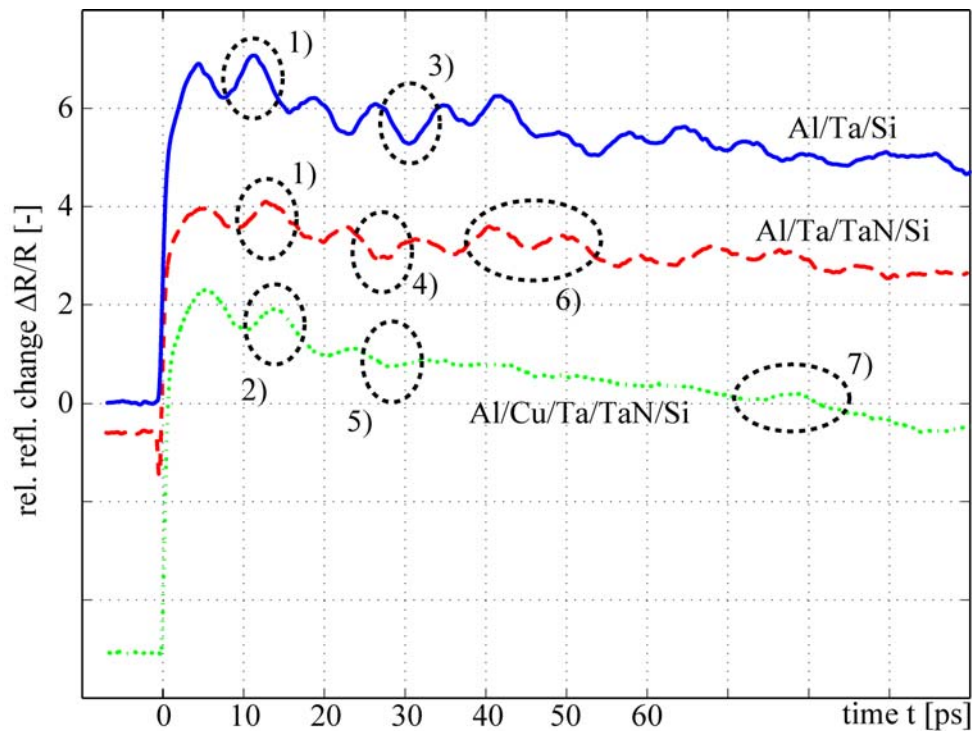


Figure 4.14 Comparison of measurements on the following multilayers: Al/Ta/Si (specimen 1) - solid line, Al/Ta/TaN/Si (specimen 3) - dashed line, Al/Cu/Ta/TaN/Si (specimen 5) - dotted line, the curves are vertically shifted, the identified peaks are caused by reflection at the following interfaces: 1) Al/Ta, 2) Al/Cu, 3) Ta/Si, 4) Al/Ta (second), 5) Al/Cu (second), 6) superimposed reflections of Al/Ta, Ta/TaN, TaN/Si, 7) Cu/Ta

In Figure 4.14 a set of measurements on specimen 1, 3 and 5, all coated with approximately 40nm aluminium are, presented.

The first reflectivity peak of the measurement on the Al/Ta/Si specimen (1, Figure 4.14, solid line) is caused by the reflection of the acoustic pulse at the Al/Ta-interface, but the third and negative peak (3, Figure 4.14) corresponds to the reflection at the Ta/Si interface. The second negative peak (between 1 and 3, Figure 4.14, solid line) corresponds to the second reflection of the acoustic pulse at the Al/Ta interface.

At the beginning the measurement on the Al/Ta/TaN/Si specimen (specimen 3, Figure 4.14 dashed line) has the same characteristics as the measurement on the Al/Ta/Si specimen. The first positive peak (1, Figure 4.14, dashed line) and the following negative peak (4, Figure 4.14, dashed line) are caused by the first and the second reflection at the Al/Ta interface. Acoustic reflections at the Ta/TaN (small acoustic reflection) and at the TaN/Si interface superimpose (6, Figure 4.14, dashed line).

Compared with the previous two measurements the third one on the Al/Cu/Ta/

TaN/Si specimen (specimen 5, Figure 4.14 dotted line) is very different. At the beginning the echoes from the Al/Cu interface (2 and 5, Figure 4.14, dotted line) are observed. The next significant peak in the reflectivity occurs at about 80ps and is assigned to the acoustic reflection at the Cu/Ta interface (7, Figure 4.14, dotted line). Then the acoustic reflections from the Ta/TaN and TaN/Si interface are expected, but the peaks in the reflectivity change are smaller than the previous ones and therefore they can not easily be identified.

Tantalum

With a first measurement on the Al/Ta/Si sample (specimen 2, measurement not shown) the wave velocity inside the tantalum film is determined with the known film thickness. Using the measured thickness of the tantalum film of 71nm the wave velocity is determined as 3987m/s, however with the thickness out of a SEM image (79nm) the wave velocity amounts to 4450m/s. It is obvious, that the determination of the wave velocity depends on the precision of the thickness measurements, which leads to an estimated accuracy of the wave velocity of 10%. This velocity is independently checked with specimen 1 (solid line in Figure 4.14 and Figure 4.15). In general, the two slightly different specimens of each thin film configuration allows a valuable cross check of the determined bulk wave velocity.

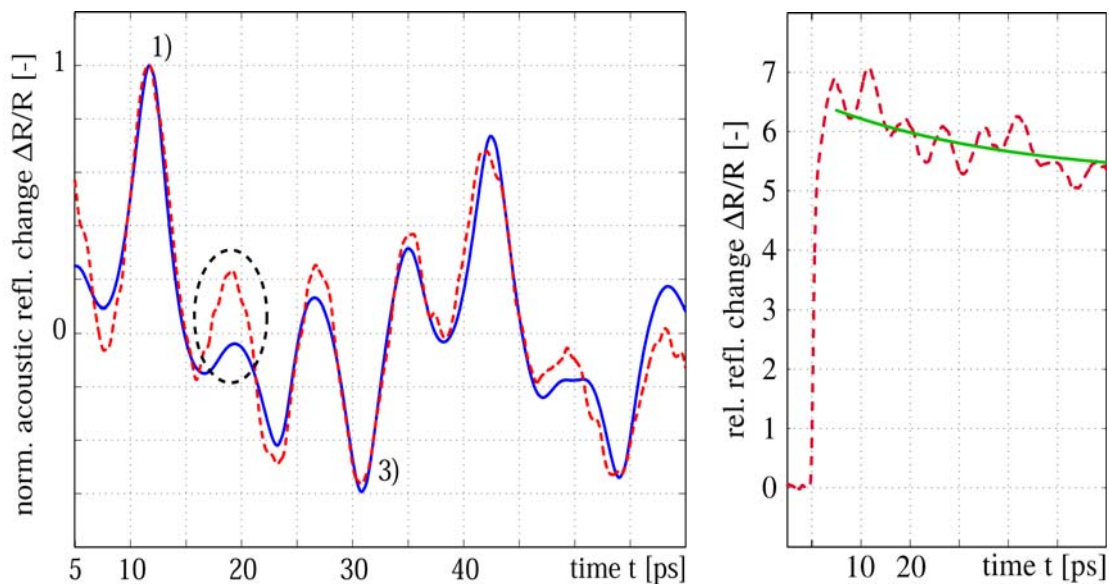


Figure 4.15 Left: simulation (solid line) and measurement without thermal reflectivity change (acoustic reflectivity change, dashed line) of specimen 1 (time scale starts at 5ps); right: average of 10 single measurements (raw data, dashed line) including the thermal reflectivity change (solid line) which is subtracted to give the dashed line left (acoustic reflectivity change)

As mentioned before the first reflectivity peak (1, Al/Ta/Si sample in Figure 4.14 and Figure 4.15 (left)) in the measurement is caused by the reflection of the acoustic pulse at the Al/Ta-interface. The third one (3, Figure 4.14 and Figure 4.15 (left)) is assigned to the reflection at the Ta/Si interface. A comparison of this measurement with the appropriate simulation, calculated with a wave velocity of 3987m/s is presented in Figure 4.15 (left). For comparison of simulation and measurement in Figure 4.15 (left) the reflectivity change caused by the induced temperature change is subtracted from the raw data (Figure 4.15 (right)) and only the acoustic reflectivity change is shown. The determined thickness amounts to 38nm (with 3987m/s) and 44nm (with 4450m/s). Between the first and second reflection of the Al/Ta interface (dashed circle in Figure 4.15 (right)) the difference of predicted and measured reflectivity is significant. Most likely this difference is caused by inaccuracies of thermal properties (tantalum-oxide layer, electron-phonon constant G or thermal conductivity K of aluminium and tantalum) since the other part of the comparison, mainly determined by acoustic properties is in good agreement. Effects of variations in the thermal conductivity for instance are shown in Figure 4.21 (right) in slightly different configuration. The other peaks in the measured reflectivity change are further echoes such as the second acoustic reflection at the Al/Ta interface (second negative peak) or are caused by superposition.

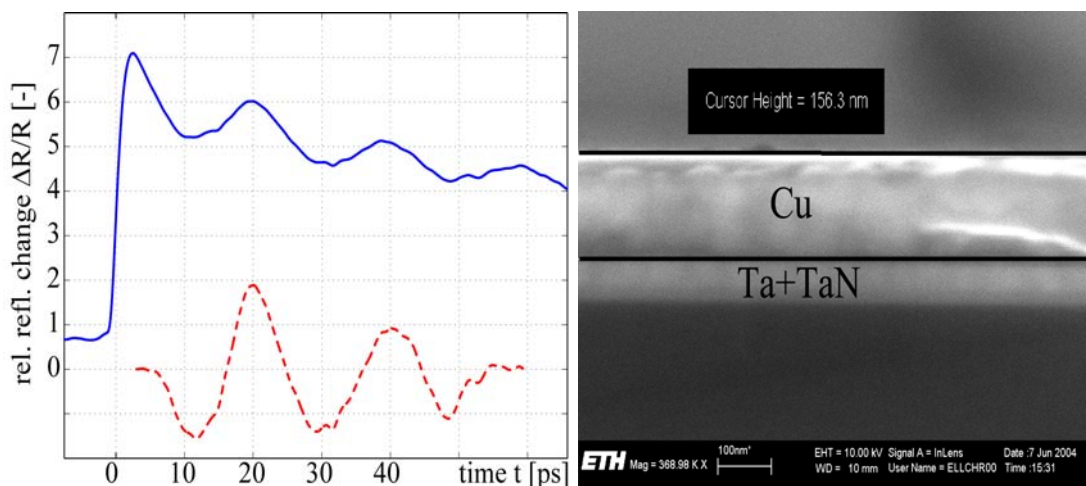


Figure 4.16 Left: measurement of specimen 1 without aluminium top layer, solid line - original measurement (dashed line - acoustic reflectivity change (measurement without thermal decay) and vertically stretched by factor 3); right: SEM image of the cross section of specimen 5

Additionally, Figure 4.16 (left) shows a measurement on the Ta/Si specimen without an aluminium top layer. The photoacoustic response on tantalum at a

wavelength of 800nm is strong enough to get a quite clear signal. Moreover, the optical surface reflectivity is 0.73 and therefore, enough energy is absorbed for launching quite strong acoustic pulses. With the previously determined results the first peak should occur at 19.1ps using the wave velocity of 3987m/s and film thickness of 38nm or 19.8ps with 4450m/s and the corresponding film thickness of 44nm. The nearly sinusoidal oscillations of the reflectivity change is mainly caused by the large optical absorption length of about 18.5nm at a corresponding wavelength of 800nm.

Tantalum-nitride

With the measurements on specimen 4 (Figure 4.17, dashed line) the wave velocity of the underlying tantalum-nitride layer is calculated, using the information of the determined velocity and thickness of the tantalum film. For estimating the bulk wave velocity of tantalum-nitride the procedure is as follows: the measured film thickness (67nm) of the tantalum film of specimen 4 and its determined wave velocity (3987m/s) is kept constant, while varying the wave velocity of the tantalum-nitride film, for assigning the reflectivity peaks to the acoustic reflections they belong. The determined wave velocity is in the order of 5700m/s and the corresponding comparison of measurement and simulation is shown in Figure 4.19.

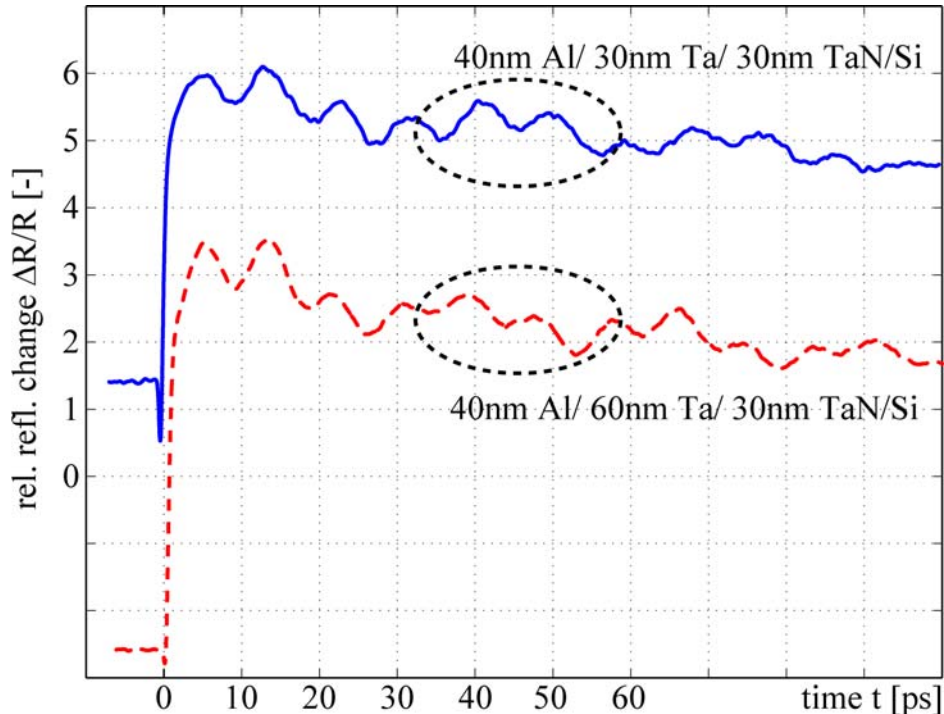


Figure 4.17 Comparison of measurements on specimen 3 and 4 with information on the nominal film thicknesses (curves are vertically shifted)

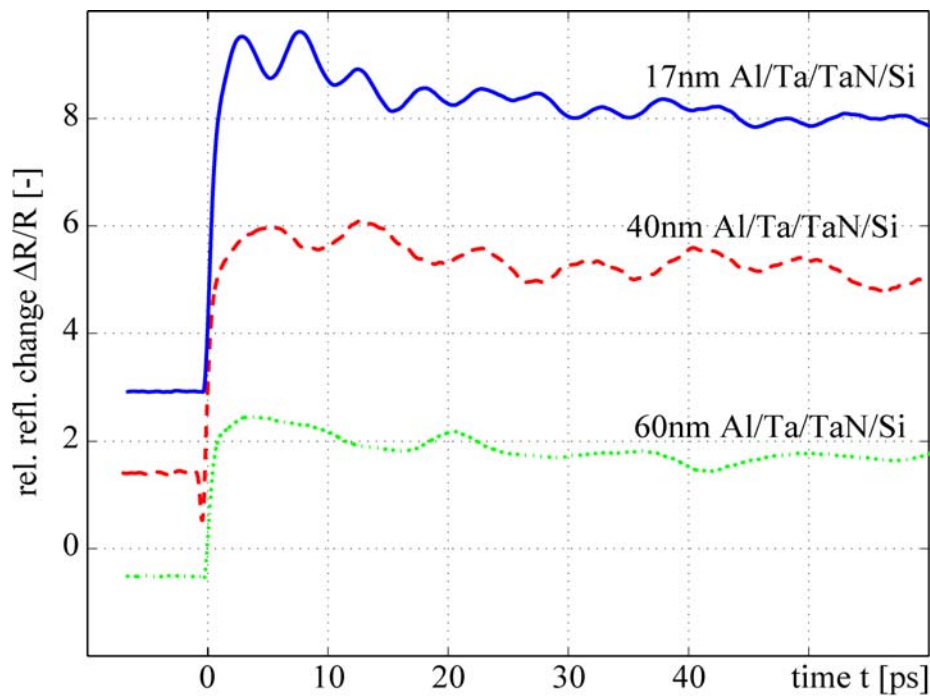


Figure 4.18 Comparison of specimen 3 coated with 3 different aluminium thin films of nominal 17nm, 40nm and 60nm thickness (curves are vertically shifted)

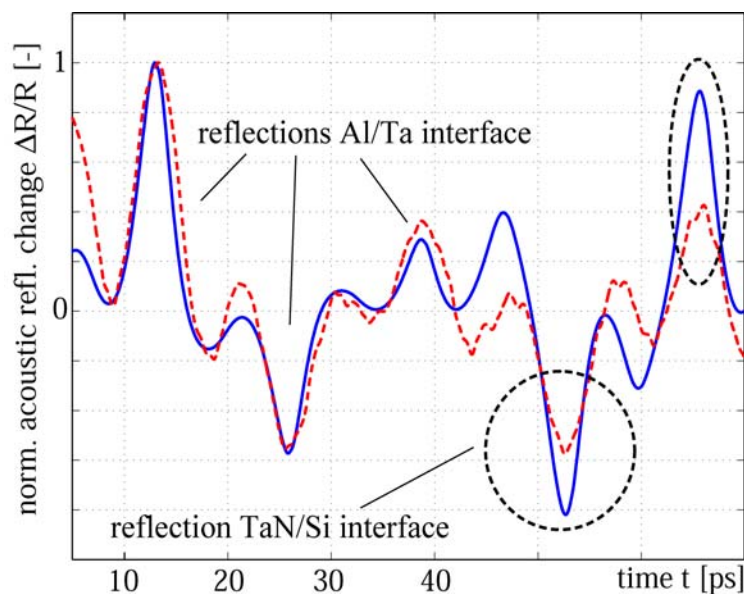


Figure 4.19 Comparison of the measurement (dashed line) and simulation (solid line) of specimen 4 coated with approximately 40nm aluminium

The negative peak marked by the dashed circle corresponds to the acoustic reflection of the TaN/Si interface. The acoustic reflection from the Ta/TaN interface is in the order of 13% (using the determined properties) and further influenced by the transmission coefficient of the Ta/Al interface. Until 40ps the agreement of simulated and measured

results is good, which emphasizes the correctness of the results of the tantalum

film, however, the predicted acoustic echoes of the TaN/Si interface (dashed circle) are much bigger than the measured signals. The reason are manifold: first of all, attenuation in the tantalum nitride film can be a reason, because a significant concentration of argon is detected in the tantalum-nitride film, which might affect the structure. Secondly, also variations of the density (because of the argon) and effects of the interfaces Ta/TaN and TaN/Si are conceivable. For the simultaneous determination of the properties of the tantalum and tantalum-nitride film, also a good match of the amplitudes is essential, since the acoustic contrast of the Ta/TaN interface is small. The estimated velocity of the TaN film is used for the determination of the tantalum-nitride thickness of specimen 3 (measurements in Figure 4.18) using the known properties and thickness of the tantalum film, as mentioned in Table 4.4. The results on the 3 measurements performed on specimen 3, with varying thickness of the aluminium top layer are all in the order of 20nm (17nm Al: 19-20nm, 40nm Al: 21nm, 60nm Al: 19-20nm), which is 10% thicker than the measured thickness. Because the determined wave velocity of TaN depends on the acoustic properties of the tantalum film and other properties, such as the TaN and Ta film thickness the accuracy of the determined wave velocity of TaN can only be estimated, and is in the order of 20-25%. For more reliable and accurate values of the wave velocity of TaN further measurements on single TaN layers are necessary.

Since the measurements on the uncoated Ta/Si specimen presented in Figure 4.16 (left) are very accurate, it is expected that measurements on the uncoated Ta/TaN/Si specimen can provide more reliable data of the TaN film. But until now measurements directly on the Ta/TaN specimen provide no meaningful acoustic results. High resolution images which show the structure of the Ta/TaN specimen can give potentially an answer on this unexpected results.

Copper

With the determined wave velocity of the tantalum and tantalum nitride film the measurements on the specimen with the additional copper film can be discussed. Measurements on specimen 6 lead to a wave velocity of the copper layer of 4770m/s. The third measurement presented in Figure 4.14 (left, dotted line) is performed on an Al/Cu/Ta/TaN/Si-substrate (specimen 5) thin film stack. The reflected acoustic pulse from the Cu/Ta interface is clearly identified at 78.4ps (dashed circle Figure 4.14 (left)) and using the identified acoustic reflection of the Al/Cu interface after 14.5ps, as well as the determined wave velocity of the copper layer, the determined thickness of 153nm is in good agreement with the other measurements and the SEM image presented in

Figure 4.16 (right). Similar as with the Al/Ta/TaN/Si specimens, only the thickness of the tantalum and tantalum-nitride layer together can be determined, because of the small acoustic reflection of the Ta/TaN interface and the mismatch in the measured and simulated amplitudes of the reflectivity peaks corresponding to acoustic reflection of the TaN/Si interface (similar to Figure 4.19). The reasons are the same as with specimen 3 and 4.

In conclusion, the mechanical properties (bulk wave velocity) of Ta, TaN and Cu are determined and validated with the second specimen of each type. It is shown, that properties (thickness or material properties) of a single diffusion barrier layer (Ta) can be determined without further effort. In the case with a bilayer diffusion barrier (Ta and TaN), a further acoustic characterization (attenuation, ...) of the tantalum-nitride layer is necessary to improve the simulations, so that both layers can simultaneously be identified. Below the copper layer the determination of thickness or material properties of the Ta/TaN multilayer is much more challenging even with the aluminium top layer acting as good acoustic transducer.

4.1.3.3.6 Simulations with copper top layer

Due to the lack of an experimental set-up operating with a wavelength of 400nm, the feasibility of the determination of geometrical dimensions of underlying diffusion barriers is discussed, using an accurate numerical model. The induced temperature distribution is calculated using the two-temperature model with the extensions of additional heat flux in the lattice, described in Chapter 4.1.3.3.4. The launched acoustic pulses and the corresponding predominant strain distribution are computed by a numerical solution of the wave equation. The main sequence of the numerical calculations is similar as described in Chapter 2.2.2. The step sizes are chosen as follows

	<i>temporal step size</i>	<i>spatial grid</i>
Temperature simulation	2fs	1nm
Acoustic simulation	10fs	using 'magic time step'

Table 4.5 Temporal and spatial time step

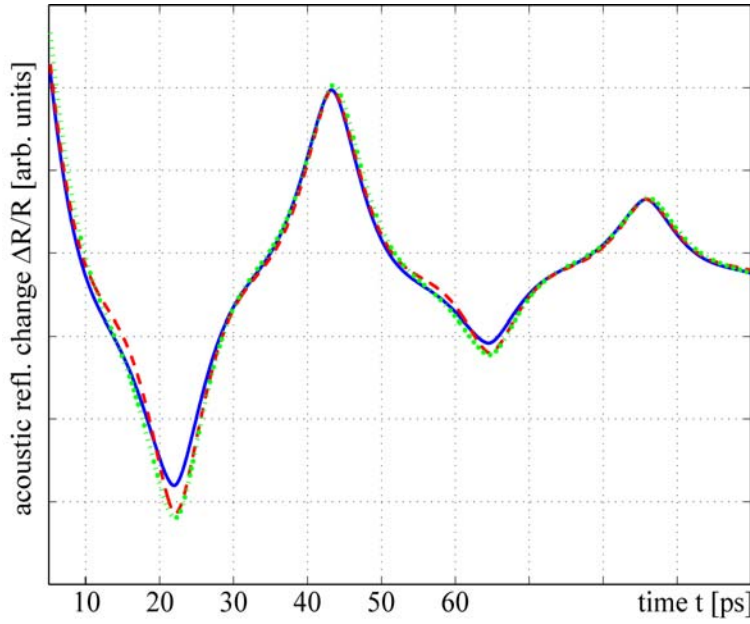


Figure 4.20 Normalized (maximum amplitude) simulations of the acoustic reflectivity change caused by a propagating acoustic pulse in a single 100nm copper film on a silicon substrate (solid line - simulation 1, dashed line - simulation 2, dotted line- simulation 3)

The spatial grid size is chosen as near as possible to a grid size defined by

$$\Delta z = \Delta t c_{max} \quad (4.8)$$

in which c_{max} is the highest bulk wave velocity of all materials in the thin film stack - in this case the bulk wave velocity of silicon (<100> direction), which is about 8500m/s. The step size defined in (4.8) is called magic time step with remarkable properties, such as vanishing numerical dispersion. Details are discussed in

Appendix B.

Copper thin film on silicon substrate

Figure 4.20 shows the acoustic reflectivity change of a propagating acoustic pulse in a 100nm thick copper film on a silicon substrate. The reflectivity change caused by the induced temperature is already subtracted. All material properties are listed in Appendix A.

	$K_{e, eq.}$ [W/(mK)]	K_l [W/(mK)]	Energy flux [J/m ²]
simulation 1	398	398	0.611
simulation 2	398	5	0.611
simulation 3	398	398	6.11

Table 4.6 Properties varied for the simulations presented in Figure 4.20

The heat diffusion in copper, similar as in other noble materials, is very high and additionally, increased by the rather small electron-phonon constant G . As a result, the heat is spread almost over the whole thickness of the thin film on a

very short time scale as it is illustrated in Figure 2.17. This leads to an acoustic pulse excited at the surface and an additional acoustic pulse excited at the interface of the copper thin film and the silicon substrate. One part of the acoustic pulse from the interface is propagating into the substrate, the other towards the free surface and causes the negative reflectivity peak after approximately 20ps. The part initiated at the surface needs twice the time of the one initiated at the Cu/Ta interface to reach the surface again. Since some of the assumed properties, such as the laser spot size, are only approximately known, their influence is discussed. To get significant differences these properties are varied in a wide range. Comparing the normalized simulations 1 (solid line in Figure 4.20) and 3 (dotted line in Figure 4.20) show the difference in the photoacoustic response caused by the much higher induced temperature. The maximum amplitude of each simulated reflectivity change is used for normalizing the simulations in Figure 4.20. The energy flux of the incident pump pulse is in simulation 3 ten times higher than in simulation 1. This leads, because of the temperature dependence of the heat capacity and conductivity in the electron system, to a slightly increased heat flux. Therefore the normalized photoacoustic response caused by the backside acoustic pulse is slightly increased. The absolute photoacoustic signal in simulation 3 is ten times higher than in simulation 1, but it is normalized in Figure 4.20 for comparison. A similar result occurs when the lattice heat conductivity is reduced. Because the heat transport into the substrate is much lower, the temporal varying temperature distribution causes an acoustic pulse with a higher amplitude at the interface. And therefore, the negative reflectivity peaks corresponding to the induced acoustic pulses from the back have again an increased amplitude.

Copper/tantalum on silicon substrate

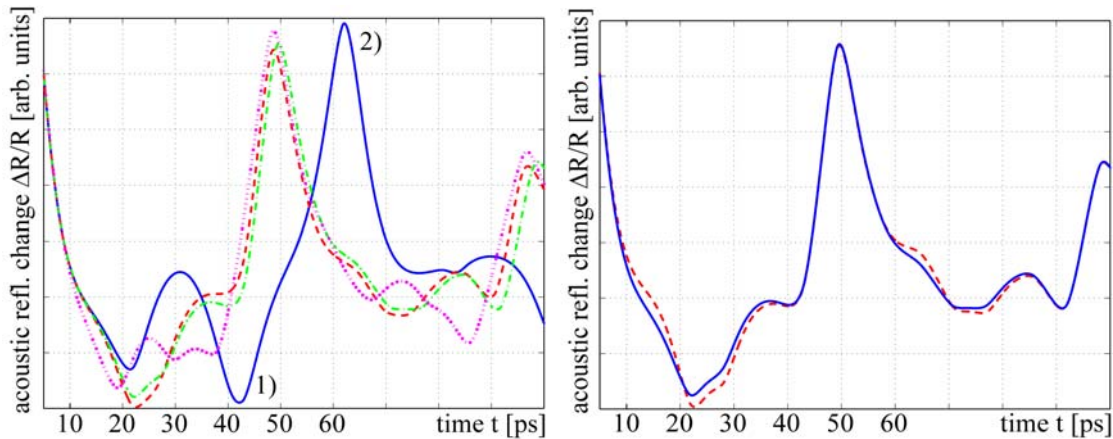


Figure 4.21 Left: normalized simulated acoustic reflectivity change for a Cu/Ta thin film stack on a silicon substrate (solid line - simulation 4, dashed line - simulation 5, dash-dotted line - simulation 6, dotted line- simulation 7), the indicated reflectivity peaks of simulation 4 (solid line) are caused by acoustic reflections at the following interfaces: 1) Cu/Ta, 2) Ta/Si; right: influence of the heat conductivity in the tantalum film (solid line - simulation 6, dashed line - simulation 8)

	Cu. film thickness [nm]	Ta film thickness [nm]
simulation 4	100	36
simulation 5	100	10
simulation 6	100	12
simulation 7	88	20

Table 4.7 Variation of the thickness of the copper and tantalum layer in simulation 4, 5, 6 and 7

Figure 4.21 (left) shows the acoustic reflectivity change of 4 different Cu/Ta thin film stacks, which are described in Table 4.7. For simulation 4 (solid line -Figure 4.21 (left)) the thickness (36nm) of the tantalum thin film below the copper top layer can easily be determined by assigning the different peaks to the corresponding acoustic pulse. The first negative peak is launched at the Cu/Ta interface and the other peaks are superpositions of acoustic waves reflected at the Ta/Si and Cu/Ta interfaces, respectively. According to the results of the three other simulations presented in Figure 4.21 (left), it is obvious that it becomes more difficult to estimate the geometrical dimensions of

the thin films because the several acoustic reflections at the Cu/Ta or Ta/Si overlap already after 20ps. To check if the thickness of the two films can independently be identified in simulation 7, the copper film is only 88nm but the tantalum film thickness is increased and amounts to 20nm. These thicknesses are chosen because the total time of flight of the acoustic pulse from the surface to the Ta/Si interface and back is similar to a 100nm copper and a 10nm tantalum film. So, it can be shown whether the two layers can be resolved independently. The general shape of the photoacoustic response is similar to the one of simulation 5, but with the differences especially between 20ps and 40ps as well as 60ps and 90ps the thicknesses can be estimated by fitting simulated results to the measurements. The modelling must take the very fast spreading of heat and the resulting more complicated acoustic response into account. But the very small differences between simulation 5 and 6 show that the accuracy of the thickness estimation is limited, because a lot of slightly varying properties in the simulation, such as the thermal conductivity, lead to changes in the photoacoustic response, which have the same order of magnitude. This is illustrated in Figure 4.21 (right).

	<i>thin film stack</i>	<i>thermal conductivity of Ta layer [W/(mK)]</i>
simulation 6	100nm Cu/12nm Ta/Si-substrate	57.5
simulation 8	100nm Cu/12nm Ta/Si-substrate	7.1

Table 4.8 Properties varied (thermal conductivity of the Ta layer) of the simulations presented in Figure 4.21 (left)

All the material properties used and their sources are listed in Appendix A.

Copper/tantalum/tantalum-nitride on silicon substrate

Apart from a single tantalum layer, also tantalum-nitride (TaN), tungsten-nitride (WN) and tantalum/tantalum-nitride multilayers are suitable candidates for diffusion barriers below copper films - as mentioned above. For single tantalum-nitride or tungsten-nitride layers the limitations are similar to the tantalum layer. Hence, they are not discussed in detail. In this section we discuss the possibility for resolving the dimensions of the tantalum/tantalum-nitride diffusion barriers, which seems to be even more challenging than a single layer.

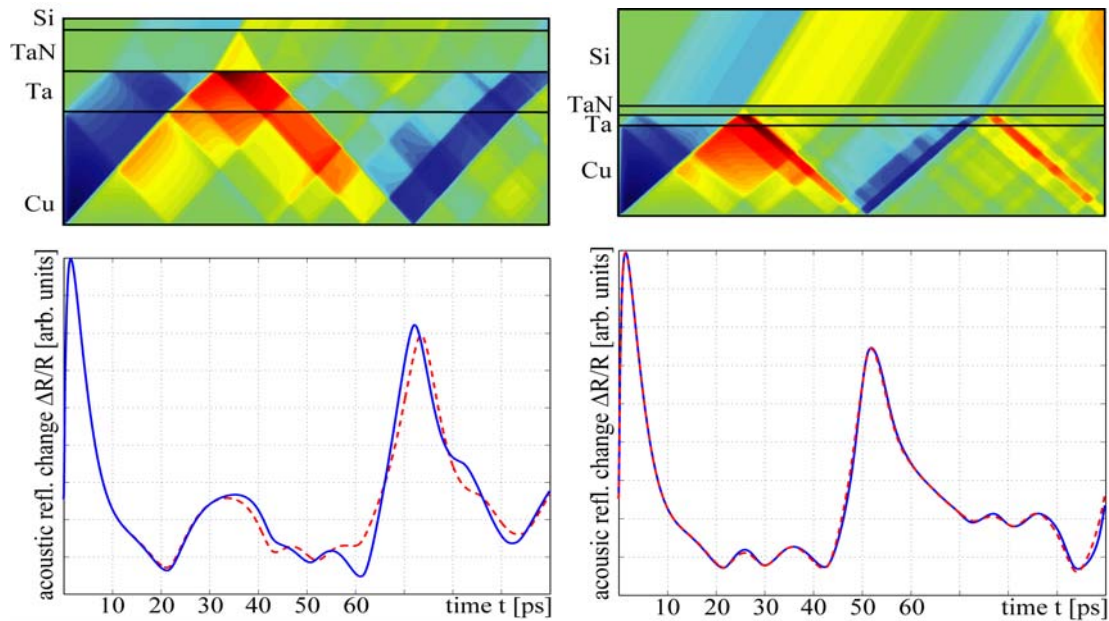


Figure 4.22 Acoustic reflectivity change calculated with simulation 10 (left) and 9 (right) according to Table 4.9; solid line - with properties of Appendix A, dashed line - also with properties of Appendix A except the wave velocities, which are experimentally determined in Chapter 4.1.3.3.5; the illustrations above shows the path of the propagating acoustic pulse (simulation 10 and 9, solid lines) with respect to time and thickness

Simulation 9 in Figure 4.22 (left) using a rather thick bilayer diffusion barrier shows that in this case the dimensions of the layers can be identified by assigning the peaks to the appropriate travelling distance in the different materials. If not mentioned, all material properties are according to Appendix A.

	<i>copper</i> <i>thickness [nm]</i>	<i>tantalum</i> <i>thickness [nm]</i>	<i>tantalum-nitride</i> <i>thickness [nm]</i>
simulation 9	100	10	10
simulation 10	100	36	36
simulation 11	100	12	10
simulation 12	100	10	12

Table 4.9 Properties varied in simulation 9, 10, 11 and 12

The illustration above the calculated reflectivity change in Figure 4.22 shows the path of the propagating acoustic pulses with their reflections (in time-

thickness plane). With the first peaks in the reflectivity change, the geometrical dimension of the layers can be identified, although, except for the first peak, all following negative peaks overlap, so that also in this case an accurate model gets necessary. The effect can be observed in comparing the path of the acoustic pulse with the corresponding reflectivity change. The assignment of the reflectivity peaks to the corresponding acoustic reflections in simulation 8 is limited by the fact that several reflections at the interfaces are superimposed. The dashed lines in Figure 4.22 represent calculations with the same film thickness and also the same material properties (Appendix A), except for the bulk acoustic wave velocity, which is modified according to the measured values (Chapter 4.1.3.3.5). Significant changes can only be observed in simulation 9 corresponding to the rather thick bilayer diffusion barrier (36nm Ta, 36nm TaN).

If the time of flight of the acoustic pulse in the tantalum-nitride is in the same order of magnitude as the time the acoustic pulse needs to cover the absorption length right at the free surface of the copper film, the determination of the thickness with an acceptable accuracy becomes challenging.

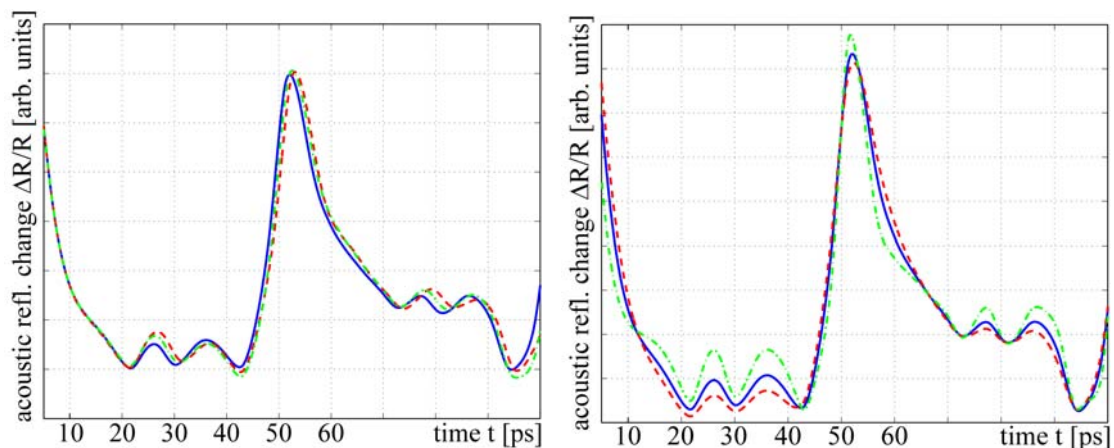


Figure 4.23 Left: acoustic reflectivity change of simulation 8 (solid line), 10 (dashed line) and 11 (dash-dotted line; right: acoustic reflectivity change of simulation 8 caused by different absorption length in the modelling of the detection (14.4nm - solid line, 18nm - dashed line, 10nm - dash-dotted-line)

The three simulations in Figure 4.23 (left) illustrate the small variations, which must be sufficient to determine the thickness of these diffusion barrier layers. But it emphasizes also that after multiple reflections small variations in the time of flight occur (at 80ps) which can possibly be used for limited thickness estimation. The detection is modelled with the theory described in Chapter 2.4 using the a calculated absorption length of 14.4nm for copper at 800nm. Figure 4.23 (right) shows the effect of a larger absorption length of 18nm and a smaller one of 10nm using the same strain distribution.

4.1.3.3.7 Discussion

This qualitative analysis indicates the limitations for the determination of the layer thickness, if the underlying barrier layers become very thin. The main limiting factors are on the one hand, the increased heat transport in the copper layer and on the other hand, the larger absorption length, which is the double of aluminium and limits the detectability of very high frequencies. However, a series of experiments on copper using a modified experimental setup working with 400nm optical wavelength, would provide also information about properties, which are disregarded in the simulation, such as the attenuation of the travelling acoustic pulses.

4.2 Measurements on transparent materials

Measurements of the wave propagation in transparent materials enable the determination of the bulk wave velocity. The presented measurement technique is performed with the setup according to Figure 3.19. A measurement on aluminium coated transparent borosilicate glass (Pyrex, Corning 7740) is presented. Using this measurement configuration (probing through a transparent substrate) oscillations in the reflectivity change caused by interferences in the transparent media are expected from theory (Chapter 2.4). The measurement shows these oscillations very well and fits with the frequency predicted by theory. Similar work, but with other materials or measurement configurations, respectively, has been done by Lin H.-R. et.al. [34] and with transparent thin films by Wright O.B. [90] [93].

4.2.1 Specimen

The specimen of this investigation is a borosilicate glass (Pyrex, Corning 7740) coated with a 100nm aluminium thin film. It is the same specimen as used in Chapter 4.1.1.3, but the measurements are performed in a different configuration (Figure 3.19). The borosilicate glass (Pyrex, Corning 7740) has the following material properties

		<i>Source</i>
Density [kg/m ³]	2230	[56]
Young's modulus [GPa]	62.75	[56]
Poisson ratio	0.2	[56]
Thermal expansion coefficient (at 25°C) [1/K]	3.266 10 ⁻⁶	[56]

Table 4.10 Material properties of borosilicate glass (Pyrex, Corning 7740)

		<i>Source</i>
Thermal conductivity (at 25°C) [W/(m K)]	1.13	[57]
Specific heat [J/(kg K)]	754.2	[57]
Refractive index at 800nm (estimation)	1.4657	[57]
Acoustic reflection coefficient (Al/Glass 7740)	-0.1588	

Table 4.10 Material properties of borosilicate glass (Pyrex, Corning 7740)

The 100nm aluminium coating is deposited under the conditions mentioned in Chapter 4.1.1.1.

4.2.2 Measurements and Discussion

The experimental setup used for the measurement presented in Figure 4.24 is modified in a way that the probe and the pump laser pulses hit the specimen from opposite sides (Figure 3.19). Both laser pulses are focussed with microscope objectives towards the specimen. The acoustic pulses are excited on the free surface of the aluminium film - the reflectivity is measured through the transparent substrate. As described in Chapter 2.4 the reflectivity is affected by reflectivity changes of the aluminium film caused by the induced temperature and the excited strain pulse. Additionally, it is modulated by reflections of the laser pulse on the propagating strain pulse in the transparent substrate. Since the thermal conductivity of the borosilicate glass is very small in the order of 1.13W/(m K), it can be assumed that the calculated temperature distribution in Figure 4.7 is similar to the one in this case. Thus, Figure 4.7 shows the temporal temperature distribution at the interface of aluminium and glass substrate after the absorption of the laser pulse at the free surface.

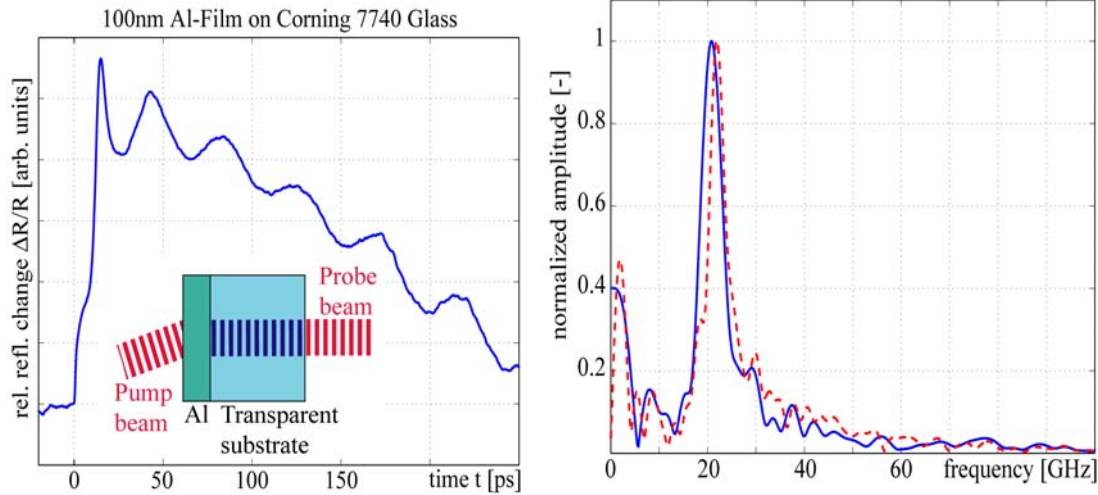


Figure 4.24 Left: reflectivity measurement according to the configuration in the inset (average of 30 single measurements using pump pulse power of 20mW) on a transparent glass substrate coated with approximately 100nm aluminium; right: fast fourier transform of the measurement left (solid line - reflectivity change from 150ps to 450ps is considered, dashed line - total measurement)

The temperature at the interface increases shortly after the absorption of the pump laser pulse at the free surface because of the non-equilibrium short-pulse laser heating. Therefore, the measured reflectivity, which is proportional to the temperature, increases shortly after absorption. Before the reflectivity decreases smoothly, it increases further within the first 30ps. The first peak of the reflectivity curve at approximately 16ps corresponds to the acoustic pulse, which is reaching the interface of aluminium and glass. Most of the acoustic pulse is transmitted into the glass because the acoustic reflection coefficient is about 15%. In the transparent substrate the incident probe laser light is reflected at the interface of aluminium and borosilicate glass and at the propagating acoustic pulse, which leads to interferences. These interferences occur in the reflectivity signal as sinusoidal variation of the reflectivity superimposed on the thermal reflectivity change. The bulk wave velocity of the acoustic pulse in the substrate can be determined with the frequency of the interferences of about 21GHz. Additionally, the frequency of the interference depends on the optical wavelength in the substrate, which again depends on the optical refractive index. The frequency of the oscillations leads to the bulk wave velocity using the following equation

$$c_I = \frac{\lambda f}{2} \quad (4.9)$$

in which λ denotes the wavelength inside the substrate and f the frequency of the oscillations. The frequency was calculated by fast fourier transformation of the reflectivity curve between 150ps and 450ps, because the first part of the measured reflectivity signal contains additionally the second and third acoustic reflection of the pulse in the aluminium film. The determined frequency of the oscillations amounts to 20.8GHz (Figure 4.24 (right), solid line). With a probe light wavelength of 800nm and the refractive index of Table 4.10 this leads to a bulk wave velocity of 5676m/s. The calculated wave velocity is 5592m/s (calculated with the parameters given in literature (Table 4.10)) and is very close to the measured one. The relative error is only about 1.5%.

4.3 Bulk wave propagation in membranes

Very thin membranes are part of numerous micro-electromechanical systems (MEMS), e.g. sensors, actuators or bulk acoustic wave filters. Usually, the mechanical properties of the membranes are important parameters for the correct operation of the MEMS device. Manufacturing processes and conditions significantly influence the resulting mechanical properties of a microstructure, which will be shown in the example of silicon nitride. After finishing of the manufacturing process of MEMS it is very difficult to measure any material property in a non-destructive way with the conventional methods. Picosecond ultrasound is the right approach for providing mechanical properties of thin and brittle MEMS-structures, such as cantilevers and membranes in a non-contact and non-destructive way.

Since nearly no work has been done for microstructures except by Matsuda O. et.al. [39] who recently published also one paper on this subject (GaAs bridge), the following two chapters deals with the application of picosecond ultrasound for the characterization of microstructures such as membranes, cantilevers and truncated micro-tips.

4.3.1 Specimen

The specimen of this investigation is a silicon nitride (Si_3N_4) membrane which is coated with aluminium films of different thicknesses according to Figure 4.25. The aluminium films are deposited by electron beam evaporation (see Chapter 4.1.1.1).

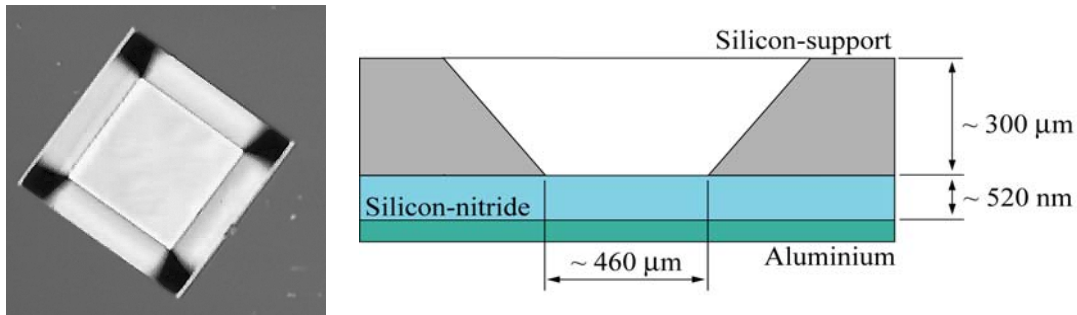


Figure 4.25 Silicon nitride membrane with surrounding silicon support (left: top view under microscope, right: schematic cross-section)

The commercially available silicon nitride (Si_3N_4) membrane shown in Figure 4.25 has a surrounding silicon support of 300 microns thickness. The dimensions of the freestanding membrane are 460 microns squared. The thickness of the membrane is in the order of 520nm and is measured by means of a profilometer. The silicon nitride membrane has an amorphous structure and is grown by an LPCVD process at about 700°C. The Young's modulus of silicon nitride varies in a wide range depending on the conditions of deposition. Some literature values of the Young's modulus are shown in Figure 4.26. The highest value (Hälg B. [21]), which lies in the order of 380GPa, is nearly three times higher than the value of sputtered silicon nitride thin films given by Petersen K.E. [52]. The numbers of the Young's moduli of films deposited by LPCVD (Tabata O. et. al. [75]) and PECVD (Tabata O. et. al. [75]) are in between.

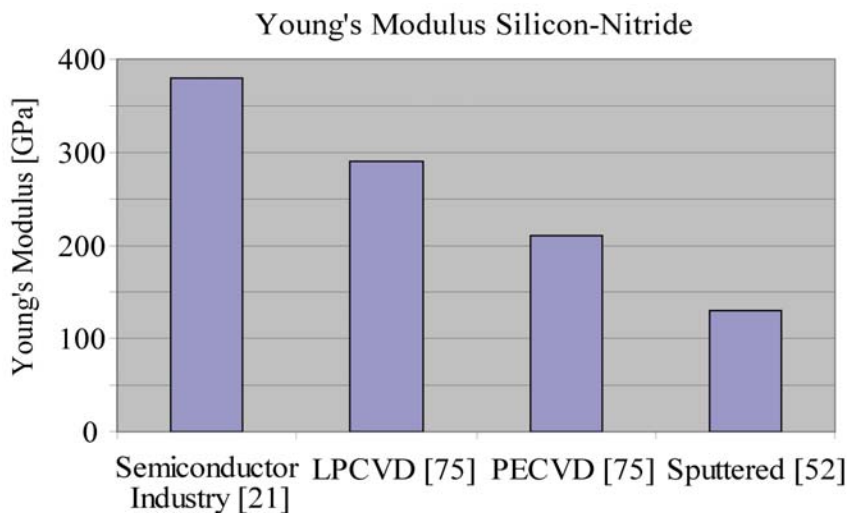


Figure 4.26 Comparison of the Young's modulus of silicon nitride films grown with different techniques.

The specimens used are described in Figure 4.25. They are coated with aluminium films of different thicknesses. The aluminium films are deposited by electron beam evaporation. The thickness of the deposited films ranges from 10nm to 120nm. The measurements with laser based ultrasound are performed directly on the membrane and for comparison beside the membrane on the supported part.

4.3.2 Measurements and Discussion

The silicon-nitride layer is nearly transparent for the laser light at a wavelength of 800nm. So, all specimens are coated with aluminium films having different thicknesses to launch acoustic pulses. In the first section, measurements on silicon nitride films coated with 10nm aluminium are reported. Results presented below are measured on a silicon nitride membrane coated with a 120nm aluminium thin film. The measurements are performed in different configurations as shown in the Figure 4.27 and Figure 4.28.

4.3.2.1 Measurements on supported membranes coated with 10nm aluminium

The specimen, which is shown schematically in Figure 4.27 (left), is coated with a 10nm thick aluminium layer. The incident pump pulse is partly absorbed by the semitransparent 10nm aluminium thin film. The absorption of the pump laser pulse initiates an instantaneous heating of the very thin aluminium coating. The temperature distribution is nearly uniform in the thickness direction. Usually, the initiated temperature decreases exponentially with increasing thickness (compare Figure 2.2). But due to the very small thickness of the aluminium layer, which is in the order of the absorption length, the temperature distribution can be assumed to be uniform. The sudden increase at a time of 0ps and the slow decrease of the measured reflectivity change shown in Figure 4.27 (right), is caused by the induced temperature change in the thin aluminium film.

The increased temperature in the aluminium thin film launches acoustic pulses, which are reflected several times at the interface of aluminium and silicon nitride and at the free surface of the aluminium thin film, respectively. This leads to a decaying oscillation at the beginning of the measured reflectivity change within the first 15ps. The launched acoustic pulse is travelling in the silicon nitride film towards the interface of silicon nitride and the silicon support. Only a small fraction of the acoustic pulse is reflected at the interface. The other part is transmitted into the silicon support. After a round trip time in the order of 105ps, the reflected acoustic pulse is detected back at the surface of the thin aluminium film. The oscillating characteristic of the reflected

acoustic pulse is still present after one reflection. After half of the round trip time in the order of 52ps a small peak in the measured reflectivity change can be observed. Most likely, the small peak is caused by an acoustic pulse, which is excited by the transmitted part of the pump laser pulse, which is absorbed at the interface of silicon nitride and silicon substrate. Travelling from the interface towards the free aluminium coated surface, the pulse can be detected exactly after half the round trip time.

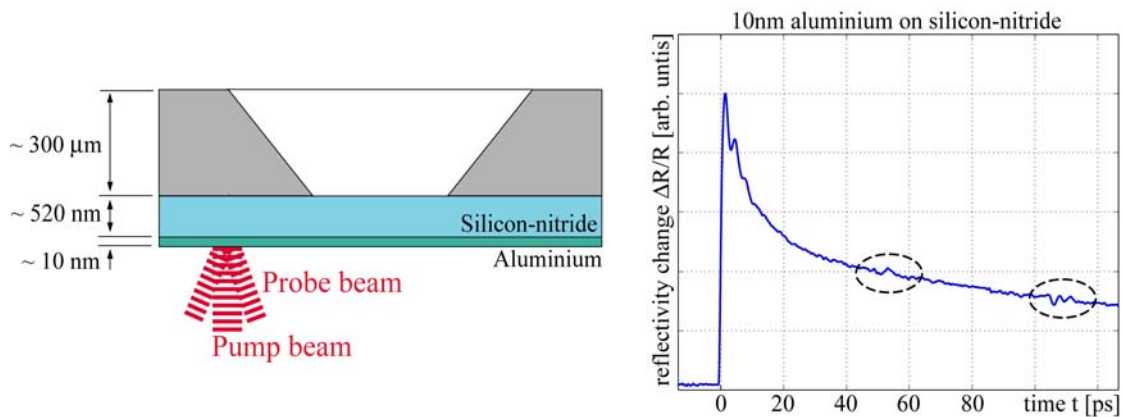


Figure 4.27 Left: measurement configuration; right: measured reflectivity change

4.3.2.2 Measurements on a free silicon-nitride membrane coated with 120nm aluminium

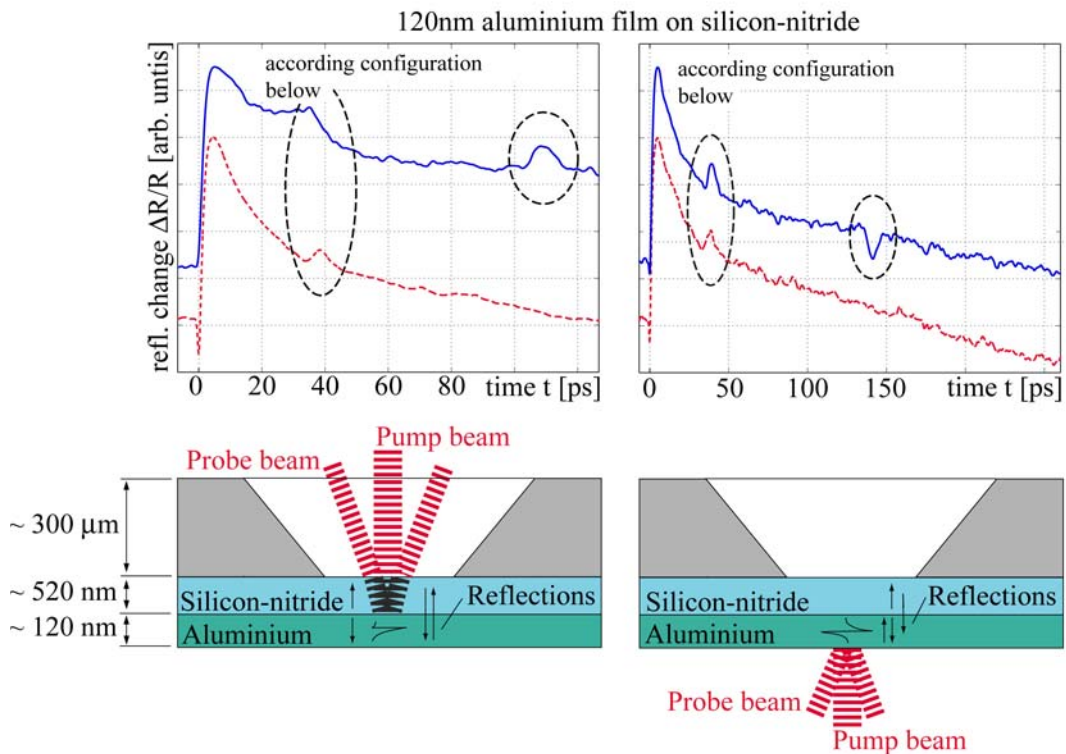


Figure 4.28 Bottom: measurement configurations; top: measured reflectivity change (solid line - measurements with configurations indicated below, dashed line - measurements on the silicon supported part of the membrane accessed from the stress free aluminium surface)

The excitation and detection of the acoustic pulses of the measurement according to Figure 4.28 (left) is performed through the nearly transparent silicon-nitride membrane. At the interface of the aluminium and the silicon-nitride membrane the incident pump pulses are absorbed, initiate a temperature distribution in the membrane and launch acoustic pulses into the silicon-nitride and the aluminium part of the membrane, as schematically indicated with the arrows in Figure 4.28 (left) on the left hand side. Each mechanical pulse is reflected at the free surface of the aluminium and the silicon-nitride part of the membrane, respectively. The corresponding reflectivity change is also measured at the interface by the probe laser pulses, as shown in Figure 4.28 (left) - solid curve. After 39ps the reflected mechanical pulse in the aluminium part reaches the interface, which corresponds with the beginning of a sharp decrease in the measurement. This steplike decrease is a superposition of different effects, which are discussed in detail in Chapter 2.4. The decrease at 39ps in the solid curve of Figure 4.28 (left) corresponds to the peak (first

reflection) in the dashed curve. The dashed curve represents the reflectivity change excited and measured at the free surface of the aluminium coating (backside of the aluminium coating) on the supported part of the membrane. A second reflection of the mechanical pulse in the aluminium coating cannot be clearly identified. The acoustic pulse launched in the silicon-nitride film reaches the interface after 105ps and causes a broad peak in the reflectivity change (solid curve).

The solid curve in Figure 4.28 (right) represents a measurement, which is carried out on the same specimen as the measurements described before, but the specimen is accessed from the other side (aluminium coating). As usual, the absorbed pump pulse initiates a temperature distribution in the membrane and excites mechanical pulses travelling according to the arrows in Figure 4.28 (right). The first reflection, which can be observed again at 39ps, is caused by the acoustic pulse reflected at the aluminium/silicon-nitride interface. This peak can also be observed in the dashed curve, which is measured on the supported part of the membrane. The second reflection of the acoustic bulk wave at the interface cannot be clearly identified in the measurement. After 142ps a negative peak in the reflectivity change is observed, which corresponds to the acoustic pulse reflected at the free surface of the silicon nitride part of the membrane. The sign change occurs at the free surface of the silicon nitride film. Due to the calculated acoustic reflectivity coefficients the negative reflectivity peak should have a higher amplitude than the first, positive peak. Reasons for the reduction of the peak amplitude are damping and a not ideal bonding of aluminium and silicon nitride, which results in modified acoustic reflectance and transmission coefficients. In the supported case, the second peak does not occur, because of the weaker acoustic reflection at the silicon-nitride and silicon interface, compared with the strong reflection at the free surface in the freestanding membrane.

4.3.2.3 Comparison of measured and simulated results of a membrane coated with 40nm aluminium

In order to compare measurements and theory, simulations are performed for a 40nm aluminium coating on the membrane. According to Chapter 2.2.3 and Chapter 4.1.3.3 a coupled numerical scheme for the induced temperature in the membrane and the bulk wave propagation is used for the simulations. The simulated reflectivity change (Figure 4.29) of the silicon-nitride membrane coated with 40nm aluminium is in good agreement with the measured results. The propagation of the bulk waves is similar to the configuration in Figure 4.28 (right). The first reflection of the wave in the aluminium can be observed after approximately 13ps. The negative peak at 117ps is caused by the wave

reflected at the free end of the silicon-nitride surface. And again after 13ps this wave reaches the free aluminium surface a second time, after the reflection at the interface of aluminium and silicon-nitride.

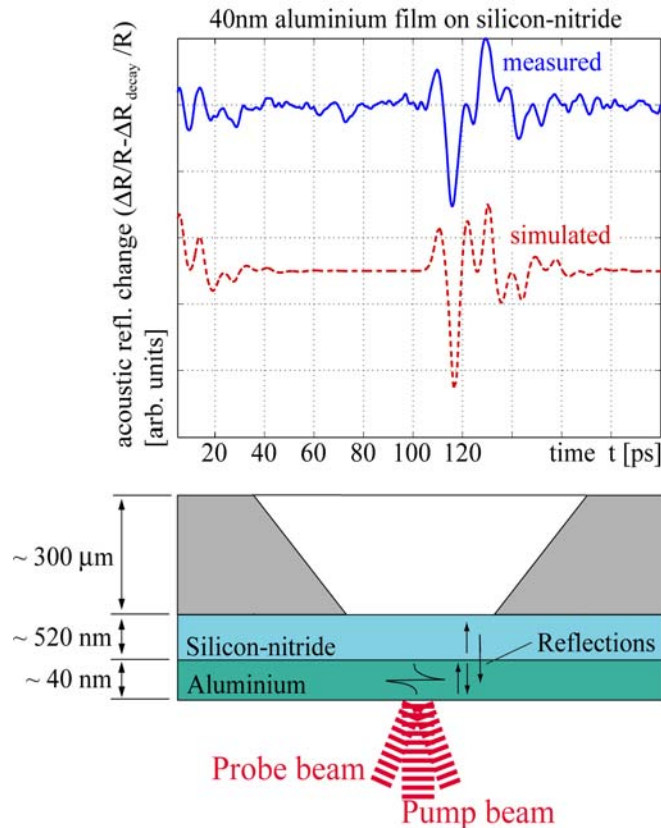


Figure 4.29 Bottom: measurement configurations; top: measured reflectivity change (using the configuration indicated below, solid line - measured results, dashed line - simulated results)

4.3.2.4 Summary of the measured results

With the presented results in Chapter 4.1.3.1, Chapter 4.3.2.2 and Chapter 4.3.2.3 and the known thickness of the aluminium and silicon nitride membrane the bulk wave velocity is determined. The average of the thickness of the membranes amounts to 520nm and the average of the round trip time in the silicon-nitride membrane is 104ps, which leads to a bulk wave velocity of 10^4 m/s . To estimate the Young's modulus of the silicon-nitride membrane, a density ρ of 3100 g/cm^3 (source Petersen K.E. [52]) and a Poisson's ratio ν of 0.24 (source Shackelford J.F. et. al. [70]) is chosen. The calculated value of the Young's modulus of 263GPa is 10% lower than the modulus given in Figure 4.26 for LPCVD silicon-nitride membranes. Nanoindentation measurements on the supported part of the silicon nitride membrane however, are in good agreement with the Young's modulus determined here. Inaccuracies of

the estimated number of the Young's modulus are caused by the measurement of the thickness; a change in thickness of 10nm and the same numbers for all other parameters leads to a change in the Young's modulus of 10GPa. Investigations on silicon nitride cantilevers recently presented by Khan A. et. al. [29] report about a Young's modulus of amorphous silicon nitride of 280GPa and 289GPa, respectively. A Poisson's ratio ν of 0.2 was estimated. With a Poisson's ratio ν of 0.2 [48] our measurements also yield a Young's modulus of 280GPa. Since the measured property is the bulk wave velocity it is important to know that the calculated Young's modulus depends on the used density and Poisson's ratio. Therefore they are given in this chapter and also in Appendix A.

4.4 Measurements on cantilevers and AFM tips

Most applications of the presented measurement technique deal with the characterization of single thin films and thin film stacks deposited on substrates. This chapter deals with a new application of picosecond ultrasound for the characterization of single microstructure such as membranes or cantilevers. In the previous chapter microstructured membranes were non-destructively characterized by picosecond ultrasound. The technique is now extended to the characterization of cantilevers. Cantilevers are, aside from membranes, one of the most used MEMS-structures. In several different applications the mechanical properties or the geometrical dimension of the cantilever are important for the correct working of a device (AFM for instance).

For silicon cantilevers a strong dependency of the measured reflectivity change on the optical probe wavelength is observed in the experiments. This dependency and possible applications are also discussed in this chapter.

4.4.1 Cantilevers

Picosecond ultrasound is generated and measured with ultrashort laser pulses in a pump-probe configuration. In this case, the measured bulk acoustic wave propagation is used for the determination of material properties or geometrical dimensions of a single cantilever. The acoustic pulses are launched at the aluminium coating of the cantilever by absorbing the pump laser pulses. With the probe laser pulses the reflectivity on the opposite side of the cantilever is scanned versus time.

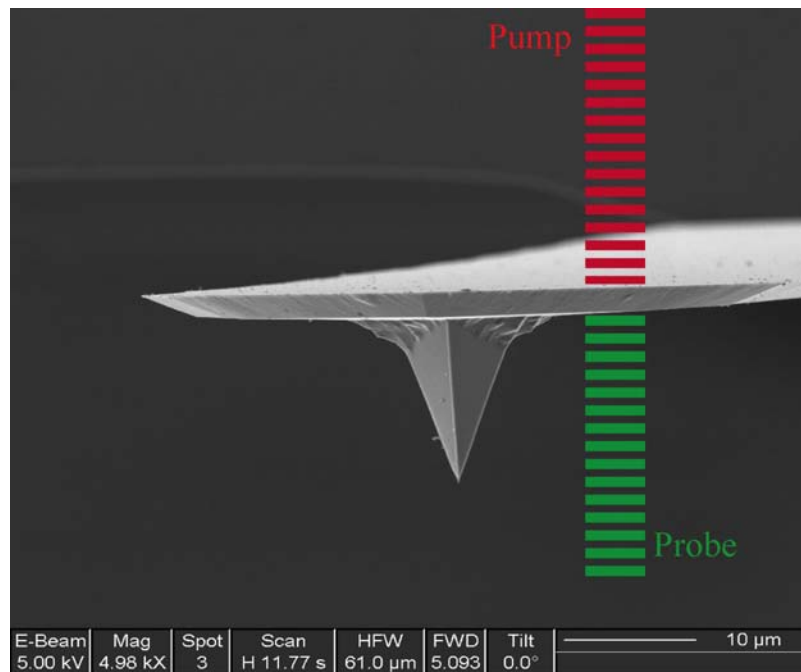


Figure 4.30 Schematic illustration of the measurement configuration, pumping on the aluminium coated side, probing on opposite side

The commercially available cantilevers (Nanosensors CONTR-16 with reflex coating), which are usually used for AFMs (atomic force microscope) (Figure 4.30) have typical thicknesses of $2\mu\text{m}$ and mean widths of $50\mu\text{m}$. The cantilever length is in the order of $450\mu\text{m}$. The silicon cantilever is coated on one side with a very thin, approximately 30nm thick, aluminium film (reflex coating). The tip is on the opposite side, which is not coated and is oriented in the $\langle 100 \rangle$ direction. The silicon is boron doped.

Double-side aluminium coated cantilever

The following measurement is performed on the described AFM cantilever, which has an additional aluminium coating (approximately 30nm thickness, deposited with e-beam evaporation according to Chapter 4.1.1.1) on the side of the incident probe pulse. The measurement configuration is illustrated in Figure 4.30. The acoustic pulses are launched at the free surface of the aluminium coating on the pumping side by absorbing the incident laser pulses. The propagating strain pulse has a similar shape, as presented in Figure 2.3. But the shape is affected by the electron diffusion (see Figure 2.16) and the small thickness of the aluminium coating of about 30nm . The acoustic pulses launched at the free surface of the aluminium coating are almost completely transmitted into the silicon cantilever, since the acoustic reflection coefficient is in the order of only 6% for the combination of aluminium and silicon in

<100> direction. After propagating through the cantilever, the acoustic pulses are detected by the probe laser pulses on the opposite side of the cantilever. On the opposite side the majority of the acoustic pulse is again transmitted from the silicon cantilever into the aluminium coating. The arriving acoustic pulse leads to the peak in the reflectivity at about 258ps in Figure 4.31 (right).

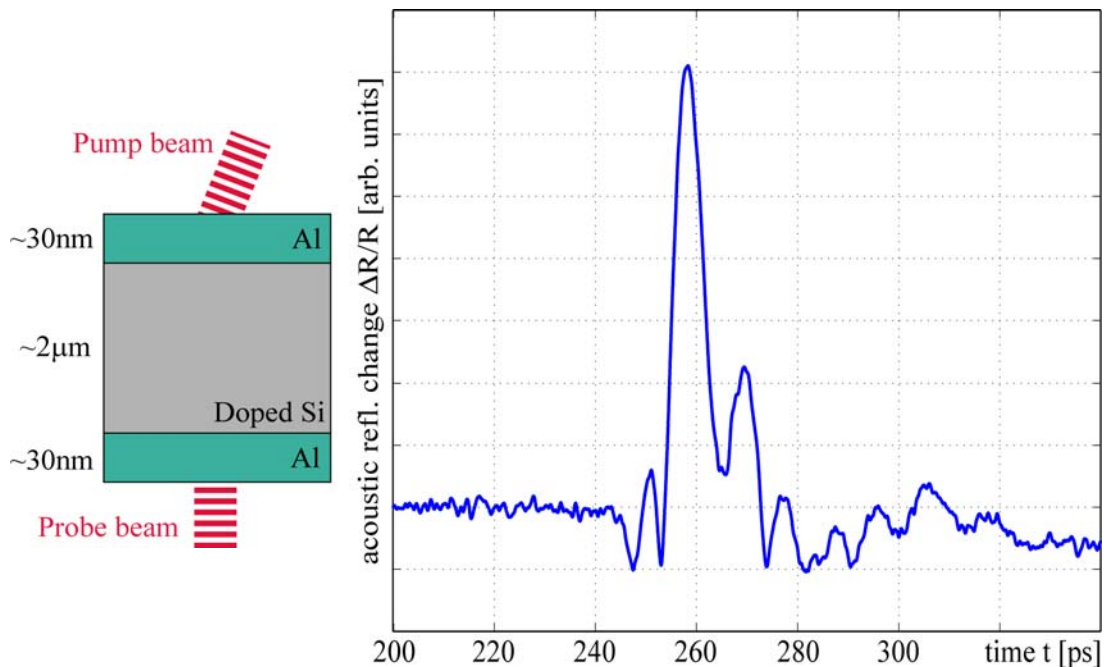


Figure 4.31 Left: illustration of the measurement configuration; right: measured acoustic reflectivity change of the propagating mechanical pulse

The measurement presented in Figure 4.31 is carried out on the freestanding part of the cantilever near to the mounting chip at a laser wavelength of about 800nm. The pump pulses have an average power of ~10mW and the probe pulses are much weaker and in the order of ~2mW. The smaller reflectivity peaks after the main peak at 258ps are caused by the acoustic reflections at the interface of the excitation and detection aluminium layer. In addition, the thermal diffusion during excitation and the excitation of an acoustic pulse also at the Al/Si-interface affect the detected pulse shape.

One-side aluminium coated cantilever

The acoustic pulses are again launched at the free surface of the aluminium coating by absorbing the incident pump laser pulses. The detection is performed on the opposite side of the cantilever (boron doped silicon) and leads to the peak in the reflectivity at about 240ps in Figure 4.32. The measurement presented in Figure 4.32 is carried out in the described configuration on a freestanding part of the cantilever in the region near the mounting chip at a wavelength of 794nm. To get a good signal to noise ratio and to work with low laser

power to avoid damage of the cantilever, microscope objectives are used to focus pump and probe pulses towards the specimen. Thus, the focal spot size is in the order of some microns. On the one hand, the reflectivity change during the first 40ps strongly depends on the geometrical overlapping of pump and probe laser spots.

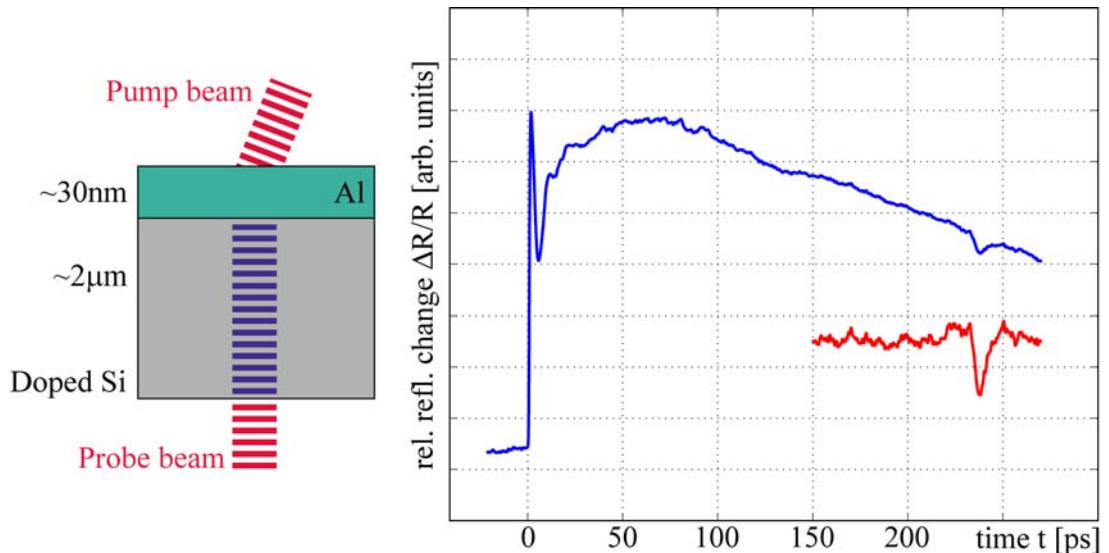


Figure 4.32 Left: Illustration of the measurement configuration; right: measured reflectivity change of the acoustic pulse

On the other hand, the relative reflectivity change after approximately 40ps shows always the same characteristic. The presented results are only averaged 10 times, which takes only few minutes. The acoustic pulse reaching the free silicon surface of the cantilever can be clearly identified after 237ps. For more clearness, the inset in Figure 4.32 shows the part of the measurement from 150ps to 270ps after subtraction of the thermal reflectivity change and vertical zoom of four times.

If one is changing the thickness of the cantilever or the wavelength of the used laser, it has a significant influence on the peak height of the reflectivity change caused by the acoustic pulse. Changing the wavelength from 814nm to 794nm the peak in the reflectivity is constantly changing from a positive to negative a sign. The reason is that the absorption length of silicon at a wavelength of 800nm is in the order of 10 microns at room temperature. This means that the silicon part of the cantilever is almost transparent. Also, Bosco C.A.C., et. al. [3] showed oscillations in the reflectivity change caused by the semi-transparent characteristic of silicon even at a wavelength of 388nm and 413nm, where the absorption length is 2 or 3 orders of magnitude smaller. Figure 4.33 shows the continuous change from a positive to a negative sign of the peak in the reflectivity in a very good way for a variation of the laser wavelength from 794nm to 814nm.

With the theory of the reflectivity change in transparent thin films on an opaque substrate, caused by acoustic pulses, the changes in the measurements can be explained as follows. In general three contributions to the reflectivity change are to be distinguished (Table 4.11, see also Chapter 2.4):

<i>Contributions to reflectivity change</i>	
Oscillations	Interferences of reflections of the probe laser pulse at the surface or the Al/Si interface, respectively and on the propagating acoustic pulse
Photoelastic contribution	Change of the reflectivity caused by the acoustic pulse in the underlying aluminium film through photoelasticity
Motion of the surface/ interfaces	Different motions of the surface and the Al/Si interface leads to changes in the reflectivity because of interference effects

Table 4.11 Contributions to the reflectivity change

Each contribution is now explained more in detail:

1) Oscillations

Oscillations can be observed, which are caused by the fact that the incident probe pulse is reflected at the surface and the other part is transmitted into the transparent film, where it is partly reflected by the propagating acoustic pulse. This part of the probe light pulse interferes constructively and destructively, depending on the propagating acoustic pulse with the part of the probe laser beam reflected at the surfaces (interface of transparent thin film and opaque substrate), which leads to oscillations of the signal detected by the photodetector. In this case (silicon cantilever), we can only observe these oscillations if we are working with a higher probe laser pulse power, which is explained by the very small photoelastic properties (Etchegion E. et. al. [16]). Then small oscillations are observed in the reflectivity with a frequency of 78GHz. According to Lin H.-N. et. al. [34] this leads to a wave speed of ~8500m/s assuming a real part of the refractive index n_{si} of 3.7 for silicon at a laser wavelength of 800nm. In the measurement presented in Figure 4.32 (right) these oscillations can not be observed, because the probe laser pulse power is kept very low (~2mW) to avoid damage of the cantilever.

In some other semi-transparent or transparent materials these oscillations can be measured easily even with small probe laser pulse power, because they have a much stronger photoelastic response than silicon at a optical wavelength of about 800nm. An example is presented in Chapter 4.2.2.

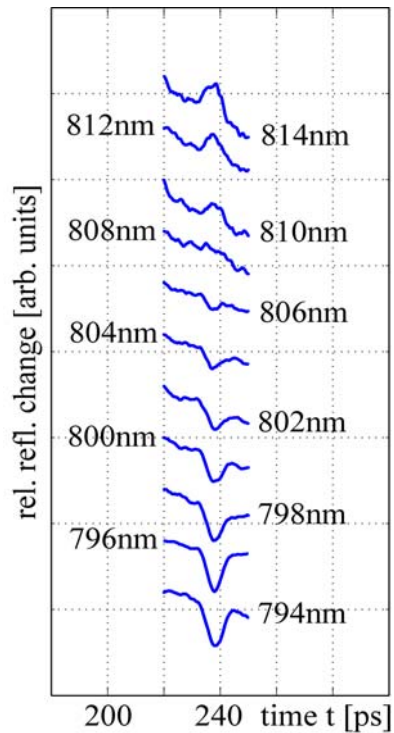


Figure 4.33 Reflectivity change depending on the laser wavelength

2) Photoelastic contribution

The photoelastic effect, which is the second contribution, must only be considered at the beginning of the measurement and at the time when the acoustic pulse is reaching the aluminium coating, which is in the order of 480ps. At the beginning of the measurement, it is almost impossible to distinguish all contributions to the reflectivity change. Beside the photoelastic contribution, the induced and diffusing heat in the cantilever also has an influence.

3) Motion of the surface/interface

In addition, the third effect, which is less known, contributes also to the reflectivity change in the first 10 to 20ps at the beginning of the measurement. This effect is independent of the coupling of the strain to the refractive index. But the optical reflectivity is affected by the motion of the cantilevers interfaces or surfaces, respectively.

The varying interferences of the optical probe light reflections at the interfaces or surfaces which are moving cause the change in the probe light reflectivity.

The motion of the free silicon surface when the acoustic pulse is reflected is the main reason for the reflectivity peak at 237ps in Figure 4.32. Since the photoelastic constants of silicon at a wavelength in the order of 800nm are very small (Etchegon E. et. al. [16]), the photoelastic contribution to the reflectivity change is neglected. After the first 40ps, as long as the acoustic strain pulse with general shape and displacement similar to Figure 4.34 is propagating in the silicon cantilever, no reflectivity change occurs because the distance between the free silicon surface and the interface is not changed. At the moment the acoustic strain pulse reaches the silicon surface, the stress-free silicon surface moves according to the displacement shape of the acoustic

pulse. Namely, with twice the amplitude of the displacement pulse because of the stress free boundary condition.

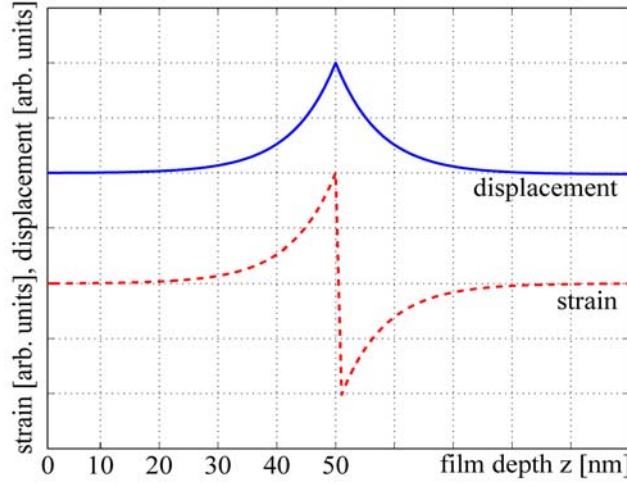


Figure 4.34 General pulse shape (strain and displacement), calculated for aluminium film

With the equations for the reflectivity change caused by the surface and interface motion ΔR_u out of Wright O.B. [89] (Eq. 23) formulated for perpendicular incident angle

$$\Delta R_u = 16 \Delta z \left(1 + \frac{1}{n_{Si}} \frac{dn_{Si}}{d\varepsilon_z} \right) k_{Si} r_0 (1 - r_0^2) n_e \cdot \quad (4.10)$$

$$\frac{2\kappa_e \cos(q) - N_1 \sin(q)}{[N_3 + r_0^2 N_2 + 2 r_0 (N_1 \cos(q) - 2\kappa_e \sin(q))]}^2$$

with

$$q = 2k_{Si}d \quad (4.11)$$

$$n_e = \frac{n_{Al}}{n_{Si}}, \quad \kappa_e = \frac{\kappa_{Al}}{n_{Si}} \quad (4.12)$$

$$N_1 = 1 - n_e^2 - \kappa_e^2, \quad N_2 = (1 - n_e)^2 + \kappa_e^2, \quad N_3 = (1 + n_e)^2 + \kappa_e^2 \quad (4.13)$$

$$k_{Si} = 2\pi \frac{n_{Si}}{\lambda} \quad (4.14)$$

$$r_0 = \frac{1 - n_{Si}}{1 + n_{Si}} \quad (4.15)$$

Δz denotes the surface displacement, d the thickness of the silicon part of the cantilever, n_{Al} and κ_{Al} the complex refractive index of the aluminium layer, n_{Si} the refractive index of silicon, λ the laser wave length. Furthermore, it is assumed that the photoelastic contribution $(dn_{Si})/(d\varepsilon_z)$ can be neglected. The surface displacement Δz is in the order of $\sim 0.003\text{nm}$ (Wright O.B. et. al. [92]). The presented results in Figure 4.35 are calculated for a single wavelength (monochromatic light). To illustrate the influence of a broader spectral content of the laser pulse, the convolution product of a typical laser pulse with gaussian spectral shape and the dependency of the reflectivity change with respect to the wavelength, is calculated. For the calculation, we set the spectral content to $\pm 16\text{nm}$ (see Figure 3.7), which is the same as spectral measurement shows in the experiments. The inset in Figure 4.35 shows the calculation with one wavelength (solid line) and the calculation for the broader spectral content (dashed line). The inset shows also the comparison of the peak height of the measurements presented in Figure 4.33 (points in Figure 4.35) and the calculated reflectivity change (dashed line in Figure 4.35), which shows an almost perfect agreement.

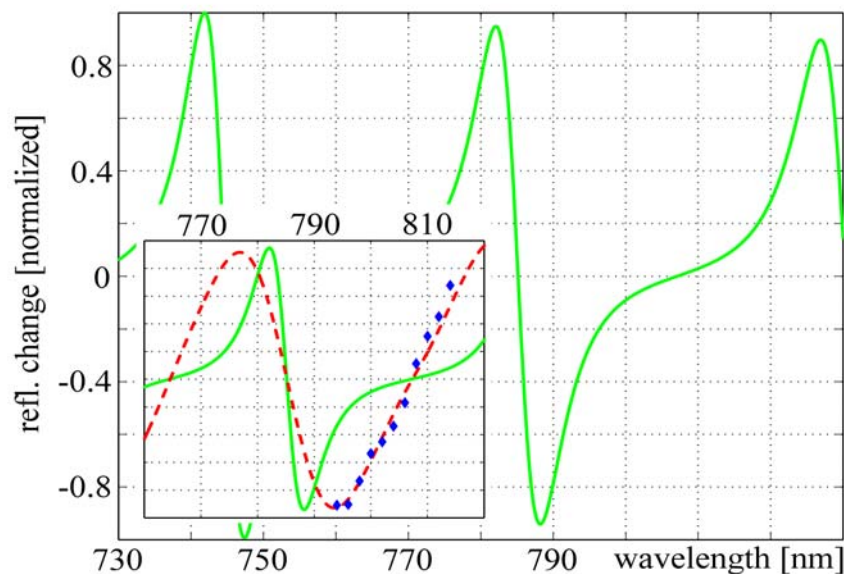


Figure 4.35 Dependency of the reflectivity change on the wavelength, calculated with (4.10) for the silicon cantilever; inset: comparison of the calculated change of reflectivity with the measured one (solid line - calculation with one wavelength, dashed line - illustration for a broader spectral content)

For silicon a refractive index n_{Si} of 3.7 is used in the simulation and the imaginary part is neglected. The refractive index of aluminium ($n_{Al} + i\kappa_{Al}$) is $2.8 + i 8.45$. It is assumed that no light is transmitted through the aluminium coating. The incidence of the probe laser beam is perpendicular to the surface of the

cantilever. The thickness of the silicon part of the cantilever is chosen to $1.951\mu\text{m}$ so that the zero crossing of the calculated reflectivity change is at the same wavelength as the measured one (807nm). Assuming a bulk wave speed in silicon (<100> direction) of 8430m/s and adding the time for the acoustic pulse propagation through the approximately 30nm aluminium coating, with a bulk wave speed of 6360m/s, one gets a total time of 236.1ps. This is in good agreement with the measurements (237ps) in Figure 4.33, if it is considered that all material properties - elastic and optical - are slightly affected by the induced temperature in the cantilever.

In conclusion, measurements of the bulk acoustic wave propagation in a silicon cantilever, which are used for the determination of geometrical dimensions or material properties, are presented. The measured signal corresponds to the reflectivity change which is dominated by the surface motion, because the photoelastic constants of silicon at a wavelength of 800nm are very small. The sign of the reflectivity depends on the laser wavelength, which is shown in the measurements and corresponds very well with the theory. The measured reflectivity change caused by the acoustic pulse is proportional to the displacement of the free silicon surface. This allows to estimate the displacement and the strain amplitude of the acoustic pulse. Furthermore, it is possible to study the influence of material properties, such as the electron-phonon coupling or the film thickness in case of very thin coatings on the acoustic pulse shape.

4.4.2 AFM tips

The temporal resolution of the presented measurement technique is very high and only limited by the laser pulse duration (100fs). Therefore a very high resolution in the propagation direction (thickness direction) of the acoustic pulses is achieved ($>1\text{nm}$). The introduction of an acoustic focussing tip (modified AFM tip), in which the acoustic pulses (wavelength 10nm-20nm) are focussed is a new possibility to improve the lateral resolution, which is currently limited in the order of some microns.

The following experiments show for the first time that the proposed combination of a micro-scale acoustic focussing tip and the accurate high frequency acoustic experiment is feasible. This leads to a device with very high resolution in time and space. In this section the possibilities and limitations of the modifications by means of a focussed ion beam (FIB) are shown. Additionally, first acoustic experiments on AFM tips are presented.

4.4.2.1 Motivation - focussing of acoustic pulses

The wavelength of the excited longitudinal acoustic pulses is in the order of the absorption length of the laser light. As mentioned before, metallic thin

films have absorption lengths of 10nm to 20nm, which correspond to frequencies of several GHz. The detection system demands a very high temporal resolution in order to detect mechanical pulses having such high frequencies. The resolution in the time domain is realized with a delay line (Chapter 3) and therefore the minimal time step Δt_{min} amounts to

$$\Delta t_{min} \approx \frac{\Delta s_{min}}{c} \quad (4.16)$$



Figure 4.36 Scheme of the focusing tip acting as an acoustic lens

Δs_{min} is the minimal step size of the translation table and c the speed of light. In the presented experimental setup the minimal step size Δs_{min} of the mechanical translation table amounts to $1\mu\text{m}$, which corresponds to a temporal resolution of 3.33fs. This very high temporal resolution is only limited by the laser pulse duration, which is, in our case, shorter

than 100fs. With a microscope objective the spot size of the laser pulse is in the order of a few wavelengths of the laser light. In contrast to the small wavelength of the acoustic pulse and the high resolution in time domain, the spot size (pump and probe laser pulse) is orders of magnitude larger. The introduction of a focussing tip, in which acoustic pulses are focussed (Figure 4.36), leads to a device for exciting and measuring acoustic waves or other effects with very high lateral and in-depth resolution. The lateral resolution depends on the geometry of the tip. The acoustic waves are excited at the base of the tip with the strong pump laser pulse. Due to the reflections at the boundaries, the acoustic pulse is focussed towards the sharp end of the tip and its amplitude is increased. The introduced focussing tip has two major advantages:

- increased amplitude at the sharp end of the tip and
- small cross-sectional area at the sharp end (high lateral resolution)

The increase of the amplitude depends on the wave propagation inside the tip, both depending on the frequency of the acoustic pulse and the geometry of the tip. The wave propagation in similar cases, but with macroscopic dimensions, is discussed by Profunser D.M. et. al. [53]. An application of this new technique as a transducer or in a new scanning probe method is conceivable.

4.4.2.2 Specimen preparation

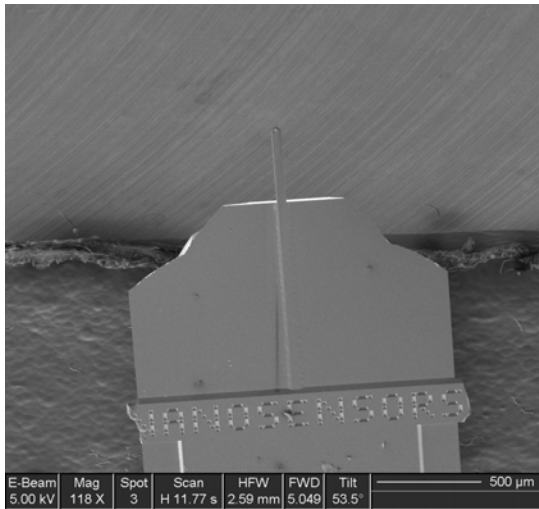


Figure 4.37 Silicon cantilever used for modifications with focussed ion beam (FIB)

The specimens for a first series of experiments are prepared with a focussed ion beam (FIB) at EMPA Dübendorf. The focussed ion beam technique enables modifications with a resolution in the order of 100nm. The used workstation incorporates a FIB and a SEM stage. The operating principle of a focussed ion beam machine is similar to a SEM, but a focused beam of Ga^+ ions is scanned across the specimen instead of electrons (Gasser P. et. al. [17]). FIB is widely used, for example in the modification of electronic chip designs, TEM sample preparation and for

modifications of micro- and nanostructures. So, it is the right approach for preparing the tip of silicon cantilevers (Figure 4.37) for measurements with picosecond ultrasound. The silicon cantilever is the same as the one used in Chapter 4.4.1.

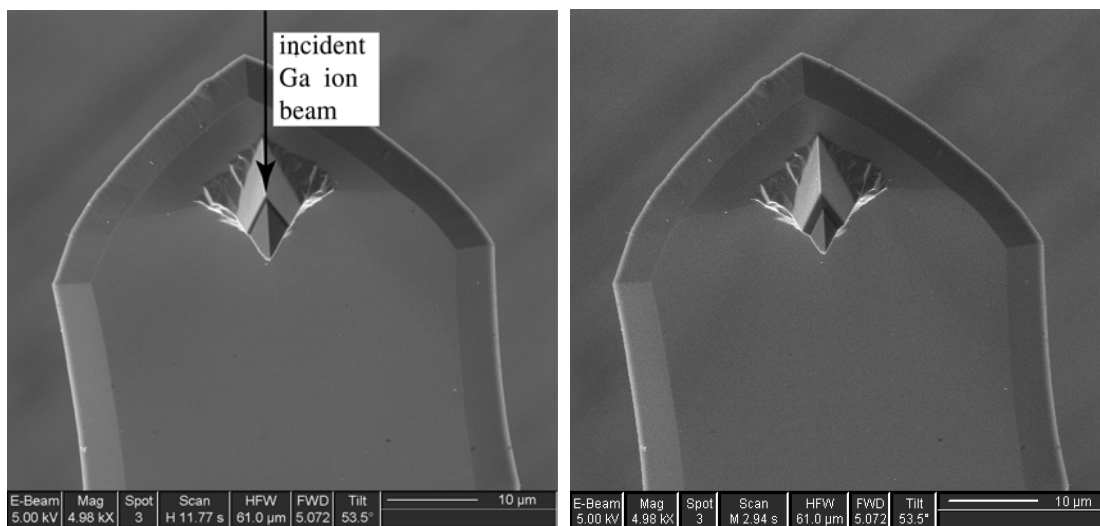


Figure 4.38 AFM tip preparations using focussed ion beam (FIB), images taken during modification

Figure 4.38 shows two images during the removal of the sharp end of the tip. The incident Ga^+ ion beam is indicated by an arrow (Figure 4.38 (right)). Since the Ga^+ ion beam has a total divergence angle of approximately 1.3° .

The cantilevers were tilted by the half of this angle to achieve a cross section of the tip, which is parallel to the cantilever. Typical FIB parameters for the modification of the tip are as follows

	<i>Acc. Voltage [kV]</i>	<i>Current [pA]</i>
Removing main part of the tip	30	1000
Final improvement of the surface	30	100

Table 4.12 FIB parameters

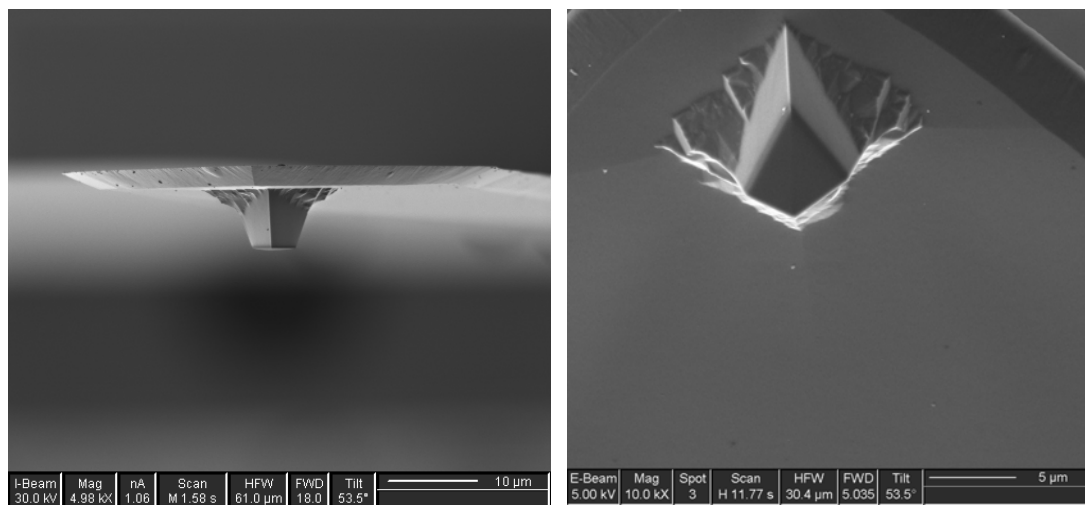


Figure 4.39 Truncated AFM tip for measuring picosecond ultrasound

Figure 4.39 shows one of the prepared tips with a total height (including the thickness of the cantilever) of $7.40\mu\text{m}$. The bombardment of the sample with heavy, and therefore, highly energetic Ga^+ ions cause a damage of the surface layer (several nanometers) of the truncated tip, resulting in an amorphization of the surface (Gasser P. et. al. [17]). This can be observed in Figure 4.39 (dark part) in the cross section of the truncated tip. Moreover, Ga is implanted in the specimens surface because of the scanning with the ion beam during imaging with the ion beam (Gasser P. et. al. [17]). To avoid most of the damage, the ion beam current is kept as low as possible. Since a decrease of the current has the consequence of a strongly increased duration for removing the tip, it was performed in two steps (Table 4.12). First, the main part of the tip was removed with a high current (1000pA). Then, a small part of the cross section, the main part of the amorphous layer, was removed with a lower current (100pA).

4.4.2.3 Measurements on truncated AFM - tips

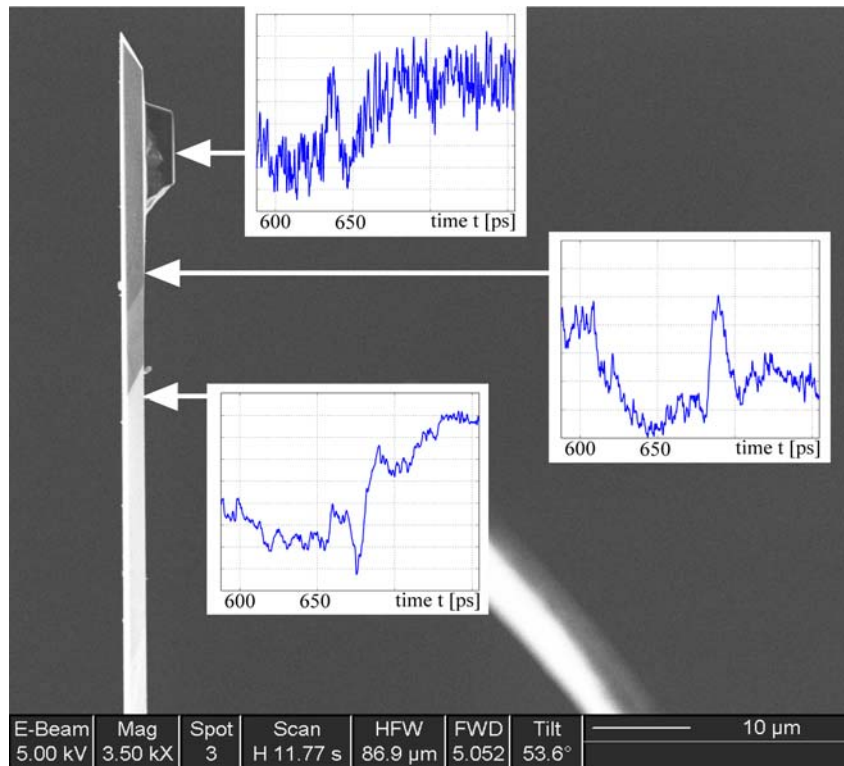


Figure 4.40 Measurements and measurement configuration (cantilever thickness $\sim 2\mu\text{m}$)

For measuring the wave propagation in the modified AFM tips, the setup, according to Figure 3.19, is used, where the specimen is accessed with pump and probe beam from opposite sides. Therefore truncated AFM tips are used for the investigation of the wave propagation on the microscopic scale. On the left hand side of the cantilever (thickness $\sim 2\mu\text{m}$) in Figure 4.40, the acoustic pulses are launched on the aluminium coating of the cantilever. As indicated with the arrows, the reflectivity is scanned versus time on the opposite side. In the following, the acoustic measurement on a $\sim 5.5\mu\text{m}$ high (including the cantilever) truncated tip is discussed. In general, the location of the tip on the cantilever can be found easily, because the sloping sides of the truncated tip causes a diffusive reflection of the probe laser beam, which corresponds also to a small, almost vanishing, light intensity in the photodetector. Nevertheless, several measurements along the cantilever are performed, to ensure measurements on the correct location and to show the difference of measurements on the cantilever and on the truncated tip. This lateral scan along the cantilever is started in the order of $40\mu\text{m}$ away from the tip in the middle of the cantilever. On the starting point, the signal corresponding to the reflectivity change is optimized. In Figure 4.40, two measurements are presented, one approxi-

mately $25\mu\text{m}$ away from the tip and one at about $12.5\mu\text{m}$. In both measurements, a reflectivity peak at 680ps can be observed. The reason for the lower quality compared with thin film measurements is that the setup is only optimized once, at the beginning of the lateral scan along the cantilever and that these measurements are only averaged 5 times. The peak at 680ps corresponds to the acoustic pulse which travelled 3 times through the cantilever. But if the line scan is continued, one reaches a region, where no probe light is reflected back to the photodetector, because of the diffusive reflection at the slopes of the tip. Reaching the tip, the reflectivity peak occurs at 640ps , which corresponds to a travelling distance of $5.44\mu\text{m}$. With the SEM in the focussed ion beam machine, a tip height of $5.5\mu\text{m}$ is determined.

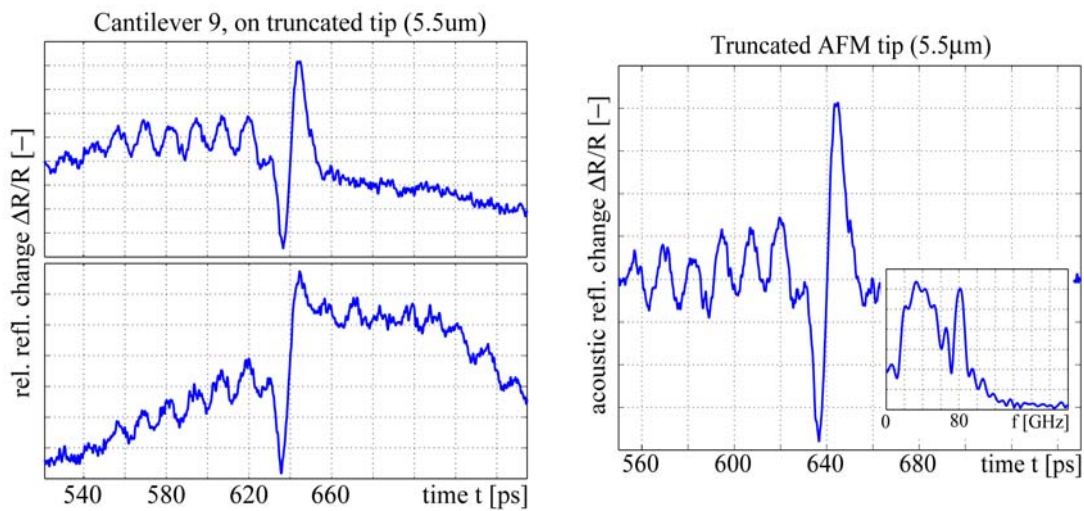


Figure 4.41 Left: Two measurements on the truncated AFM tip; right: same measurement as the upper one on the left hand side, but after high pass filtering (inset: fast fourier transform of the measured signal)

The two curves in Figure 4.41 (left) show measurements using the same configuration. The peak of the reflectivity change at 640ps can be observed clearly in both measurements, which represent an average of 50 single measurements using a pump average power of approximately 15mW and a center wavelength of about 790nm . The difference between the two measurements is, the further optimizing of the reflectivity change by small changes of the pump beam position. In the reflectivity change, again oscillations occur, which have a frequency of about 80GHz . Most likely these oscillations are interferences of the probe light reflected at the tip surface and the reflections at the propagating acoustic pulse, similar to the explanations presented in Chapter 4.2. Using the real part of the refractive index of silicon n_{Si} 3.7, these oscillations should have a frequency (Equation (4.9)) of 78GHz , which is very close to the measured frequency. Reasons for the difference of the frequencies might be, on the

one hand, the slightly different optical properties of the surface (cross section of the tip), which are modified through the FIB and on the other hand, an increased temperature in the tip.

Experiments with another tip of 6.2 μm height show similar results. In a next step, the experiments should be performed in the configuration proposed in Figure 4.36, which is discussed in the following outlook.

Chapter 5

Conclusions and Outlook

5.1 Simulation and modelling of the experiment

A thermo-mechanical simulation is presented using numerical FDTD methods. For describing the absorption and induced temperature change caused by the absorbed laser pulses different models were implemented. Also non-equilibrium heating is considered, which is caused by the very short duration of the laser pulses. Linear elastic material is assumed for the calculation of the wave propagation. The simulations were applied for determining the fast transient heating in different materials, such as aluminium or copper, as well as for discussing the characterization of diffusion barriers below a copper top layer.

Acoustic pulseshaping by means of trains of ultrashort laser pulses or variations of the laser pulse shape itself is a field, where these accurate simulations enable the production of the appropriate laser pulse shape for a desired sound wave. Additionally this thermo-mechanical simulation can show, which acoustic pulse shape in the chosen material and configuration can be excited. Furthermore, the interaction of these more complex acoustic pulse shapes with structured specimens are an interesting future field.

Extension of the one-dimensional thermodynamic models to the 2D and 3D cases is an interesting field since the numerical simulations of the mechanical wave propagation for the axi-symmetric quasi 3D case are already realized. This quasi 3D simulations are interesting in connection with the application of picosecond ultrasound on specimens structured with dimension smaller than the spot size. Using such simulations, the measured reflectivity change can be assigned to defects or variations of geometrical dimensions, although the structures have sub-wavelength dimensions. Moreover, the discussion of

excited surface acoustic waves is an interesting future field using accurate simulations.

5.2 Experimental setup

Two different experimental setups using the same laser source were developed. In the first setup pump and probe pulses hit the specimen from the same side. Due to the chosen optical realization the achieved spot size on the specimen is in the order of $100\mu\text{m}$ and is suitable for working with thin film characterization. However, the second setup is realized with microscope objectives and therefore, the spot size is much reduced such that ultrasonic experiments in single structures, with dimensions below $5\mu\text{m}$, are possible. Pumping and probing is performed from opposite sides.

So, a modification in which the specimen is accessed with pump and probe laser from one side, focussed with a single microscope objective (co-linear pump-probe setup) could provide a similar spot size and would be very interesting in connection with ultrasonic measurements in microstructures or lateral structured thin films.

Since the same microscope objective is used for focussing pump and probe beams towards the specimen, optical crosstalk with the consequence of a poorer signal to noise ratio might become a limiting problem. A solution would be to work with different optical wavelength for pumping and probing. In addition, the accuracy of the positioning devices should be improved.

Using parts of high frequency optical communication technology enables measurements with extremely high frequency content. The application of these developments for real time measurements, without using a delay line, is conceivable and would be very interesting from an engineering point of view.

5.3 Experimental results

Thin film characterization

Measurements of the bulk acoustic wave propagation were used for measuring sound velocity in aluminium films as a function of the thickness of the coating. This can be applied to any other material to investigate the dependency of its properties on thickness or process conditions. Well characterized thin aluminium films can be used as transducers at a optical wavelength of 800nm if the photoacoustic response is too small.

Diffusion

It has been shown that the diffusion layer of a gold and aluminium interface can quantitatively be characterized by means of ultrashort pulse laser acous-

tics. The use of defined diffusion layers with varying mechanical properties for acoustic filtering devices has already been investigated and is further pursued.

Diffusion barrier layers

Thin diffusion barrier layers are used to avoid diffusion of copper into the silicon semiconductor. Apart from a single tantalum layer, also tantalum-nitride (TaN), tungsten-nitride (WN) and tantalum/tantalum-nitride multilayers are candidates for diffusion barriers below copper films. In this thesis it has been shown that the resolution of picosecond ultrasound is high enough to determine mechanical properties or the thickness of mono- or bilayered diffusion barriers below a copper or an aluminium/copper layer. In addition, the limitations of this technique, with respect to minimal film thickness and accuracy, are investigated and the bulk wave velocity of tantalum and tantalum-nitride is determined, which can be used for estimating their Young's moduli.

Because mechanical properties of most new thin film materials, such as tantalum-nitride are very rare, picosecond ultrasound is the right approach to determine these properties and their almost unknown dependency on deposition condition or deposition technique, respectively. In the semiconductor industry the requirements on speed, feature size and reliability always lead to changing thin film stacks, use of new materials and technologies and therefore, to many specific, but interesting problems from a scientific and engineering point of view.

Microstructures

Non-destructive characterization of silicon-nitride membranes and silicon cantilevers with dimensions in the micrometer range or lower has been shown, using high frequency ultrasound excited by ultrashort laser pulses. By measurements in semi-transparent silicon cantilevers it is shown, that a detection of the acoustic pulses is also possible, if the photoacoustic effect vanishes. Instead of the photoacoustic effect, the difference of the motion of front and back surface of the cantilever changes the reflectivity, which could be shown by the changing sign of the measured reflectivity change.

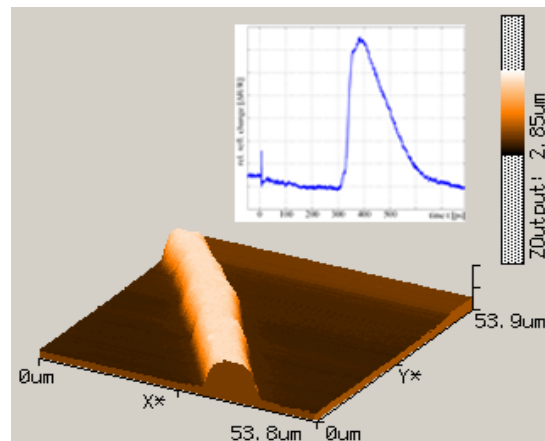


Figure 5.1 Picosecond ultrasound measurement on a single aluminium line (top width ~5µm)

This technique is developed in a way that is suitable for the characterization of any freestanding or substrate-supported microstructure. The minimum feature size of a single structure corresponding to the lateral resolution, is in the order of 4 microns (Figure 5.1) which was tested with different single aluminium lines. Using several similar objects, such as carbon nanotubes or metallic lines with nanometer dimensions, it might be also possible to even characterize them if their dimensions are smaller than the spot size, when their number is increased with decreasing size.

AFM tips

For the first time measurements of the bulk wave propagation in a single truncated silicon AFM tip is presented. An optical setup was used, where pump and probe beam hit the AFM tip from opposite sides.

Future studies, for instance, the interaction of propagating acoustic bulk waves with near field forces or the effects of wave focussing in the AFM tip, demand further developments on the experimental setup.

Apart from or in connection with the AFM tips acoustic lenses at the surface (Figure 5.2), where the laser pulses are absorbed are interesting for the focussing of acoustic pulses.

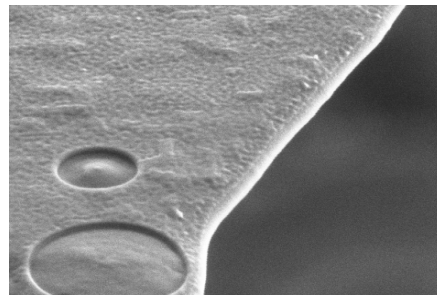


Figure 5.2 FIB milled acoustic lenses (diameter 2 μm and 5 μm) at the surface of a silicon cantilever

Appendix A: Material properties

<i>Property</i>	<i>Al</i>	<i>Cu</i>	<i>Ta</i>	<i>TaN</i>	<i>Si</i>
Heat capacity c [J/(kg K)] [11]	897	385	140	205	705
Lattice heat capacity C_l [J/(m ³ K)] ^{a)}	2.39 E6	3.42 E6	2.18 E6	2.94 E6	1.64 E6
Elec. heat capacity C_e [J/(m ³ K)] ^{b)}	2.76 E4	2.94 E4	-	-	-
Thermal conductivity K [W/(mK)] [38]	237	398	57.5	7.9 ^{d)}	130 ^{c)}
Electron-phonon coupling constant G [W/(m ³ K)] [79] [94]	4.9 E17	6.0 E16	-	-	-
Density ρ [kg/m ³] [12]	2700	8960	15586 ^{d)}	14360 ^{d)}	2330
Young's modulus E [GPa]	71	123	145 ^{e)}	461 ^{e)}	130
Poisson constant ν	0.34	0.35	0.34	0.34	0.28
Expansion coefficient α [1/K] [12]	23.1 E-6	16.5 E-6	6.3 E-6	3.6 E-6	2.6 E-6 ^{c)}
Reflectivity R (800nm)	0.87	0.96	0.73	-	-
Reflectivity R (400nm)	-	0.51	-	-	-
Absorption length [nm] (800nm)	7.54	12.65	18.5	-	-
Absorption length [nm] (400nm)	-	14.41	-	-	-

<i>Property</i>	<i>Au</i>	<i>Pt</i>	<i>Sapphire</i>
Heat capacity c [J/(kg K)] [11]	129	133	-
Density ρ [kg/m ³] [12]	19300	21500	3990
Young's modulus E [GPa]	78	170	345
Poisson constant ν	0.42	0.39	0.24
Expansion coefficient α [1/K] [12]	14.2 E-6	8.8 E-6	-
Reflectivity R (800nm)	0.97	0.71	-
Absorption length [nm] (800nm)	12.45	12.86	-

- a) calculated with $C = C_l + C_e$ from heat capacity and density
- b) calculated with parameter out of [23]
- c) database of IOFFE (www.ioffe.rssi.ru)
- d) internal report
- e) internal report, estimated from measurements
- all optical properties (reflectivity and absorption length) calculated with data out of [49]

Appendix B: Magic time step

The limit of the Neumann stability analysis, which results according to [33] in

$$\Delta t \leq \frac{\Delta z}{c_I} \quad (\text{B.1})$$

is the special case, in which

$$\Delta t = \frac{\Delta z}{c_I} \quad (\text{B.2})$$

and is called *magic time step*. Δt denotes the time step, Δz the step size in space domain and c_I the bulk wave velocity.

In the following one-dimensional derivation u is a function depending on the parameter z . The derivatives of u with respect to z are developed from the Taylor-series at the point $z_i + \Delta z$, and $z_i - \Delta z$. z_i denotes the multiplication of the index i with the step size Δz . The Taylor-series of function u at these space points $z_i + \Delta z$ and $z_i - \Delta z$ are

$$u(z_i + \Delta z) = u_i + \Delta z \frac{\partial u}{\partial z} \Big|_{z_i} + \frac{(\Delta z)^2}{2} \frac{\partial^2 u}{\partial z^2} \Big|_{z_i} + \sum_{m=1}^{\infty} \frac{(\Delta z)^{m+2}}{(m+2)!} \frac{\partial^{m+2} u}{\partial z^{m+2}} \Big|_{z_i} \quad (\text{B.3})$$

$$u(z_i - \Delta z) = u_i - \Delta z \frac{\partial u}{\partial z} \Big|_{z_i} + \frac{(\Delta z)^2}{2} \frac{\partial^2 u}{\partial z^2} \Big|_{z_i} + \sum_{m=1}^{\infty} \frac{(-\Delta z)^{m+2}}{(m+2)!} \frac{\partial^{m+2} u}{\partial z^{m+2}} \Big|_{z_i} \quad (\text{B.4})$$

in which u_i denotes the function u at the point z_i . The subtraction of these two equations (B.3) and (B.4) yields the first derivative of u with respect to z at position z_i

$$\frac{\partial u}{\partial z} \Big|_{z_i} = \frac{u_{i+1} - u_{i-1}}{2\Delta z} - \sum_{m=1}^{\infty} \frac{(\Delta z)^{2m}}{(2m+1)!} \frac{\partial^{2m+1} u}{\partial z^{2m+1}} \Big|_{z_i} \quad (\text{B.5})$$

Consequently, the derivative of u with respect to z is approximated by the first term in equation (B.5). The second part relates to the error from the exact derivative. If both Taylor-series (B.3) and (B.4) are added, the second derivative with respect to z yields

$$\frac{\partial^2 u}{\partial z^2} \Big|_{z_i} = \frac{u_{i+1} - 2u_i + u_{i-1}}{(\Delta z)^2} - 2 \sum_{m=1}^{\infty} \frac{(\Delta z)^{2m}}{(2m+2)!} \frac{\partial^{2m+2} u}{\partial z^{2m+2}} \Big|_{z_i} \quad (\text{B.6})$$

In a similar way the n^{th} derivative can be developed.

For the discretization of the one-dimensional wave equation

$$u_{tt} = c_l^2 u_{zz} \quad (\text{B.7})$$

the approximation of the second derivative (B.6) is used in time and space

$$\frac{u_i^{n+1} - 2u_i^n + u_i^{n-1}}{(\Delta t)^2} - 2 \sum_{m=1}^{\infty} \frac{(\Delta t)^{2m}}{(2m+2)!} \frac{\partial^{2m+2} u}{\partial t^{2m+2}} \Bigg|_{z_i, t_n} =$$

$$c_l^2 \left\{ \frac{u_{i+1}^n - 2u_i^n + u_{i-1}^n}{(\Delta z)^2} - 2 \sum_{m=1}^{\infty} \frac{(\Delta z)^{2m}}{(2m+2)!} \frac{\partial^{2m+2} u}{\partial z^{2m+2}} \Bigg|_{z_i, t_n} \right\} \quad (\text{B.8})$$

n denotes the index in the time domain and Δt is the time step. With equation (B.8) the function at the new time step u_i^{n+1} is estimated using u_i^n and u_i^{n-1} . The error of the estimation as given by the summation terms is

$$u_{err} = 2 \sum_{m=1}^{\infty} \left(\frac{(\Delta t)^{2m+2}}{(2m+2)!} \frac{\partial^{2m+2} u}{\partial t^{2m+2}} \Bigg|_{z_i, t_n} - c_l^2 \frac{(\Delta t)^2 (\Delta z)^{2m}}{(2m+2)!} \frac{\partial^{2m+2} u}{\partial z^{2m+2}} \Bigg|_{z_i, t_n} \right) \quad (\text{B.9})$$

Equation (B.9) yields

$$u_{err} = 2 \sum_{m=1}^{\infty} \left(\frac{\left((\Delta t)^{2m} c_l^{2m+2} - c_l^2 (\Delta z)^{2m} \right) (\Delta t)^2}{(2m+2)!} \frac{\partial^{2m+2} u}{\partial z^{2m+2}} \Bigg|_{z_i, t_n} \right) \quad (\text{B.10})$$

considering the general solution of d'Alembert. In case of infinitesimal small steps in the time and hence, in space domain, the estimated error vanishes according to equation (B.10) - or the error vanishes if

$$(\Delta t)^{2m} c_l^{2m+2} - c_l^2 (\Delta z)^{2m} = 0 \quad (\text{B.11})$$

which is equivalent to

$$\Delta t = \frac{\Delta z}{c_l} \quad (\text{B.12})$$

Therefore, the time step determined by equation (B.12) is called *magic time step* Δt_{magic} (Taflove A. et. al. [76]). If the numerical experiments are run with the magic time step, the numerical dispersion vanishes and the result is the

exact solution of the wave equation sampled with the chosen spatial resolution. The following Figure B.1 presents a comparison of the numerical simulations of the wave propagation of an acoustic pulse induced by an ultra-short laser pulse calculated with different time steps. The resulting curve right at the bottom of Figure B.1 is calculated with the magic time step Δt_{magic} , however, the other ones with smaller time steps Δt . Since the frequency content of this acoustic pulse is very high the effect of the numerical dispersion on the pulse shape is strong, as it is shown in Figure B.1.

Extensions for using the magic time step for 2D- and 3D-wave propagation problems are not successful, because usually the different waves, i.e. shear waves and longitudinal waves, have also different wave speeds and require different time steps.

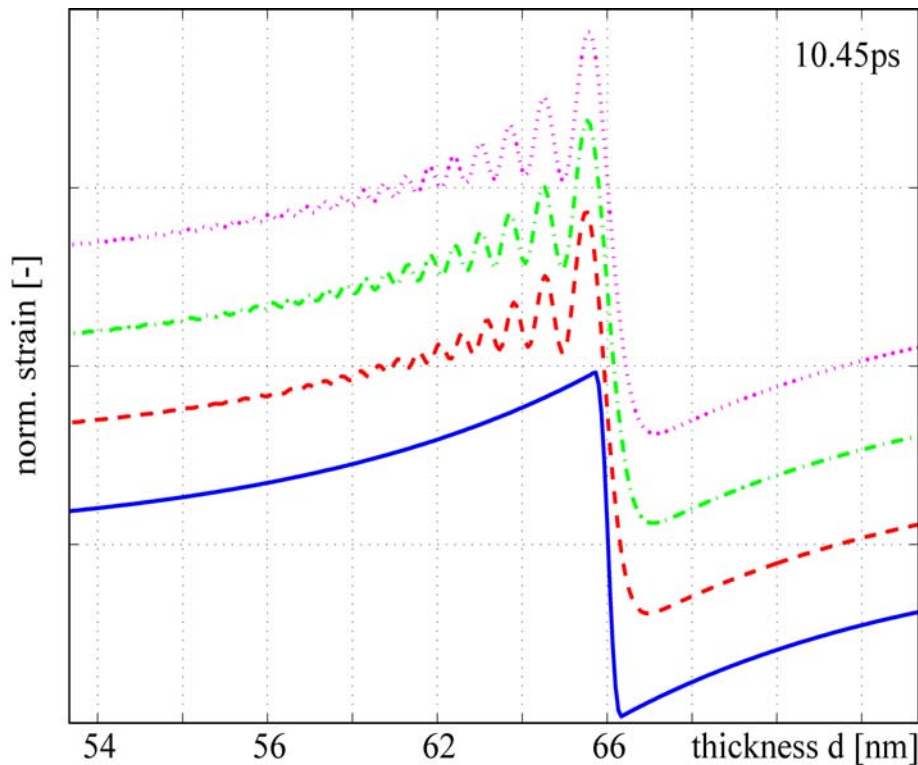


Figure B.1 Comparison of the numerical simulations (vertical shifted) of the acoustic wave propagation in an aluminium thin film (100nm) with (solid line, right at the bottom) and without magic time step (right at the top (dotted line): $\Delta t = \Delta t_{magic}/8$, second (dash-dotted): $\Delta t = \Delta t_{magic}/4$, third (dashed line): $\Delta t = \Delta t_{magic}/2$)

Further explanations on the magic time step are given by Taflove A. et. al. [76].

Appendix C: Reflectivity change

To connect the derivatives of the refractive index with respect to the predominant strain distribution $((\partial n)/(\partial \varepsilon_z)$ and $(\partial k)/(\partial \varepsilon_z)$ of Chapter 2.4.1) with the photoelastic (piezo optical) constants P_{kl} , we follow the explanations of Matsuda O. et. al. [40].

Henceforth the strain is denoted with η_z instead of ε_z so that one does not confuse the components of the strain with the dielectric tensor. The contribution of the uniaxial strain η_z to the change $\Delta \varepsilon$ of the dielectric constants is

$$\Delta \varepsilon = \begin{bmatrix} P_{12} & 0 & 0 \\ 0 & P_{12} & 0 \\ 0 & 0 & P_{11} \end{bmatrix} \eta_z \quad (\text{C.1})$$

assuming an isotropic photoelastic tensor in which P_{11} and P_{12} are the only two independent photoelastic constants. The photoelastic constants P_{kl} can also be expressed using Pockels coefficients p_{kl} (Matsuda O. et. al. [40]). If the probe laser beam incidence is perpendicular to the surface of the specimen only $\Delta \varepsilon_x$ and $\Delta \varepsilon_y$ of the change of the dielectric tensor have to be considered, to describe the optical modulation.

From equation (C.1) follows

$$\Delta \varepsilon_x = \Delta \varepsilon_y = P_{12} \eta_z = -\varepsilon^2 p_{12} \eta_z \quad (\text{C.2})$$

According to [40] equation (C.2) can be rewritten in terms of the complex refractive index n^*

$$\Delta n^* = \frac{P_{12}}{2n^*} \eta_z = -\frac{n^{*3}}{2} p_{12} \eta_z \quad (\text{C.3})$$

or as

$$\frac{\partial}{\partial \eta_z} n^* = \frac{\partial n}{\partial \eta_z} + i \frac{\partial \kappa}{\partial \eta_z} = \frac{P_{12}}{2n^*} = -\frac{n^{*3}}{2} p_{12} \quad (\text{C.4})$$

It is understood that the photoelastic constants are wavelength dependent and in opaque material also complex quantities.

Appendix D: Electro-optical modulator

The electrical resonator is built according to Figure D.1. Capacity $C1$ is 300pF, the coil $L1$ has 1.6 μ H and the Capacity $C2$ is variable between 0.8pF and 12pF. According to the manufacturer one can approximate the electro-optical modulator as capacity of 30pF¹. Measurements at the Laboratory for Electromagnetic Fields and Microwave Electronics of ETH Zurich turned out a capacity C_{EOM} of 32pF. This capacity C_{EOM} should be taken into account, if the resonance frequency f_{Res} is calculated. The resonance frequency f_{Res} of the open-circuit is

$$f_{Res} = \frac{1}{2\pi\sqrt{L_1 C_2}} \quad (D.1)$$

but if the EOM is connected to the tank circuit, the resonance frequency f_{Res} changes to

$$f_{Res} = \frac{1}{2\pi\sqrt{L_1(C_2 + C_{EOM})}} \quad (D.2)$$

With the values mentioned above the resonance frequency f_{Res} is between $f_{Res_min} = 18.97$ MHz (with $C2_{max}$) and $f_{Res_max} = 21.97$ MHz (with $C2_{min}$).

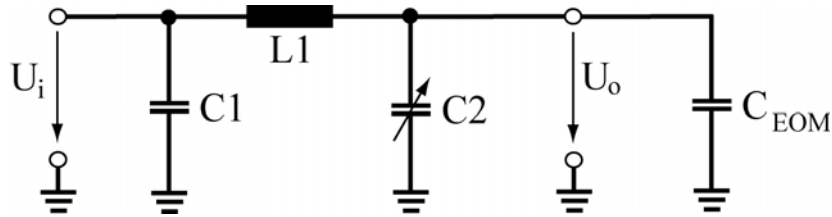


Figure D.1 Scheme of the tank circuit (electrical resonator)

The adjustment of the capacity $C2$ is done in an experimental way so that the resonance frequency is exactly at 19MHz. The measurements are performed at the Laboratory for Electromagnetic Fields and Microwave Electronics. With the use of a network analyzer (NWA) the ratio of the reflected power to the incident power ($S11$) is measured with respect to the frequency, according to the measurement configuration in Figure D.2. At the resonance frequency most of the power is transmitted through the resonant circuit and hence it follows, that the ratio $S11$ has a minimum at the resonance frequency f_{Res} of the circuit.

¹ Oral contribution of the manufacturer ConOptics for our EOM-Type 350-50

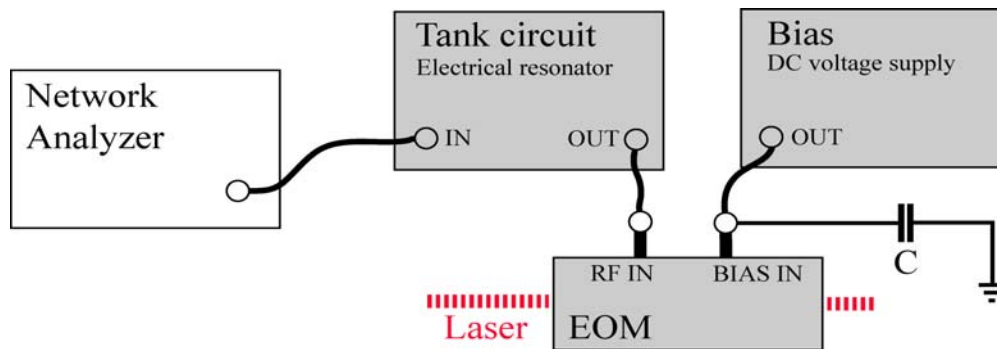


Figure D.2 Measurement configuration for the adjustment of the resonance frequency of the electrical resonator

In general, measurements of the resonance frequency of resonant circuits, such as the used tank are slightly difficult since the probe disturbs the results even if the capacity is very low or the ohmic resistance very high. The results of the measurements are presented in the charts in Figure D.3. The upper chart shows the frequency dependence of the reflected power S_{11} at the maximum of the variable capacity C_2 ($C_{2_{max}}$). At the resonance frequency $f_{Res_{min}}$ (18.746MHz) the reflected power S_{11} is lowest and in the presented case -21.261dB which means that most of the power is transmitted to the output of the tank circuit. The measured resonance frequency $f_{Res_{max}}$ with minimum of the variable capacity C_2 ($C_{2_{min}}$) is 21.558MHz and S_{11} is only -15.709dB. For values of S_{11} below -15dB the adjustment is very good and it is guaranteed that most of the power is transmitted to the output of the resonant circuit. The agreement of the measured resonance frequencies with the predicted values is also very good if one bears in mind that parasitic elements such as parasitic resistors or capacitors are neglected.

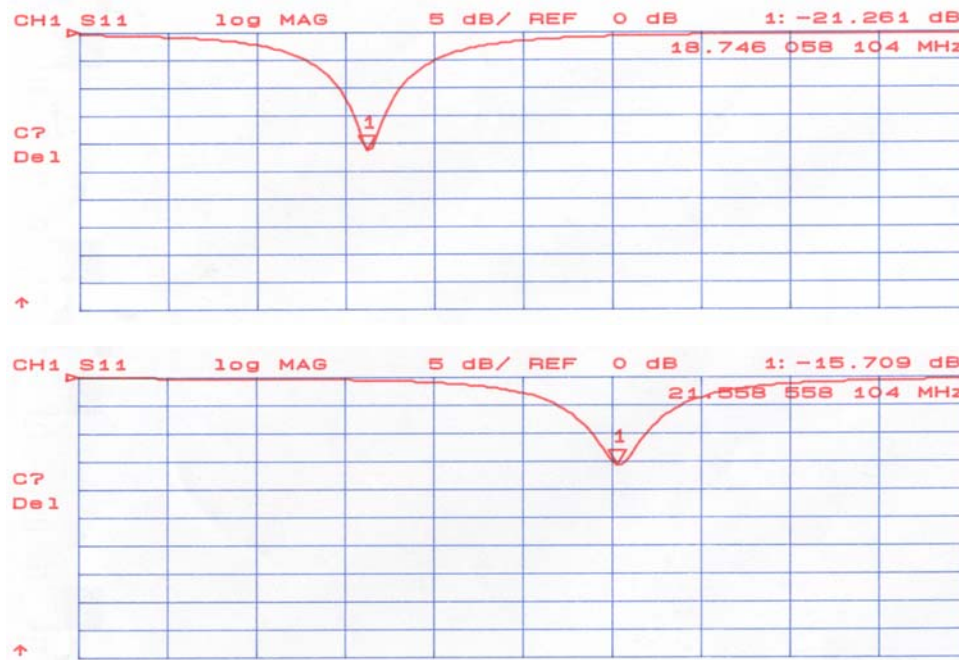


Figure D.3 Frequency dependence of the parameter S_{11} ; top: minimum of the resonance frequency f_{Res_min} at the maximum of the variable capacity C_2 (C_{2_max}); bottom: maximum of the resonance frequency f_{Res_max} at the minimum of the variable capacity C_2 (C_{2_min}); values of S_{11} and the resonance frequency which correspond to the marker 1 are given in the right upper corner of each diagram (vertical scale: -5dB/division, start (top) 0dB; horizontal scale: 1MHz/division, start (left) 15.5MHz)

Bibliography

- [1] Anisimov S.I., Kapeliovich B.L., Perel'man T.L., *Electron emission from metal surfaces exposed to ultrashort laser pulses*, Sov. Phys. JETP, Vol. 39, No. 2, pp. 375-377, August 1974
- [2] Bonello B., Perrin B., Romatet E., and Jeannet J.C., *Application of the picosecond ultrasonic technique to the study of elastic and time-resolved thermal properties of materials*, Ultrasonics, Vol. 35, pp. 223-231, 1997
- [3] Bosco C.A.C., Azevedo A. and Acioli L.H., *Laser-wavelength dependence of the picosecond ultrasonic response of a NiFe/NiO/Si structure*, Physical Review B, Vol. 66, Art. No. 125406, September 2002
- [4] Brorson S.D., Kazeroonian A., Moodera J.S., Face D.W., Cheng T.K., Ippen E.P., Dresselhaus M.S. and Dresselhaus G., *Femtosecond Room-Temperature Measurement of the Electron-Phonon Coupling Constant λ in Metallic Superconductors*, Physical Review Letters, Vol. 64, No. 18, pp. 2172-2175, April 1990
- [5] Bryner J., *Experimentelle Ermittlung der mechanischen Eigenschaften von dünnen Filmen*, Diplomarbeit WS 2001, ETH Zürich
- [6] Chen J.K., Latham W.P. and Beraun J.E., *Axisymmetric modeling of femtosecond-pulse laser heating on metal films*, Numerical Heat Transfer, Part B, Vol. 42, pp. 1-17, 2002
- [7] Chen J.K., Beraun J.E. and Tham C.L., *Investigation of thermal response caused by pulse laser heating*, Numerical Heat Transfer, Part A, Vol. 44, pp.705-722, 2003
- [8] Chin B.L., Yao G., Ding P., Fu J. and Chen L., *Barrier and Seed Technologies for Sub-0.10 μ m Copper Chips*, Semiconductor International, May 2001
- [9] Chinmulgund M., Inturi R.B., Barnard J.A., *Effect of Ar gas pressure on growth, structure, and mechanical properties of sputtered Ti, Al, TiAl, and Ti₃Al films*, Thin solid films, 270, pp. 260-263, 1995
- [10] Chu W.K., Mayer J.W. and Nicolet M.A., *Backscattering Spectrometry*, Academic Press, 1978
- [11] CRC Handbook of Chemistry and Physice, pp. 4-133, 84th Edition, 2003-2004, online version (www.hbcpNetbase.com)
- [12] CRC Handbook of Chemistry and Physice, pp. 12-219, 12-220, 84th Edition, 2003-2004, online version (www.hbcpNetbase.com)
- [13] De Cogan D. and De Cogan A., *Applied Numerical Modelling for Engineers*, Oxford Science Publications, New York, 1997

-
- [14] Devos A., Perrin B., Bonello B. and Jeannet J.-C., *Ultra-fast photoacoustics in colloids*, Proceedings of Photoacoustic and Photothermal Phenomena: 10th International Conference, edited by Scudieri F. and Bertolotti M., pp. 445-447, American Institute of Physics, 1999
- [15] Devos A. and Le Louarn A., *Strong effect of interband transitions in the picosecond ultrasonics response of metallic thin films*, Physical Review B, Vol. 68, Art.No.045405, 2003
- [16] Etchegion E., Kirchner J. and Cardona M., *Elasto-optical constants of Si*, Physical Review B Vol. 47, No. 16, pp. 10292-10303, April 1993
- [17] Gasser P., Klotz U.E., Khalid F.A. and Beffort O., *Site-specific specimen preparation by focused ion beam milling for transmission electron microscopy of metal matrix composites*, Microscopy and Microanalysis, Vol. 10, pp. 311-316, 2004
- [18] Grahn H.T., Maris H.J. and Tauc J., *Picosecond Ultrasonics*, IEEE Journal of Quantum Electronics, Vol. 25, No. 12, pp. 2562-2569, December 1989
- [19] Gusev V.E. and Karabutov A.A., *Laser Optoacoustics*, AIP Press, American Institute of Physics, 1993
- [20] Gusev V., *Laser hypersonics in fundamental and applied research*, Acustica 82 Suppl. pp. S37-S45, Jan-Feb 1996
- [21] Hälg B., *On a nonvolatile memory cell based on micro-electro-mechanics*, Proceedings of IEEE Micro Electro Mechanical Systems, Napa Valley, California, 172 - 176, Feb 1990
- [22] Hecht E., *Optik*, Oldenbourg Verlag, 2. Auflage, 1999
- [23] Hohlfeld J., Wellershoff S.-S., Güdde J. Conrad U., Jähnke V. and Matthias E., *Electron and lattice dynamics following optical excitation of metals*, Chemical Physics, 251, pp. 237-258, 2000
- [24] Hostetler J. L., Smith A. N., Czajkowsky D. M. and Norris P. M., *Measurement of the electron-phonon coupling factor dependence on film thickness and grain size in Au, Cr and Al*, Applied Optics, Vol. 38, No. 16, pp. 3614-3620, June 1999
- [25] Hurley D.H., Wright O.B., *Detection of ultrafast phenomena by use of a modified Sagnac interferometer*, Optics Letters, Vol. 24, No. 18, pp. 1305-1307, September 1999
- [26] Hurley D.H., Wright O.B., Matsuda O., Gusev V. and Kolosov O.V., *Laser picosecond acoustics in isotropic and anisotropic materials*, Ultrasonics, Vol. 38, pp. 470-474, 2000
- [27] Jiles D.C. and Staines M.P., *Piezo Optic Properties of Aluminium*, Solid State Communications, Vol. 47, No. 1, pp. 37-41, 1983
-

-
- [28] Kaganov M.I., Lifshitz I.M., Tanatarov L.V., *Relaxation between Electrons and the Crystalline Lattice*, Sov. Phys. JETP, Vol. 4, No. 2, pp. 173-178, March 1957
- [29] Khan A., Philip J. and Hess P., *Young's modulus of silicon nitride used in scanning force microscope cantilevers*, Journal of Applied Physics, Vol. 95, No. 4, pp. 1667-1672, February 2004
- [30] Kittel Ch., *Einführung in die Festkörperphysik*, Oldenbourg Verlag, 1999
- [31] KLA-Tencor corporation, *The art of defect war (updated for 0.1um)*, San Jose, 2001
- [32] Lee Y.-C., Bretz K.C., Wise F.W. and Sachse W., *Picosecond acoustic measurements of longitudinal wave velocity of submicron polymer films*, Applied Physics Letters, Vol. 69, No. 12, pp. 1692-1694, September 1996
- [33] Leutenegger T.F., *Detection of defects in cylindrical structures using a time reverse numerical simulation method*, Diss. ETH No. 14833, Zürich, 2002
- [34] Lin H.-N., Stoner R.J., Maris H.J. and Tauc J., *Phonon attenuation and velocity measurements in transparent materials by picosecond acoustic interferometry*, Journal of Applied Physics, Vol. 69, No. 7, pp. 3816-3822, April 1991
- [35] Lin H.-N., Maris H.J., Freund L.B., Lee K.Y., Luhn H. and Kern D.P., *Study of vibrational modes of gold nanostructures by picosecond ultrasonics*, Journal of Applied Physics, Vol. 73, No. 1, pp. 37-45, January 1993
- [36] Luh Y., *Diskretisierungen und Mehrgitteralgorithmen zur Lösung hyperbolischer Differentialgleichungen, am Beispiel der Wellengleichung, der Advektionsgleichung und der verallgemeinerten Stokes-Gleichungen*, Berichte der Gesellschaft für Mathematik und Datenverarbeitung, Diss. Univ. Bonn, Oldenbourg, 1992
- [37] Maris H.J., *Picosecond Ultrasonics*, Scientific American, pp. 86-89, January 1998
- [38] *Materials Science and Engineering Handbook*, CRC Press, 2004, online version (www.engnetbase.com)
- [39] Matsuda O., Fukui T., Akabori M. and Wright O.B., *Ultrafast carrier dynamics in a GaAs slab probed by acoustic phonon generation*, Proceedings of 26th International Conference on the Physics of Semiconductors, Pt. II, p.92-95, Edinburgh UK, 2002
-

-
- [40] Matsuda O. and Wright O.B., *Reflection and transmission of light in multilayers perturbed by picosecond strain pulse propagation*, Journal of the Optical Society of America B, Vol. 19, No. 12, pp. 3028-3041, December 2002
- [41] Matsuda Y., Richardson C.J.K. and Spicer J.B., *Narrowband Generation of Ultrafast Acoustic and Thermal Transients in Thin Films for Enhanced Detectability*, IEEE Transactions on Ultrasonics, Ferroelectrics, and Frequency Control, Vol. 49, No. 7, pp. 915-921, July 2002
- [42] Miklos A. and Lörincz A., *Transient thermorefectance of thin metal films in the picosecond regime*, Journal of Applied Physics, Vol. 63, No. 7, pp. 2391-2395, April 1988
- [43] Miklos A. and Lörincz A., *Determination of Thermal Transport Properties of Thin Metal Films from Pulsed Thermorefectance Measurements in the Picosecond Regime*, Applied Physics B, Vol. 48, pp. 261-267, 1989
- [44] Mizubayashi H., Yoshihara Y and Okuda S., *The Elasticity Measurements of Aluminium nm-Films*, Phys. Stat. Sol. A, 129, pp. 475-481, 1992
- [45] Mizubayashi H., Yamaguchi T. and Yoshihara Y., *An elasticity study of Al and Ag nanometre films*, Journal of Alloys and Compounds, 211/212, pp. 446-450, 1994
- [46] Natarajan A., Louder D., Dietz M., Weyandt P., Ivanecky J., Morath C., Tas G. and Clerico J., *Improving process consistency and yields of read/write heads using laser sonar metrology*, MicroMagazine, May 2003
- [47] Nikoonahad M., Lee S. and Wang H., *Picosecond photoacoustics using common-path interferometry*, Applied Physics Letters, Vol. 76, No. 4, pp. 514-516, May 2000
- [48] Oral contribution of (Prof. P. Hess) during WCU conference
- [49] Palik E.D., *Handbook of Optical Constants of Solids*, Academic Press, 1985
- [50] Perrin B., Bonello B., Jeannet J.-C. and Romatet E., *Picosecond ultrasonics study of metallic multilayers*, Physica B, 219&220, pp. 681-683, 1996
- [51] Perrin B., Bonello B., Jeannet J.-C. and Romatet E., *Interferometric detection of hypersound waves in modulated structures*, Prog. in Nat. Science, 6 Suppl., S444-S448, Dec 1996
- [52] Petersen K.E., *Dynamic Micromechanics on Silicon: Techniques and Devices*, IEEE Transactions on electron devices, Vol. 25, No.10, 1241 - 1250, Oct 1978
-

-
- [53] Profunser D.M., Vollmann J., Dual J., *Ultrasonic wave propagation in focusing tips with arbitrary geometries*, Ultrasonics, Volume 40, Issues 1-8, May 2002, Pages 747-752
- [54] Profunser D.M., Vollmann J., Bryner J., Dual J., *Measurement and simulation of the laser-based thermo-elastic excitation and propagation of acoustic pulses for thin film and MEMS inspection*, Proc. SPIE Vol. 4703, p. 21-30, Nondestructive Evaluation and Reliability of Micro- and Nanomaterial Systems, June 2002
- [55] Profunser D.M., Vollmann J., Dual J., *Determination of the material properties of microstructures by laser-based ultrasound*, Ultrasonics 42, Issues 1-9, 641-646, Elsevier Science, Amsterdam
- [56] Pyrex Corning 7740, Datasheet from Corning
- [57] Pyrex Corning 7740, Datasheet from Abrisa
- [58] Qiu T.Q. and Tien C.L., *Short-pulse laser heating on metals*, International Journal of Heat and Mass Transfer, Vol. 35, No. 3, pp. 719-726, 1992
- [59] Qiu T.Q., Tien C.L., *Size Effects on Nonequilibrium Laser Heating of Metal Films*, Transactions of the ASME, Journal of Heat Transfer, 115, pp. 842-847, November 1993
- [60] Qiu T., Tien C.-L., Shannon M.A. and Russo R.E., *Thermal and mechanical responses of gold films during nanosecond laser-pulse heating*, Experimental Heat Transfer, Vol. 7, pp. 175-188, 1994
- [61] Qiu T.Q. and Tien C.L., *Femtosecond laser heating of multi-layer metals - I. Analysis*, International Journal of Heat and Mass Transfer, Vol. 37, No. 17, pp. 2789-2797, 1994
- [62] Qiu T.Q., Juhasz T., Suarez C., Bron W.E. and Tien C.L., *Femtosecond laser heating of multi-layer metals - II. Experiments*, International Journal of Heat and Mass Transfer, Vol. 37, No. 17, pp. 2799-2808, 1994
- [63] Richardson C.J.K., Ehrlich M.J. and Wagner J.W., *Interferometric detection of ultrafast thermoelastic transients in thin films: theory with supporting experiment*, Journal of the Optical Society of America B, Vol. 16, No. 6, pp. 1007-1015, June 1999
- [64] Richardson C.J.K. and Spicer J.B., *Characterization of heat-treated tungsten thin-films using picosecond duration thermoelastic transients*, Optics and Lasers in Engineering, Vol. 40, No. 4, pp. 379-391, 2003
- [65] Rogers J.A., Maznev A.A., Banet M.J. and Nelson K.A., *Optical generation and Characterization of Acoustic Waves in Thin Films*, Annual Review of Material Science, Vol. 30, pp. 117-157, 2000
- [66] Rosei R. and Lynch D.W., *Thermomodulation Spectra of Al, Au and Cu*, Physical Review B, Vol. 5, No. 10, pp. 3883-3894, May 1972
-

-
- [67] Rudolph Tech
- [68] Schubert F., Peiffer A., Kohler B., Sanderson T., *The elastodynamic finite integration technique for waves in cylindrical geometries*, Journal of the Acoustical Society of America, Vol. 104, No. 5, 2604-2614, November 1998
- [69] Scruby C.B. and Drain L.E., *Laser Ultrasonics - Techniques and Applications*, Adam Hilger, 1990
- [70] Shackelford J.F., Alexander W., *CRC Materials Science and Engineering Handbook*, CRC press, 2001, page 823
- [71] Siry P., Belliard L. and Perrin B., *Picosecond acoustics with very high lateral resolution*, Acta Acustica united with Acustica, Vol. 89, No. 6, pp. 925-929, November-December 2003
- [72] Spectra Physics, *MilleniaTM V, User's Manual*. Spectra Physics August 1998
- [73] Spectra Physics, *TsunamiTM, User's Manual*. Spectra Physics May 1995
- [74] Strauss W.A., *Partial Differential Equations*, John Wiley and Sons Inc., New York, 1992
- [75] Tabata O., Kawahata K., Sugiyama S., Igarashi I., *Mechanical property measurements of thin films using load-deflections of composite rectangular membranes*, Sensors and Actuators, Vol. 20, No. 1-2, 135-141, 1989
- [76] Taflove A. and Hagness S.C., *Computational electrodynamics: the finite-difference time domain method*, Artech House, London-Boston, 2000
- [77] Tas G., Stoner R.J., Maris H.J., Rubloff G.W., Oehrlein G.S. and Halbout J.M., *Noninvasive picosecond ultrasonic detection of ultrathin interfacial layers: CF_x at the Al/Si interface*, Applied Physics Letters, Vol. 61, No. 15, pp. 1787-1789, October 1992
- [78] Tas G. and Maris H.J., *Picosecond ultrasonic study of phonon reflection from solid-liquid interfaces*, Physical Review B, Vol. 55, No. 3, pp. 1852-1857, January 1993
- [79] Tas G., Maris H.J., *Electron diffusion in metals studied by picosecond ultrasonics*, Physical Review B, Vol. 49, No. 21, 15046-15054, June 1994
- [80] Thomsen C., Strait J., Vardeny Z., Maris H.J., Tauc J. and Hauser J.J., *Coherent Phonon Generation and Detection by Picosecond Light Pulses*, Physical Review Letters, Vol. 53, No. 10, pp. 989-992, September 1984
-

-
- [81] Thomsen C., Grahn, H.T., Maris H.J. and Tauc J., *Surface generation and detection of phonons by picosecond light pulses*, Physical Review B, Vol. 34, No. 6, 4129-4138, 15 Sep 1986
- [82] Tzou D.Y., *Macro- to Microscale Heat Transfer - The Lagging Behaviour*, Series in Chemical and Mechanical Engineering, Taylor&Francis, 1996
- [83] Tzou D.Y., *Thermal shock phenomena under high rate response in solids*, Annual Review of Heat Transfer, Chapter 3, pp. 111-184, Tien C.L. ed., Hemisphere, Washington DC, 1992
- [84] Vertikov A., Kuball M., Nurmikko A.V. and Maris H.J., *Time-resolved pump-probe experiments with subwavelength lateral resolution*, Applied Physics Letters, Vol. 69, No. 17, pp. 2465-2467, October 1996
- [85] Vollmann J., Profunser D.M., Dual J., *Sensitivity improvement of a pump-probe set-up for thin film and microstructure metrology*, Ultrasonics, Volume 40, Issues 1-8, May 2002, Pages 757-763
- [86] Vollmann J., Profunser D.M., Dual J., *Device for filtering electrical high frequency signals*, International Patent Application, PCT/CH 02/00605, ETH Zürich, Zürich, Switzerland, November 2002
- [87] Vollmann J., Profunser D.M., Meier A.H., Döbeli M., Dual J., *Pulse laser acoustics for the characterization of inhomogeneities at interfaces of microstructures*, Ultrasonics 42, Issues 1-9, 657-663, Elsevier Science, Amsterdam
- [88] Wright O.B., Hyoguchi T. and Kawashima K., *Laser Picosecond Acoustics in Thin Films: Effect of Elastic Boundary Conditions on Pulse Generation*, Japanese Journal of Applied Physics, Vol. 30, No. 1B, pp. L131-L133, January 1990
- [89] Wright O.B., *Thickness and sound velocity measurement in thin transparent films with laser picosecond acoustics*, Journal of Applied Physics, Vol. 71, No. 4, pp.1617-1629, February 1992
- [90] Wright O.B., Hyoguchi T. and Kawashima K., *Characterization of transparent and opaque thin films using laser picosecond ultrasonics*, Nondestr. Test. Eval., Vol. 7, pp. 149-163, 1992
- [91] Wright O.B., Hyoguchi T. and Kawashima K., *Laser Picosecond Acoustics in Various Types of Thin Film*, Japanese Journal of Applied Physics, Vol. 31, Supplement 31-1, pp. 85-87, 1992
- [92] Wright O.B. and Kawashima K., *Coherent Phonon Detection from Ultrafast Surface Vibrations*, Physical Review Letters, Vol. 69, No. 11, pp. 1668-1671, September 1992
- [93] Wright O.B., *Laser picosecond acoustics in double-layer transparent films*, Optics letters, Vol. 20, No. 6, pp. 632-634, March 1995
-

-
- [94] Wright O.B. and Gusev V.E., *Ultrafast generation of acoustic waves in copper*, IEEE Transactions on Ultrasonics, Ferroelectrics, and Frequency Control, Vol. 42, No. 3, pp. 331-338, May 1995
- [95] Zhu T.C., Maris H.J., Tauc J., *Attenuation of longitudinal-acoustic phonons in amorphous SiO₂ at frequencies up to 440 GHz*, Physical Review B, Vol. 44, Number 9, pp. 4281-4289, 1 September 1991

Curriculum vitae

Dieter Michael Profunser

Born on May 19, 1974 in Feldkirch, Austria

Citizen of Austria

Education

- 1980 - 1988 Primary and Secondary school in Muntlix, Austria
- 1988 - 1993 HTL (electronics & communication engineering) in Rankweil, Austria. Graduation with a matura
- 1994 - 1999 Studies at the Mechanical Engineering Department of the Swiss Federal Institute of Technology ETH, Zürich, Switzerland. Graduation with the degree Dipl. Masch. Ing. ETH
- 1999-2004 Doctoral student at the Institute of Mechanical Systems (IMES, Center of Mechanics) of the Swiss Federal Institute of Technology ETH, Zürich, Switzerland

Professional experience/practical trainings

- 1996 - 1998 Tutoring assistant at the Institute of Mechanical Systems (IMES, Center of Mechanics), Zürich, Switzerland
- Feb. - Mar. 1997 Practical training at HILTI AG, Corporate Research, Principality of Liechtenstein
- Feb. - Mar. 1998 Practical training at ELB-Form, Research & Development, Austria
- 1999-2004 Research and teaching assistant at the Institute of Mechanical Systems (IMES, Center of Mechanics), Zürich, Switzerland
